High-power Femtosecond Laser Sources for Mid-Infrared Generation

Markus Pötzlberger

München 2021

High-power Femtosecond Laser Sources for Mid-Infrared Generation

Markus Pötzlberger

Dissertation
der Fakultät für Physik
der Ludwig-Maximilians-Universität
München

vorgelegt von
Markus Pötzlberger
aus Gmunden

München, den 23.02.2021

Erstgutachter: Prof. Dr. Ferenc Krausz
Zweitgutachter: Prof. Dr. Jörg Schreiber
Tag der mündlichen Prüfung: 06.04.2021

Contents

List of Figures

List of Tables

List of Acronyms

AMC . . . . . active multipass cell
AR . . . . . anti-reflective
CEO . . . . . carrier-envelope offset
CEP . . . . . carrier-envelope phase
Cr:ZnS . . . . . chromium-doped zinc sulfide
Cr:ZnSe . . . . . chromium-doped zinc selenide
CW . . . . . continuous wave
DFG . . . . . difference-frequency generation
EOS . . . . . electro-optic sampling
FROG . . . . . frequency-resolved optical gating
FWHM . . . . . full width at half maximum
GaSe . . . . . gallium selenide
GD . . . . . group delay
GDD . . . . . group delay dispersion
HC . . . . . Herriott cell
Ho:YAG . . . . . holmium-doped yttrium aluminum garnet
HR . . . . . highly reflective
IDFG . . . . . intra-pulse difference-frequency generation
integrated RIN$_{\mathrm{rms}}$ . . square root of the integrated relative intensity noise
KLM . . . . . Kerr-lens mode-locked
LGS . . . . . lithium gallium sulfide
mid-IR . . . . . mid-infrared
ML . . . . . mode-locked
OC . . . . . output coupler
ROC . . . . . radius of curvature

SESAM . . . . . semiconductor saturable absorber mirror
SPM . . . . . self-phase modulation
TFP . . . . . thin-film polarizer
Ti:sapphire . . . . . titanium-doped sapphire
Tm:YLF . . . . . thulium-doped yttrium lithium fluoride
Yb:CALGO . . . . . ytterbium-doped calcium aluminum gadolinium oxide
Yb:Lu_2O_3 . . . . . ytterbium-doped lutetium oxide
Yb:YAG . . . . . ytterbium-doped yttrium aluminum garnet
ZGP . . . . . zinc germanium phosphide

Zusammenfassung

Im Spektralbereich des mittleren Infrarots (MIR) treten sehr viele Wechselwirkungen zwischen Materie und elektromagnetischer Strahlung auf. Dies macht elektromagnetische Strahlung aus diesem Bereich äußerst wertvoll für spektroskopische Untersuchungen von chemischen Proben und für das Studium derer Dynamiken. Viele solcher Anwendungen würden von der Verfügbarkeit von MIR-Laserquellen mit großer spektraler Bandbreite, hoher Strahlungsdichte und zeitlicher Kohärenz profitieren. Die Technik der feldaufgelösten Infrarotspektroskopie ist eine solche Anwendung. Diese Spektroskopiemethode verspricht eine breitbandige Probenanalyse mit einem noch nie da gewesenen Dynamikbereich und einer bisher unerreichten Empfindlichkeit. Allerdings erfordert diese Methode ultrakurze Laserimpulse im schwer zugänglichen MIR-Bereich, welche zusätzlich noch eine stabile Phase zwischen der Trägerwelle und dem Impulsmaximum aufweisen müssen. Diese Diskrepanz zwischen Bedarf und Verfügbarkeit an ultrakurze Laserimpulse im MIR kann mit nichtlinearer Frequenzkonversion und der Entwicklung geeigneter Femtosekundenlaser, die diese Konversion antreiben, gelöst werden. Die Entwicklung von entsprechenden Femtosekundenlasern ist der Schwerpunkt dieser Dissertation. Die Herausforderung bei dieser Entwicklung war das Erzielen hoher Spitzen- und Durchschnittsleistungen. Diese hohen Leistungen werden benötigt, um im Konversionsprozess ausreichende Mengen an MIR-Strahlung für die spektroskopische Untersuchung zu erzeugen.

Diese Herausforderung wurde anfangs durch die erstmalige Integration einer aktiven Mehrfachabbildung (englisch: *active multipass cell*) in einen kerrlinsenmodengekoppelten (englisch: *Kerr-lens mode-locked*, KLM) Scheibenlaser angegangen. Die erfolgreiche Zusammenführung dieser beiden Konzepte ermöglichte die Verdopplung der Auskoppelrate eines Oszillators auf Basis von Ytterbium-dotiertem Yttrium-Aluminium-Granat (Yb:YAG), welcher bei einer Wellenlänge von 1,03 µm emittiert. Der so erhaltene Oszillator ist mit einer Spitzenleistung von 40 MW der bisher leistungsstärkste in Luft betriebene Oszillator. Die erfolgreiche Integration der aktiven Mehrfachabbildung und die dadurch ermöglichten Spitzenleistungen eröffnen einen neuen Pfad zu leistungsfähigeren KLM-Scheibenlasern.

Abgesehen von höheren Spitzenleistungen können auch längere Wellenlängen der Lasersysteme zu einer effizienteren Konversion in das mittlere Infrarot führen. Daher wurden mehrere Untersuchungen zur Verbesserung der neuartigen KLM-Scheibenlaser durchgeführt, welche bei einer Wellenlänge von 2,1 µm emittieren und Holmium-dotiertes Yttrium-Aluminium-Granat (Ho:YAG) als Verstärkungsmedium verwenden. Die dadurch gewonnenen Erkenntnisse führten zu einem wesentlich besseren Verständnis der optimalen Schei-

benparameter, was für die zukünftige Entwicklung von leistungsfähigeren Scheibenlasern bei einer Wellenlänge von 2,1 µm wertvoll ist.

Festkörperlaser basierend auf breitbandigem Chrom-dotiertem Zinksulfid (Cr:ZnS) wurden aufgrund ihrer Eigenschaften ebenfalls als vielversprechende Laser für die Konversion ins MIR identifiziert. Die im Allgemeinen niedrigen Durchschnittsleistungen dieses Lasertyps erforderten jedoch eine Weiterentwicklung der zugehörigen optischen Verstärker. Daher wurden für diese Verstärker verschiedene Verbesserungsansätze getestet, wie zum Beispiel die erste Implementierung eines Peltier-gekühlten Cr:ZnS-Verstärkers. Die Experimente haben gezeigt, dass eine Aneinanderreihung von vier wassergekühlten Einzelpass-Verstärkern eine Eingangsleistung von 0,73 W auf mehr als 16 W Ausgangsleistung verstärken kann. Eine solche Verstärkerleistung soll die angestrebte feldaufgelöste Spektroskopie mit MIR-Impulsen von höherer Durchschnittsleistung und größerer Bandbreite ermöglichen.

Während die Cr:ZnS-Lasertechnologie hierfür nun von Kollegen technisch weiterentwickelt wird, wird der verbesserte Yb:YAG-Oszillator bereits für neue feldaufgelöste Spektroskopieexperimente eingesetzt. Die Weiterentwicklung der Cr:ZnS-Technologie und der feldaufgelösten Infrarotspektroskopie soll letzten Endes die angestrebte hochempfindliche Analyse von relevanten chemischen und biologischen Proben ermöglichen.

Abstract

The mid-infrared (mid-IR) region of the electromagnetic spectrum is rich in interactions with matter, making mid-IR radiation tremendously useful for spectroscopic investigations of chemical specimens and the study of their dynamics. Many such applications would benefit from the availability of mid-IR laser sources with broad spectral bandwidth, high brightness and temporal coherence. Among them is the method of field-resolved infrared spectroscopy, which promises to enable broadband spectroscopy with an unprecedented dynamic range and sensitivity. However, this method requires laser pulses with ultrashort pulse durations and carrier-envelope phase stability — characteristics that are difficult to achieve and, to date, rarely demonstrated in the mid-IR region. This limited availability of appropriate sources can be tackled via nonlinear frequency conversion processes and the development of tailored femtosecond lasers that drive these processes — the latter being the focus of this thesis. The challenge is to obtain high peak and average powers from these lasers to generate meaningful amounts of mid-IR light.

This challenge was initially addressed by combining, for the very first time, an active multipass cell with a Kerr-lens mode-locked (KLM) thin-disk oscillator. The successful union of these two concepts enabled a doubling of the output coupling rate of an oscillator based on ytterbium-doped yttrium aluminum garnet (Yb:YAG) and lasing at a wavelength of 1.03 µm. The resulting oscillator, with an emitted peak power of 40 MW, is the most powerful to date in terms of peak power in ambient air. This successful integration of the active multipass cell opens a new path to more powerful KLM thin-disk oscillators.

Besides higher peak powers, a more efficient conversion into the mid-IR can also be achieved by employing longer driving wavelengths. Therefore, a femtosecond KLM thin-disk oscillator operating at a wavelength of 2.1 µm, which uses holmium-doped yttrium aluminum garnet (Ho:YAG) as the gain medium, was developed. Effort in optimizing such oscillators led to a much better understanding of the thin-disk parameter range for optimal laser operation, which is valuable for the future development of more powerful 2.1 µm thin-disk oscillators.

Bulk lasers based on chromium-doped zinc sulfide (Cr:ZnS) — a medium with ultra-broadband gain bandwidth — were also identified as a promising driving source. The limited output power of such oscillators required, however, further development of the corresponding amplification systems. Therefore, several approaches, including the first implementation of a Peltier-cooled Cr:ZnS amplifier, were tested. These experiments have shown that a chain of four water-cooled single-pass amplifiers can already boost the fem-

tosecond pulses from an initial average power of 0.73 W to an average power of more than 16 W. Such an amplifier performance shall provide future field-resolved spectroscopy experiments with ample mid-IR power and broader bandwidth.

While the Cr:ZnS bulk-laser technology is maturing, the improved Yb:YAG oscillator is already deployed for on-going field-resolved spectroscopy experiments. The further development of the Cr:ZnS technology and of field-resolved spectroscopy shall ultimately lead to the envisioned highly sensitive spectroscopic investigation of important chemical and biological specimens.

Chapter 1

Introduction

Ultrashort laser pulses are a versatile tool with diverse applications. Being the shortest events human has ever created, they open the way to the investigation of fast processes previously inaccessible, such as femtochemistry [1] and attosecond metrology [2]. They also have other unique properties that enabled new applications in a wide range of areas. For example, they facilitate various exotic material modifications [3] and are at the heart of the frequency comb technology [4]. The latter enables accurate spectroscopy [5, 6] by referencing to an atomic clock, as well as rapid, broadband dual-comb spectroscopy [7, 8]. Ultrashort laser pulses are about to make another contribution to the discipline of spectroscopy with the technique of field-resolved infrared spectroscopy, which holds promise to advance the analysis of biological samples. This technique and its potential will be introduced in this chapter, and they represent the motivation and context for the laser development undertaken in this thesis.

Having knowledge of the composition of biological samples is valuable for at least two reasons. First, the composition of a sample such as blood reflects its donor's physiological state because it contains a multitude of different constituents, metabolites and signaling molecules. Therefore, knowledge about the composition should allow conclusions to be drawn about the donor's health state [9]. Second, knowledge about the composition for many donors with different conditions would allow to recognize patterns and to gain new insights in both medicine and biology [10, 11]. These disciplines would thus benefit from a fast and reliable method to analyze biological samples [12, 13].

Vibrational spectroscopy is a capable method for identifying complex organic compounds [14]. For biologically relevant molecules, the variability of the chemical structure is much larger than the range of the individual chemical element involved. As vibrational spectroscopy addresses the vibration of chemical bonds and the structures they form, it is a promising method to differentiate such molecules. Infrared absorption spectroscopy is one form of vibrational spectroscopy. It determines the absorption caused by sub-structures (functional groups) in the spectral range from about 2.5 µm to 6.6 µm and the absorption caused by the entire chemical structure (fingerprint) in the spectral range from about 6.6 µm to 10 µm and beyond. This information can then be used for the identification of biologically relevant compounds. The corresponding spectral range from 2.5 µm to 20 µm

will be called the mid-infrared (mid-IR) range in this thesis.

Determining the composition of biological samples is, however, difficult for several reasons. Such a measurement is supposed to determine concentrations, which lie orders of magnitude apart for the various components [10]. The situation becomes even more challenging by the appearance of similar or identical molecular fragments in various molecules and the usually liquid state of matter of the sample. These circumstances lead to superimposed broad absorption spectra instead of collections of sharp, isolated absorption features [9]. The resulting broad sample absorption is called the spectroscopic fingerprint of the sample. While it is not known if this fingerprint allows a complete analysis of the sample composition, a highly reproducible method with high sensitivity and high spectral resolution can capture at least a significant portion of this information, which will still lead to better insights into the sample donors' physiological state.

Conventional spectroscopic methods like Fourier-transform infrared spectroscopy have difficulties in reaching the desired sensitivity, since those techniques detect their signal in the mid-IR region. The detectors in this spectral domain are, however, rather noisy and saturate at low power levels, which generally limits the sensitivity of such methods [15–17]. Another limitation to this sensitivity can be the intensity noise of the mid-IR source [15], as these intensity fluctuations can distort the measurement signal. Field-resolved spectroscopy, in contrast, employs a different detection scheme and mitigates the above limitations. In this way, much higher sensitivities are achievable. Field-resolved spectroscopy is based on the following measurement principle. If appropriate mid-IR radiation is applied to a specimen as an ultrashort probe pulse, then the specimen's response and the corresponding mid-IR emission will last beyond the excitation in the time domain. This behavior is illustrated in fig. 1.1a, where the excitation pulse is located on the very left. The pulse is followed by an extended, weak, decaying oscillation of the electric field. This subsequent, coherent emission is known as free induction decay [17]. It contains information about the energy of the specimen's resonances. These energies correspond to the absorption lines of the specimen. In addition, the free induction decay also provides phase information of the resonances.

The novelty of field-resolved spectroscopy [18–20] is that it records this weak mid-IR response with a technique called electro-optic sampling (EOS) [21–24]. EOS, as a sampling technique, scans a sample pulse in time over the electromagnetic field under investigation. This sampling pulse should be shorter than a half-cycle of the electric field under investigation in order to track the field. This requirement is the reason why the sample pulse is formed by higher optical frequencies — where the shorter electric-field oscillation period can support shorter pulses — rather than by the mid-IR range under investigation. For each delay step, the nonlinear process of sum-frequency generation is performed between the investigated mid-IR field and the sample pulse. The resulting sum-frequency gives rise to a slight modification in polarization at wavelengths where sample pulse and sum-frequency overlap, see fig. 1.1b. This modification is recorded for each delay step and results in a signal, which allows the reconstruction of the electric field, like the one in fig. 1.1a. The measurement system as a whole, consisting of the generation of mid-IR light, sample interaction and electro-optic sampling, is called an Infrasampler in this thesis.

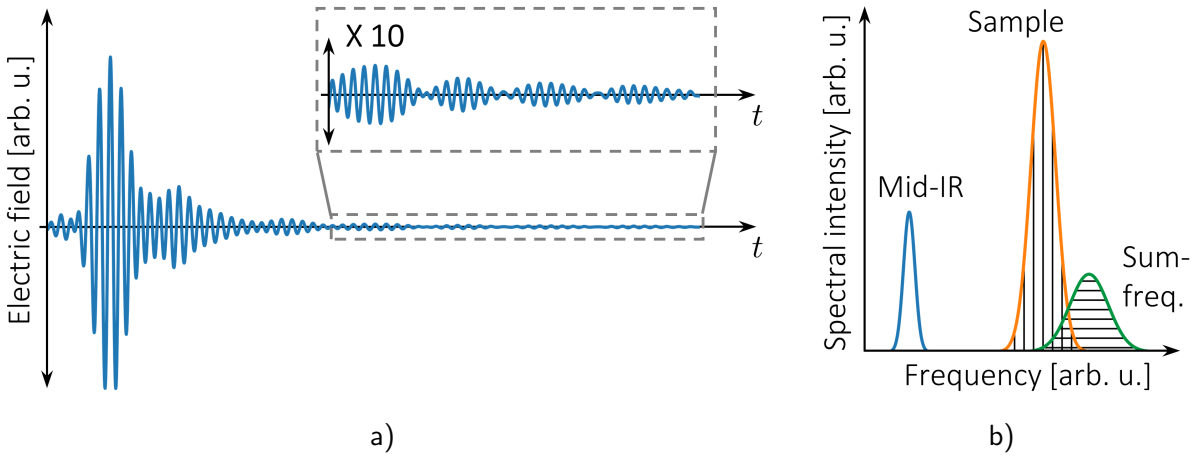

Figure 1.1: a) Mid-IR excitation pulse followed by emission due to coherent molecular response. The trailing oscillations are shown enlarged in the inset. The figure is adapted from reference [20]. b) Spectral position of the different radiations involved in EOS. The hatching direction indicates the different polarization directions for the high-frequency components. The figure is adapted from reference [23].

The measurement principle of EOS gives field-resolved spectroscopy a few advantages. The sum-frequency generation converts the specimen's mid-IR response to the spectral domain of the sample pulse, which is technologically advantageous because of the higher sensitivity [25, p. 150] and lower noise [26] of detectors there. Further, the temporal separation of response and excitation pulse allows optimization for the weak response, even in the presence of a much stronger mid-IR probe pulse [20]. The measured EOS-signal itself scales proportionately to the square root of the intensity of the mid-IR response [20]. The same applies to the signal-to-noise ratio of field-resolved spectroscopy, which allows the measurement of much thicker, strongly absorbing, aqueous samples in comparison to intensity-proportional techniques like conventional Fourier-transform infrared spectroscopy [27]. The recorded phase information may also provide additional information for the characterization of specimens. In the first demonstration of field-resolved spectroscopy, these advantages enabled a dynamic range of detectable concentrations of more than five orders of magnitude and a detection sensitivity of sub-micrograms per milliliter of blood serum [20]. This promising result outperformed the state-of-the-art Fourier-transform infrared spectrometer, which was used as a benchmark in publication [20], and the hope is that the further development of field-resolved spectroscopy will lead to an unprecedented analysis of biological samples in terms of speed and detailedness.

The realization of field-resolved spectroscopy in the configuration described above requires specific characteristics of the ultrashort, mid-IR probe pulse. The probe pulse needs to contain matching wavelengths, such that the molecules under investigation can interact with the resonant parts of the spectrum and reveal their identity. Accordingly, more information is gained about the constituents if the probe pulse covers a broader range of

relevant wavelengths. A mid-IR source with broadband, ultrashort pulses is thus highly desired for this spectroscopic application. Furthermore, the electric field under investigation needs to be reproducible from shot-to-shot for the sampling with EOS. This requirement is equivalent to a stable carrier-envelope phase of the mid-IR pulse, as introduced later in the context of eq. (2.41). Therefore, the broadband, ultrashort pulses need to be carrier-envelope-phase-stable. Furthermore, the sampling benefits from a high repetition rate because it leads to more averaging or can reduce the acquisition time. Therefore, those mid-IR pulses should be generated at megahertz repetition rates.

Intra-pulse difference-frequency generation (IDFG) delivers mid-IR radiation with all these desired properties. IDFG is a nonlinear frequency conversion process, as explained later in subsection 2.3.2. A stable carrier-envelope phase is guaranteed for IDFG in contrast to most other mid-IR sources due to the nonlinear process and its execution within one laser pulse, as will be explained at the end of subsection 2.3.2. Also, the generation of broadband ultrashort pulses is possible. The only drawback for this approach is the low conversion efficiency [28], which can be overcome by the development of tailored driving lasers.

IDFG is, in fact, the best matching approach for the generation of the desired mid-IR radiation. While other established mid-IR sources possess various advantages, they also exhibit some serious shortcomings. For example, the required temporal structure of the mid-IR probe pulse rules out simple black body radiation [29, p. 612] and synchrotron radiation [30]. Quantum cascade lasers [31], while powerful and maturing quickly, are currently still too narrow in bandwidth [32]. They provide larger bandwidths only in a gradual tuning mode and are thus inappropriate [33]. The construction of solid-state lasers in the mid-IR would be appealing, but the choice of gain media in the mid-IR is very limited [34]. Such gain media are mainly located in the range from 2 µm to 5 µm [35] and they become more challenging to operate as one moves closer to the 5 µm-limit. Iron-doped zinc selenide is one such example lasing at a wavelength of about 4 µm. It needs cryogenic cooling, lacks powerful pump sources and covers only a fraction of the desired bandwidth [36]. Therefore, currently available solid-state lasers cannot directly cover the spectral demand in the mid-IR. Optical parametric oscillators [37, 38] and optical parametric amplifiers [39, 40] are the most promising alternatives to the IDFG process because they share the same nonlinear process. In fact, they have the potential to be more efficient than IDFG. However, they require setups with interferometric stability to perform properly. These challenging alignment requirements are in strong contrast to the simplicity of an IDFG setup. An IDFG setup consists only of a focusing element, a nonlinear crystal, another focusing element for beam collimation and a dichroic element for separating the generated mid-IR. For stability and reliability reasons, IDFG is, therefore, the approach chosen for supplying field-resolved spectroscopy experiments with mid-IR radiation. The main challenge for this approach is to generate the high peak and average powers to drive the IDFG process effectively.

The aim of this thesis is to enable, using high-power femtosecond lasers, ever better mid-IR generation with broader bandwidth, higher power, higher conversion efficiency and better stability. The development of the corresponding high-power femtosecond lasers was

pursued in the framework of this thesis. The development of such lasers aids not only the advancement of field-resolved spectroscopy but also pushes the capabilities of state-of-the-art lasers. In the course of this development, several such high-power laser systems have been realized and improved. These contributions and their significance are discussed in this thesis. Introductions to these laser systems are given later in the respective sections.

The various approaches and laser systems developed are presented in the following chapters: In the first study, described in chapter 3, the peak power available from Kerr-lens mode-locked thin-disk oscillators at a wavelength of 1 µm was enhanced via the first demonstration of an integrated active multipass cell. The potent KLM thin-disk concept was then applied to a gain medium in the 2.1 µm range in chapter 4, because longer driving wavelengths greatly assist the IDFG process and the more effective generation of mid-IR light. An even more promising approach, based on chromium-doped zinc sulfide bulk lasers, was also investigated. These laser are capable of generating ultrashort pulses centered at 2.3 µm, albeit at lower powers when compared to thin-disk lasers. Chapter 5 describes the amplifier development required for this third approach. These three chapters on experiments are accompanied by chapter 2, which provides a brief introduction to the concepts relevant to this thesis, and the final chapter 6, which summarizes the main results and concludes this thesis.

Chapter 2

Theory and General Concepts

This thesis deals with experiments on Kerr-lens mode-locked thin-disk oscillators and single- or double-pass amplifiers. In this chapter, relevant terms and concepts are briefly introduced, which are necessary for the discussion and understanding of these experiments and their results. These concepts are part of the fields of laser physics and nonlinear optics.

Section 2.1 starts with fundamental basics and introduces the interaction of light and matter that takes place in the laser gain medium. The section then explains how these interactions can amplify light and introduces some other concepts with the associated mathematical models.

Section 2.2 builds on the previously introduced amplification in the gain medium and outlines further requirements for the generation of laser light. Starting from a laser operation with a temporally uniform mean-output, the spatial properties of the emitted laser beam are described in this section, before the formation of ultrashort laser pulses is outlined and essential concepts for ultrashort pulses are introduced.

Section 2.3 addresses concepts of nonlinear optics that are important for the formation of the pulses and the conversion into mid-IR radiation.

Section 2.4 introduces the special laser geometry of the thin-disk, which was used for the laser oscillators.

Throughout the sections, references are provided to excellent and more detailed resources on the topics presented.

2.1 The Gain Medium and the Amplification Process

The Amplification Process

It is the amplification of light, which enables lasers to generate their extraordinary light of high spatial and temporal coherence [41, p. 17]. This amplification will occur in the gain medium of the laser system. There, light and matter can exchange energy if a radiative transition is possible and the radiation energy matches the transition energy. The corresponding transitions in solid-state gain media are usually transitions between different electronic states $|n\rangle$.

In detail, there are three processes by which energy can be exchanged between light and the atoms/ions within the gain medium [42, p. 501]. These processes are called absorption, stimulated emission and spontaneous emission and will be described in the following by their rates at which they occur. For an easier understanding, it is advisable to think in units of photons and to express the intensity I of the interacting radiation by its mean photon-flux density Φ:

$$\Phi = \frac{I}{h\nu} \ . \tag{2.1}$$

In this equation, it is assumed that the radiation is monochromatic with frequency ν and the symbol h denotes the Planck constant.

A general description of the considered situation is given in fig. 2.1a. This figure shows the orientation of the Cartesian coordinate system used in this thesis, as well as the electromagnetic radiation with mean photon flux density Φ impinging on the gain medium. A more detailed illustration of the processes under discussion is shown in fig. 2.1b. This figure illustrates the three transition processes between a low-energy state $|1\rangle$ and a high-energy state $|2\rangle$, as discussed in the following.

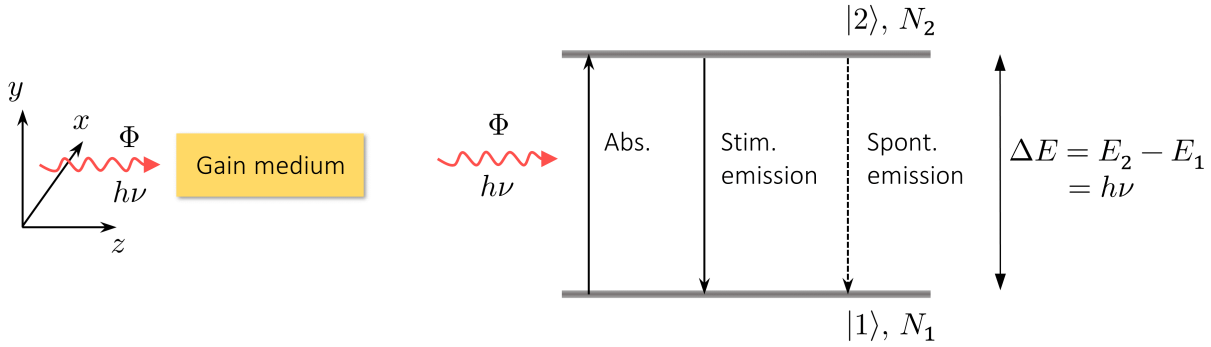

Figure 2.1: a) General description of the considered situation in which the light interacts with the gain medium. b) Schematic representation of the three interaction processes in the gain medium. The variables are defined in the main text.

The first interaction process is called absorption and transfers energy from the electromagnetic field to the gain medium. Absorption diminishes the photon-flux density Φ as the photon-flux propagates in z-direction through a location with population density N_1 and reduces simultaneously N_1 over time at this location:

$$\frac{\partial \Phi}{\partial z} = -\sigma_{12} N_1 \Phi = \frac{\partial N_1}{\partial t} \ . \tag{2.2}$$

The population density N_1 is the density of atoms/ions which are in the low-energy state $|1\rangle$. The variable σ_{12} is the absorption cross-section for the transition from $|1\rangle$ to the state

$|2\rangle$ of higher energy. The implicit dependencies on space and time of such equations are not written down for the sake of simplicity. More detailed versions of these equations can be found in reference [43].

If there is population in the excited state $|2\rangle$, then the transfer of energy can also occur from the medium to the electromagnetic field. This release of energy can be provoked by an external electromagnetic field, whose frequency ν matches the energy difference of the states $E_2 - E_1 = h\nu$. The corresponding process is called stimulated emission and it increases the photon flux density, while it reduces the population density N_2 of the excited state $|2\rangle$.

$$\frac{\partial \Phi}{\partial z} = \sigma_{21} N_2 \Phi = -\frac{\partial N_2}{\partial t} \tag{2.3}$$

Analogous to before, σ_{21} is the emission cross-section for the transition from $|2\rangle$ to $|1\rangle$. The cross sections σ_{12} and σ_{21} are identical in the current case ($\sigma_{12} = \sigma_{21} = \sigma$), because the absorption and stimulated emission take place between the same levels at the same wavelength. Moreover, systems are considered in which the degeneracy of the energy levels has no influence. More general treatments with degeneracy can be found in references [41, 44].

The excited state $|2\rangle$ can also release energy without an external electromagnetic field via the process of spontaneous emission. This process is described by the following equation:

$$\frac{\partial N_2}{\partial t} = -\frac{1}{\tau_{sp}} N_2 \ . \tag{2.4}$$

In this eq. (2.4), τ_{sp} denotes the spontaneous lifetime, which will later be replaced by a generalized upper-state lifetime τ_2 to account for possible other decay mechanisms. Spontaneous emission emits incoherent radiation and, therefore, acts only as a noise source and as a loss process. The parameters σ, τ_2 and the sum of N_1 and N_2 are material parameters.

These three processes and their equations are elementary to the explanation and modeling of laser devices. The systems of equations that can be formed with them are called rate equations.

The desired amplification of light is possible with the process of stimulated emission because the provoked emission is indistinguishable from the stimulating radiation [41, p. 17]. This means, for example, that the stimulated emission has the same directional properties, the same polarization and the same phase as the stimulating radiation. If one combines the above mentioned mechanisms, which directly interact with the external electromagnetic field (spontaneous emission is omitted), into one differential equation for the intensity $I = \Phi h\nu$, then one obtains:

$$\frac{\partial I}{\partial z} = \sigma \left(N_2 - N_1\right) I = \sigma \Delta N I \ . \tag{2.5}$$

This means that the intensity increases along z and thus amplification takes place, if the difference in population density ΔN is positive. This state of $\Delta N > 0$ is called population

inversion and is not present in gain media in thermal equilibrium [41, p. 25]. Even by optical means, no population inversion can be achieved in two-level systems, at best a transparency of the medium when absorption and stimulated emission balance each other [44, p. 7].

Equation (2.5) can be solved under the assumptions that I is the only z-dependent quantity and that the magnitude of I does not affect ΔN. The propagation dependent intensity $I(z)$ is then given as:

$$I(z) = I_0 e^{\sigma \Delta N z} = I_0 e^{g_0 z} = I_0 G_0 \ , \tag{2.6}$$

with I_0 as initial intensity, z as propagation distance within the gain medium, g_0 as small-signal gain coefficient and G_0 as small signal gain. To obtain amplification, one has to somehow reach a higher population in the upper laser level than in the lower level. The next paragraphs show how this state can be achieved.

The Gain Medium and the Idealized Four-Level System

Population inversion can be realized by optical means if one uses slightly more complex energy-level schemes than the two-level system discussed up to now. Therefore, this thesis uses four-level and quasi-three-level systems in solids with optical pumping to create inversion ($\Delta N > 0$). Accordingly, the rate equations of an idealized four-level system are discussed in the following paragraphs. Quasi-three-level systems are not explicitly discussed because they can be described as four-level systems with a considerable, thermally induced population of the lower laser level [41, p. 125]. A detailed treatment of such quasi-three-level gain media can be found, for example, in reference [45]. The reader is also referred to references for details on three-level systems [41, p. 33], details on non-optical excitation mechanisms [44, p. 232], and details on gain media other than solids [44, p. 397-474], as a complete review would go beyond the scope of this thesis.

The energy levels of a four-level system are arranged in the way depicted in fig. 2.2a. The laser ions/atoms with doping density N_{tot} reside in the ground state $|g\rangle$ in thermal equilibrium. Pump light of frequency ν_p then provides energy to the gain medium by addressing the transition from $|g\rangle$ to $|3\rangle$. An idealized four-level system has a fast non-radiative relaxation processes from $|3\rangle$ to $|2\rangle$. Accordingly, the population density N_3 remains close to zero ($N_3 \approx 0$). As a consequence, the pump light experiences only absorption as described in eq. (2.7). In this equation (2.7), the indices "p" and "a" stand for "pump" and "absorption" and N_g is the population density of the ground state.

Assuming a fast relaxation process between $|1\rangle$ and $|g\rangle$, the lower laser level $|1\rangle$ also remains unpopulated ($N_1 \approx 0$). Thus, the seed radiation with intensity I_s and frequency ν_s experiences only stimulated emission as $\Delta N = N_2 - N_1 \approx N_2$, see eq. (2.8) and eq. (2.5). This means that one obtains population inversion as soon as one pumps such an idealized system. The indices "s" and "e" in eq. (2.8) stand for "seed" and "emission".

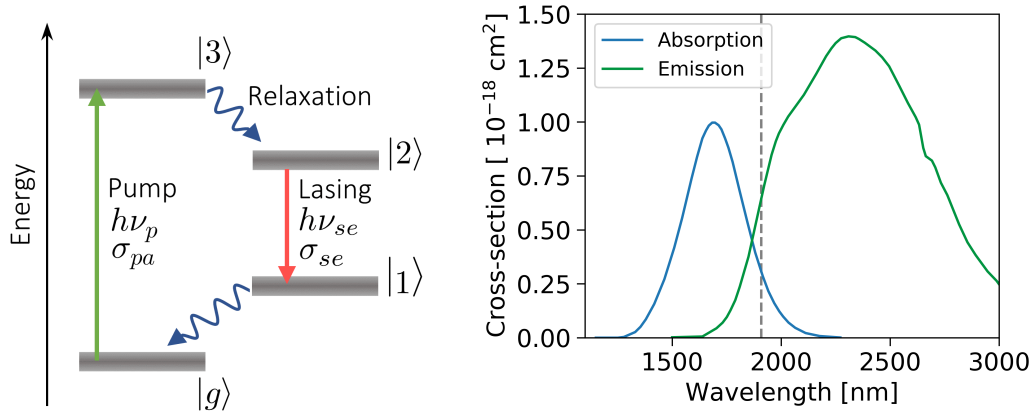

Figure 2.2: a) Energy level diagram of a four-level system. The variables are defined in the main text. b) Absorption and emission cross-sections of chromium-doped zinc sulfide. The gray, dashed line represents the later pump wavelength. The presence of absorption and emission at this pump wavelength demands a modification of the idealized rate equations, as described later in eq. (2.13) and (2.14). The displayed data was digitally extracted from reference [46].

$$\frac{\partial I_p}{\partial z} = -\sigma_{pa} N_g I_p \tag{2.7}$$

$$\frac{\partial I_s}{\partial z} = \sigma_{se} N_2 I_s \tag{2.8}$$

$$N_{tot} = N_1 + N_2 + N_3 + N_g \approx N_2 + N_g \tag{2.9}$$

$$\frac{\partial N_2}{\partial t} = \sigma_{pa} \left(N_{tot} - N_2\right) \frac{I_p}{h\nu_p} - \sigma_{se} N_2 \frac{I_s}{h\nu_s} - \frac{1}{\tau_2} N_2 \tag{2.10}$$

The entire doping density N_{tot} is distributed as population density among $|2\rangle$ and $|g\rangle$ as the other two levels remain empty, see eq. (2.9). The density N_2 is determined by eq. (2.10). The first two terms in this equation (2.10) originate from the interaction with the pump (eq. (2.7)) and seed light (eq. (2.8)) and the last term is a loss process due to spontaneous emission. The fast relaxation processes and a long upper-state lifetime τ_2 facilitate the generation of population inversion in this idealized system. Several gain media such as chromium-doped zinc selenide largely satisfy the assumptions made, making the idealized system a useful approximation for these media.

Equation (2.7) can be rewritten with eq. (2.9) to illustrate a process, which affects pump light absorption.

$$\frac{\partial I_p}{\partial z} = -\sigma_{pa} \left(N_{tot} - N_2\right) I_p = -\sigma_{pa} N_{tot} \left(1 - \frac{N_2}{N_{tot}}\right) I_p = -\alpha_0 \left(1 - \frac{N_2}{N_{tot}}\right) I_p \tag{2.11}$$

Equation (2.11) shows that the initial absorption coefficient α_0 is reduced as the inversion N_2 builds up. This happens because less population density is still available for absorption. This effect is relevant for absorption measurements such as those discussed in chapter 5.

Even in this idealized gain medium, not all supplied energy can be carried away by stimulated photons. This is the case due to the discrete nature of the excitation and the typical difference in energy between pump and seed. Therefore, the following energy fraction η_{Defect}, called quantum defect, is lost in the amplification process and is usually converted to heat:

$$\eta_{Defect} = \frac{h\nu_p - h\nu_s}{h\nu_p} = 1 - \frac{\nu_s}{\nu_p} \ . \tag{2.12}$$

This factor allows a lower estimate of the heat load and an assessment of a gain medium's suitability for high power operation. This factor will be used later.

Modified Four-Level System

The chromium-doped zinc sulfide used later in chapter 5 requires a modification of the derived rate equations, because its emission band overlaps with its absorption band and the pump process will be performed in this region of overlap, as shown in fig. 2.2b on page 11. This modification is similar to the one published for chromium-doped zinc selenide in reference [43]. The modification is that the pump radiation experiences stimulated emission with a cross section of σ_{pe} driven by the upper laser level population N_2, see eq. (2.13) and eq. (2.14).

$$\frac{\partial I_p}{\partial z} = \left[-\sigma_{pa}\left(N_{tot} - N_2\right) + \sigma_{pe}N_2\right] I_p \tag{2.13}$$

$$\frac{\partial N_2}{\partial t} = \left[\sigma_{pa}\left(N_{tot} - N_2\right) - \sigma_{pe}N_2\right] \frac{I_p}{h\nu_p} - \sigma_{se}N_2\frac{I_s}{h\nu_s} - \frac{1}{\tau_2}N_2 \tag{2.14}$$

This increases the reduction in absorption with growing population N_2 by an additional factor $(1 + \sigma_{pe}/\sigma_{pa})$ as shown in the equation below:

$$\frac{\partial I_p}{\partial z} = \left[-\sigma_{pa}\left(N_{tot} - N_2\right) + \sigma_{pe}N_2\right] I_p \tag{2.15}$$

$$= -\alpha_0 \left(1 - \left(1 + \frac{\sigma_{pe}}{\sigma_{pa}}\right) \frac{N_2}{N_{tot}}\right) I_p \ . \tag{2.16}$$

The stimulated emission with cross section σ_{pe} also reduces the steady state inversion N_{Steady} in eq. (2.17), which is obtained from eq. (2.14) for $\partial N_2/\partial t = 0$, as well as its limit N_{Inf} for an infinite pump power. The larger populations of the case without pump reemission are obtained by setting σ_{pe} to zero.

$$N_{Steady} = \frac{\sigma_{pa}N_{tot}\frac{I_p}{h\nu_p}}{\left(\sigma_{pa} + \sigma_{pe}\right)\frac{I_p}{h\nu_p} + \sigma_{se}\frac{I_s}{h\nu_s} + \frac{1}{\tau_2}} \tag{2.17}$$

$$N_{Inf} = \frac{\sigma_{pa}}{\sigma_{pa} + \sigma_{pe}}N_{tot} \tag{2.18}$$

The overlap of absorption and emission is, therefore, a shortcoming of this pump wavelength of chromium-doped zinc sulfide, because the presence of reemission reduces the amplifier performance at first. The reduction in maximal achievable inversion N_{Inf} can be compensated by an increase in doping concentration N_{tot}. However, this higher doping concentration will also lead to a higher initial absorption, which will increase the heat load at the front of the crystal. The higher doping concentration also leaves unaffected the faster decrease in absorption with inversion buildup in eq. (2.15). Thus, the presence of reemission can only be partially compensated. Whether the uncompensated effects have significant negative impacts cannot be said in general terms. The assessment requires experiments or numerical simulations.

The rate equations from above apply to oscillators and amplifiers alike, and the same holds for the next two effects. However, these effects are easier to recognize in laser amplifiers.

Gain Narrowing and Gain Saturation

The equations so far have been formulated for one pump and one seed wavelength, but in the next section 2.2 it will be seen that the amplification of broadband seed radiation is sought. If such radiation is amplified, then a narrowing of its spectral width is observed. This spectral narrowing by amplification is called gain narrowing. It originates from the wavelength dependence of the emission cross-section. As seen in fig. 2.2b, this cross section typically has a maximum at a given wavelength and decreases towards longer and shorter wavelengths. This wavelength dependence leads to a stronger amplification in the spectral center than in the outer parts and causes the reduction in spectral width when measured at half the spectral amplitude. An analytical description of this effect for a Gaussian spectrum in a gain medium with Gaussian emission cross-section can be found in reference [47, p. 402].

The second effect is called gain saturation. Equation (2.10) and eq. (2.14) showed that the population density of the upper laser level N_2 is influenced by the seed intensity I_s. This influence leads to a dependence of the gain coefficient on the applied seed intensity, which means that the amount of gain experienced in an amplifier depends on the amount of applied seed light. This effect can be derived by describing the pump light interaction by a fixed pump rate R_p into the upper laser level and by calculating the steady state of N_2:

$$\frac{\partial N_2}{\partial t} = 0 = R_p - \sigma_{se} N_2 \frac{I_s}{h\nu_s} - \frac{1}{\tau_2} N_2 \ . \tag{2.19}$$

This leads to a maximum population density N_{max} for the case without any seed light and a seed light dependent population density $N_2(I_s)$:

$$N_{max} = N_2(I_s = 0) = R_p \tau_2 \tag{2.20}$$

$$N_2(I_s) = \frac{R_p \tau_2}{1 + \tau_2 \sigma_{se} \frac{I_s}{h\nu_s}} = \frac{N_{max}}{1 + I_s / I_{sat}} \ . \tag{2.21}$$

The new variable $I_{sat} = h\nu_s/\tau_2\sigma_{se}$ is called saturation intensity. If one inserts $N_2(I_s)$ into the amplification equation of I_s (eq. (2.8)) then one obtains:

$$\frac{\partial I_s}{\partial z} = \frac{\sigma_{se}N_{max}}{1 + I_s/I_{sat}} I_s = \frac{g_{max}}{1 + I_s/I_{sat}} I_s \ , \tag{2.22}$$

where g_{max} is the maximal possible gain coefficient. This differential equation (2.22) can be solved for a gain crystal of length L. Its solution describes the emitted intensity $I_s(L)$ depending on the initial intensity $I_s(0)$ [42, p. 558].

$$\ln\left(\frac{I_s(L)}{I_{sat}}\right) + \frac{I_s(L)}{I_{sat}} = \ln\left(\frac{I_s(0)}{I_{sat}}\right) + \frac{I_s(0)}{I_{sat}} + g_{max}L \tag{2.23}$$

This solution is an transcendental equation and needs to be solved by numeric means, as it was done in fig. 2.3. This figure 2.3 displays the experienced gain as function of the seed intensity in multiples of the saturation intensity. This plot was generated for $g_{max}L = 2$. For vanishing seed intensity, the highest population inversion is present within the crystal, which leads to the highest gain. For growing seed intensity, the amplifier becomes limited by the pump rate. Due to energy conservation, the amplifier can only add a limited amount of intensity ΔI to the seed beam. This amount can be estimated as $\Delta I \approx g_{max}LI_{sat}$ by neglecting the ln()-terms in eq. (2.23) at high seed intensities. This contribution ΔI then vanishes in the quotient of the gain calculation $G = I_s(L)/I_s(0) = (I_s(0) + \Delta I)/I_s(0)$ with growing seed intensities $I_s(0)$. Therefore, the gain converges to a value of one for high seed intensities. This value is represented by the gray, dashed line in fig. 2.3.

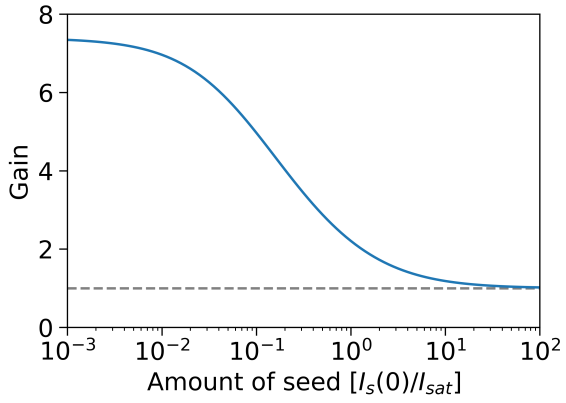

Figure 2.3: Illustration of gain saturation. The grey dashed line indicates the value one.

This last effect concludes this section on obtaining light amplification in gain media. The next section describes how this amplification can be used to generate coherent laser light and ultrashort laser pulses.

2.2 The Laser Cavity and Mode-Locking

The Laser Cavity

Besides an energy source and a gain medium for the generation of gain, it also takes a cavity formed by mirrors to realize a laser light source — a laser oscillator. The concept of a simple laser oscillator is depicted in fig. 2.4. The cavity is needed to provide feedback to the amplification process so that coherent radiation, starting from spontaneous emission, can form and be maintained. A part of the coherent radiation is then extracted from the cavity with a partially reflective mirror called the output coupler (OC).

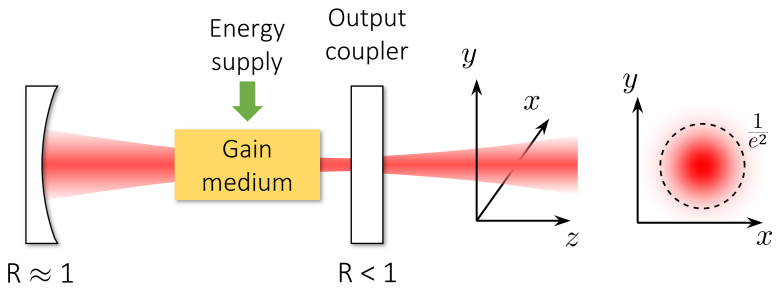

Figure 2.4: Simple laser light source consisting of an energy supply, a gain medium and a cavity formed by a highly reflective (R ≈ 1) and a partially reflective (R < 1) mirror (=the output coupler). The emitted beam propagates in z-direction. The displayed transverse intensity distribution is Gaussian. The dashed line indicates the $1/e^2$ intensity diameter, as discussed later in the context of eq. (2.27).

However, not every cavity is suitable for lasing. For efficient lasing, the cavity must be arranged so that a laser beam exists that reproduces itself after one round trip [44, p. 175]. A cavity arrangement that fulfills this criterion is called a stable cavity. This criterion must be taken into account in the design of the cavity. The corresponding analysis can be performed with so-called $ABCD$ matrices, which are a tool in ray optics to describe the action of optical elements in the paraxial approximation [42, p. 24]. Such matrices $\mathbf{M}$ are exemplified in eq. (2.24) in their general form and for a lens with focal length f.

$$\mathbf{M} = \begin{pmatrix} A & B \\ C & D \end{pmatrix} \; ; \qquad \mathbf{M}_{Lens} = \begin{pmatrix} 1 & 0 \\ -\frac{1}{f} & 1 \end{pmatrix} \tag{2.24}$$

The analysis of the cavity is then performed by calculating the $ABCD$ matrix of one round trip within the laser cavity by multiplying the corresponding matrices in their sequence ($\mathbf{M}_{Cavity} = \Pi_i \, \mathbf{M}_i$). The cavity is stable, if the entries A_{Cavity} and D_{Cavity} of the obtained matrix $\mathbf{M}_{Cavity}$ fulfill the following criterion [44, p. 175]:

$$1 - \left(\frac{A_{Cavity} + D_{Cavity}}{2} \right)^2 > 0 \; . \tag{2.25}$$

The computation on the left side of inequality (2.25) results in a value which will be called the stability parameter of the cavity. This value can be calculated depending on various degrees of freedom of the cavity and defines ranges called stability zones for these degrees of freedom, within which the cavity is stable. The visualization of these stability zones is an important design tool for laser cavities and the realization of ultrashort laser pulses. Analyses of this kind were performed with the freely available software tool "reZonator" [48]. A schematic example of such a stability plot will be seen later in fig. 2.5b. For the design of cavities, it is worth knowing that angles of incidence on concave cavity mirrors and tilted material plates lead to astigmatism [49, 50, p. 91, p. 425]. Accordingly, the properties of the cavity and the corresponding laser beam can differ in the tangential and sagittal plane of the cavity.

Once the pump, the gain medium and the laser cavity are correctly chosen and arranged, then laser operation can be obtained for those configurations where the gain can balance the losses during operation [41, p. 103]. The losses of intracavity radiation are caused by the desired output coupling rate and by parasitic effects such as reflections at interfaces, a clipping of the beam, or imperfectly reflective mirrors. In the simplest case, the laser oscillator emits its light with uniform mean-intensity over time. This mode of operation is called continuous wave (CW) operation. The cavity configuration defines, as mentioned before, which laser beam can form within the cavity. An example of such a beam evolution (=beam caustic) within the cavity is schematically shown in fig. 2.4 on page 15. A numerical simulation of such a beam evolution within a thin-disk oscillator used in this thesis will be seen later in fig. 4.5b.

The Gaussian Beam

The emitted laser beam is in the most favorable case a Gaussian beam. Such a Gaussian beam [42, p. 75] is illustrated in fig. 2.4. The intensity of this beam $I(r, z)$ depends on the radial position in the transverse plane r, the location in propagation direction z through the $1/e^2$-intensity radius $w(z)$, the beam waist radius w_0 and the peak intensity I_0. The beam waist is the smallest extent of the beam if the beam propagates freely. This waist has a $1/e^2$-intensity diameter of $2w_0$. The $1/e^2$-intensity radius $w(z)$ describes the width evolution of a freely propagating beam. The corresponding beam caustic is symmetric in z around the beam waist and determined by w_0, the location of the beam waist z_0 and the Rayleigh length z_R.

$$I(r,z) = I_0 \left(\frac{w_0}{w(z)}\right)^2 \exp\left(\frac{-2r^2}{w(z)^2}\right) \tag{2.26}$$

$$w(z) = w_0 \sqrt{1 + \left(\frac{z - z_0}{z_\mathrm{R}}\right)^2} \tag{2.27}$$

$$z_R = \frac{\pi w_0^2 n}{\lambda_0} \frac{1}{M^2} \tag{2.28}$$

The Rayleigh length itself depends on the beam waist radius w_0, the refractive index n of the medium the beam is propagating in, the vacuum wavelength λ_0 of the beam and the

beam quality factor M^2 [41, p. 226]. The Rayleigh length is important for all applications where a high intensity should be maintained over distance, because the intensity varies only by a factor of two within one Rayleigh length distance from the beam waist.

The beam quality factor M^2 quantifies the deviation of a laser beam from its theoretical ability to form a focus. Accordingly, this factor and its determination are an important topic in the construction of laser light sources. For an ideal Gaussian beam, the M^2-value takes the best possible value of one, but also other laser beams exist. For example, the transverse intensity beam profile (=the beam profile) can be of Hermite- or Laguerre-Gaussian shape [42, p. 94] with a M^2-value larger than 1. The emission of beams in such higher-order transverse modes will be called multimode operation, whereas the emission of a Gaussian beam with $M^2 \approx 1$ will be called single-mode operation. The M^2-value influences how harsh one must focus the beam to achieve a certain beam waist radius w_0. This relationship can be seen in eq. (2.29), which specifies the divergence half-angle θ. In the far-field, this is the angle between the $1/e^2$-intensity caustic and the z-axis [42, p. 85]. Steeper angles need to be realized with growing M^2-value.

$$\theta = M^2 \frac{\lambda_0}{\pi w_0 n} \tag{2.29}$$

The M^2-value also influences over which distance the waist confinement can be maintained (eq. (2.28)). The M^2-value can be determined by measuring the beam waist size and the divergence in the far-field. More details on its measurement can be found in reference [51].

A versatile tool for the description of Gaussian beams is the complex beam parameter q [42, p. 76], which fully characterizes the beam and finds application in subsection 3.4.2. One definition to compute this parameter for one particular location z is:

$$q = (z - z_0) + i z_R \ . \tag{2.30}$$

Once q is known at a specific location z, then it can be propagated with the help of $ABCD$ matrices and the following relation [42, p. 92]:

$$q_2 = \frac{Aq_1 + B}{Cq_1 + D} \ . \tag{2.31}$$

This relation specifies q_2 after the optical arrangement described by the $ABCD$ matrix, depending on the initial q_1.

So far, the laser oscillator has been operated in CW operation. The other operating mode, which generates the versatile ultrashort pulses described in chapter 1, will be introduced now. The coming subsection will outline how the corresponding mode-locked operation can be obtained. The previously presented concepts of the laser cavity and the Gaussian beam also apply to such mode-locked oscillators and their pulsed laser beams.

Mode-Locking

The laser cavity does not only define the beam caustic within the cavity and the spatial properties of the emitted beam; it also imposes a condition on the wavelengths which can

thrive within it. These are the wavelengths, which acquire a phase of multiple 2π during one round trip, such that the phase reproduces itself. The simplest demonstration of this wavelength selectivity is an empty cavity formed by two flat mirrors — a so-called Fabry-Perot resonator. Such a cavity accepts the wavelengths λ_m with their frequency spacing $\Delta\nu$ [42, p. 368]:

$$\lambda_m = \frac{2L}{m} \tag{2.32}$$

$$\Delta\nu = \frac{c}{\lambda_{m+1}} - \frac{c}{\lambda_m} = \frac{c}{2L} \ . \tag{2.33}$$

In these equations above, L is the mirror spacing, m is a positive integer and c is the speed of light. These wavelength resonances are called longitudinal modes and have a certain linewidth, which means that they are not as sharp as they appear in the equation above. Laser cavities other than Fabry-Perot resonators exhibit similarly spaced discrete frequency spectra. A more detailed discussion of the longitudinal mode spectrum of optical cavities is provided in reference [52].

A laser oscillator in CW operation typically emits light on many of these longitudinal modes unless special countermeasures are taken [41, p. 261]. That is because many longitudinal modes usually fit within the gain bandwidth and reach a gain-loss balance.

If one manages to give these frequencies a common phase reference, then they form a pronounced, localized interference, which propagates as a pulse through the cavity [41, p. 536]. This mode of operation is called mode-locked (ML) operation and can, in principle, deliver the desired powerful and ultrashort laser pulses for the frequency conversion to the mid-IR.

In the time domain description, one needs a mechanism that gives the pulse an advantage over CW radiation to establish and maintain the desired common phase reference. Such mechanisms can be realized with optical means and form the category of passive mode-locking techniques. These techniques introduce self-amplitude modulation into the cavity, which is an intensity-dependent loss [53, p. 33] that decreases with increasing intensity. Alternatively, a few techniques introduce an intensity-dependent increase in gain, which creates similar conditions as the intensity-dependent decrease in loss [53, p. 67]. The elements that introduce an intensity-dependent decreasing loss are also referred to as saturable absorbers.

One example of a widely applied passive mode-locking technique is the semiconductor saturable absorber mirror (SESAM) [54], which is a multilayer mirror of semiconductor material with an intensity-dependent decreasing absorption.

Another important passive mode-locking technique is Kerr-lens mode-locking. This technique has tremendously advanced the generation of ultrashort pulses in solid-state lasers [55, p. 74] and it is the technique used in the Kerr-lens mode-locked (KLM) oscillators of this thesis.

Kerr-lens mode-locking is based on the phenomenon that intense light with a transverse intensity variation affects its own propagation in nonlinear materials by a focusing effect. This self-focusing phenomenon will be discussed in more detail later in subsection 2.3.1.

The phenomenon leads to an intensity dependence of the beam caustic within the cavity, because the cavity now contains an intensity-dependent focusing element to which the beam evolution must adjust. These intensity-dependent changes of the beam caustic can be used to create a fast artificial saturable absorber [55, p. 104], which enables the growth of an initial intensity spike into a powerful optical pulse and the establishment of a phase relation amongst the longitudinal modes. To promote the pulse formation, one would like to achieve a large influence of the intensity on the beam caustic to create a correspondingly large advantage for the laser pulse. Two measures are taken to achieve a strong influence.

First, one exposes the nonlinear medium — the Kerr-medium — to a tiny beam diameter to achieve a noticeable focusing action via the self-focusing effect, see later eq. (2.56). This is done by creating a focus within the cavity with two concave mirrors and by placing the Kerr-medium in this focus, as depicted in fig. 2.5a. Such a telescope arrangement is called Kerr-telescope in this thesis.

Second, the influence of the self-focusing effect on the beam caustic is greatest for cavity configurations at the limit of their stability (eq. (2.25)). This is particularly true for the stability parameter as a function of the Kerr-telescope length [53, p. 73]. A stable cavity can be obtained for up to two ranges of this telescope length, as illustrated in fig. 2.5b. For Kerr-lens mode-locked operation, one usually pushes the cavity to one of the two limits, which reside between these two ranges. In other words, one pushes the cavity to an edge of its stability zones. The efficiency and power of CW operation decrease as one approaches such an edge, but a larger advantage for the intense pulse is established in this way.

The change in caustic can be used in two ways to create an advantage for the intense pulse. The first option is to design the laser in such a way that the pulses experience more gain in the gain medium than the CW radiation [55, p. 104]. This approach is called soft-aperture Kerr-lens mode-locking. The other approach is to design the cavity such that the pulses avoid a loss that CW radiation experiences. This can be achieved by integrating a slightly cropping aperture into the laser cavity at a location where the beam size shrinks with intensity [55, p. 104]. This approach is thus called hard-aperture Kerr-lens mode-locking and is depicted in fig. 2.5a. Both effects are of relevance for the oscillators discussed in this thesis.

In mode-locked operation, the output coupler extracts a portion of the circulating pulse each time the pulse bounces off this partially reflective mirror. This happens with a frequency of about $\nu_{Rep} = c/2L$ because the pulse travels in air with a group velocity close to the speed of light c, such that a round trip through the cavity of length L takes roughly $2L/c$ time [41, 58, p. 537]. Therefore, mode-locked oscillators emit light pulses periodically. Free-space, solid-state oscillators typically have pulse repetition rates from 10 MHz to 100 MHz, because it would take a cavity of about 150 m length to realize a repetition rate of 1 MHz and only a length of 0.15 m would be available for the implementation of a GHz cavity — both of which impractical for the usual, practical laser dimensions. These typical repetition rates are large enough for scanning techniques like electro-optic sampling and allow decent acquisition times with sufficient averaging.

In the previous paragraphs, the origin of the laser pulses was outlined. Next, the generated pulses and the associated theory will be introduced in more detail.

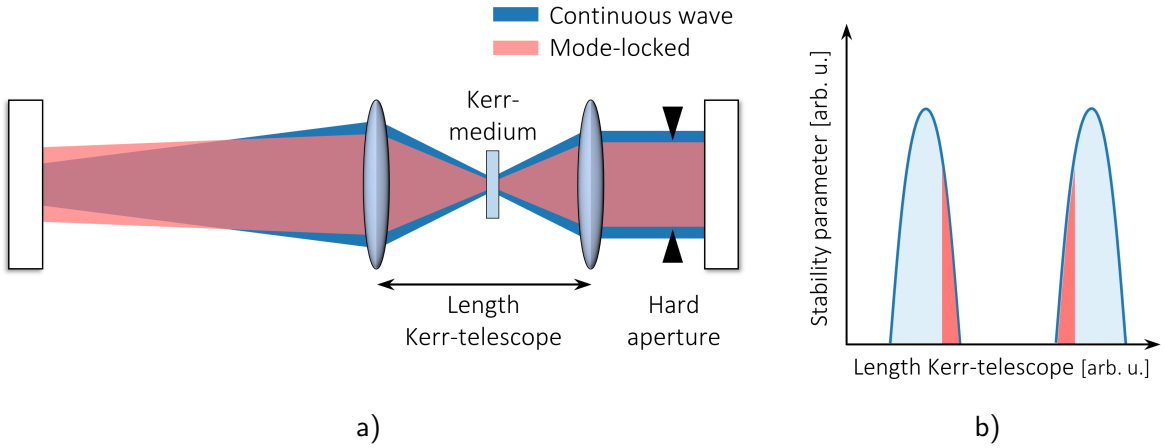

Figure 2.5: a) Schematic of a beam caustic within the laser cavity for CW and ML operation. Simulations of the different evolutions can be found in references [56, 57, p. 27]. b) A schematic graph of the stability parameter as a function of the length of the Kerr-telescope. Visible are the two stability zones that are typically found for oscillators and that result in a stable cavity. For ML operation, the cavity is usually operated at one of the two red-colored edges of the zones.

The Temporal Shape of Ultrashort Laser Pulses

The previously outlined formation of the light pulse can be described in more detail with differential equations of varying complexity — so-called master equations [53, 55, p. 78, p. 44]. Such models can describe the action of a frequency-independent loss, a frequency-dependent gain and of a linear, fast saturable absorber on the phase and the envelope $a(t)$ of the electric field for one round trip. More detailed models also include two effects called group delay dispersion and self-phase-modulation. These effects will be introduced later on page 21 and in subsection 2.3.1. For the sum of all these round-trip-based effects, one then searches for the pulse envelope that does not change from round trip to round trip. One can find a simple, analytic solution under the conditions of negative dispersion values, a moderate frequency-dependent gain and a moderate self-amplitude modulation. The envelope of the electric field $a(t)$ is then shaped like [55, p. 82]:

$$a(t) \propto \operatorname{sech}\left(\frac{t}{\tau_{sech}}\right) , \tag{2.34}$$

with the parameter τ_{sech} describing the temporal duration of the envelope. The temporal intensity profile of the pulse is accordingly a sech^2. It is common to specify the pulse duration τ_p as the full width at half maximum (FWHM) of the temporal intensity profile. In the present case the pulse duration would be $\tau_p \approx 1.763\ \tau_{sech}$ [47, 53, p. 10, p. 87]. Also, the spectral bandwidth (=the spectral width) of the pulse $\Delta\nu_p$ is usually specified in terms of the FWHM of its spectrum. The Fourier transform links the widths of the temporal and spectral domain with each other. The Fourier transform of a sech-shaped electric field is,

for example, again sech-shaped and has therefore a sech^2-shaped spectrum, for which the following relation holds [47, 53, p. 10, p. 87]:

$$\tau_p \, \Delta\nu_p \geqslant \; 0.315 \; . \tag{2.35}$$

This inequality means that the pulse cannot be shorter than a certain value defined by its spectral width. This inequality is used in subsection 3.5.2 as a sanity check for the pulse duration measurement of the oscillator. In the spectral domain (angular frequency $\omega = 2\pi\nu$), the pulse is described by amplitude information $E(\omega)$ and phase information. The shortest possible pulses are obtained for a linear or constant spectral phase and are called Fourier-transform-limited pulses. Longer pulses for a given spectrum are caused by spectral phases other than linear [59, p. 19]. This connection between spectral phase and pulse duration motivates the important topic of spectral phase management and the introduction of the concept of dispersion below.

The spectral phase can, for example, be influenced by propagation through material, because materials have a frequency dependent refractive index $n(\omega)$, if regions with absorption exist [53, p. 152]. In such materials, each spectral component of the pulse acquires an additionally modified phase $\phi(\omega)$ as it propagates for a distance L [53, p. 147]. In the spectral domain this can be written as phase modification of the corresponding field representation $E(\omega)$:

$$E(\omega, L) = E(\omega, 0) e^{-i\phi(\omega)} \tag{2.36}$$

$$\phi(\omega) = \frac{\omega \; n(\omega)}{c} L \; . \tag{2.37}$$

One can analyze the implications of the acquired frequency-dependent spectral phase by decomposing it into a Taylor series around the carrier frequency ω_0.

$$\phi(\omega) = \sum_{m=0}^{\infty} \left. \frac{\partial^m \phi}{\partial \omega^m} \right|_{\omega_0} \frac{(\omega - \omega_0)^m}{m!} = \sum_{m=0}^{\infty} \varphi_m \frac{(\omega - \omega_0)^m}{m!} \tag{2.38}$$

$$= \varphi_0 + \varphi_1 (\omega - \omega_0) + \varphi_2 \frac{(\omega - \omega_0)^2}{2} + \ldots \tag{2.39}$$

The obtained φ_m-factors cause different effects. The coefficient φ_0 is directly transferred to the time domain because it is a constant in the Fourier transform. There it alters the phase of the field oscillations relative to the envelope. The term φ_1 is known as group delay (GD) and leads to a shift of the pulse in time.

The coefficient φ_2 is called group delay dispersion (GDD). Its quadratic phase in the frequency domain corresponds to a linearly varying oscillation frequency of the pulse's electric field over time (=a linear frequency-chirp). Additionally, GDD influences the pulse duration, as exemplified in eq. (2.40). This equation specifies how a Fourier-transform-limited pulse with Gaussian temporal profile of FWHM-duration τ_{in} is elongated to a FWHM-duration τ_{out} by GDD (φ_2) [47, 53, p. 151, p. 34].

$$\tau_{out} = \tau_{in} \sqrt{1 + \left(\frac{4 \ln(2) \; \varphi_2}{\tau_{in}^2} \right)^2} \tag{2.40}$$

The equation also shows that the impact of a given amount of GDD increases as the pulses become shorter. The so obtained pulses of duration τ_{out} are longer than they could be, exhibit a linear frequency-chirp in time and are said to be chirped or stretched. GDD has analogous effects on sech^2-shaped pulses. As a rule of thumb, at a wavelength of 1 µm, material usually causes positive GDD; whereas at a wavelength of 2 µm, many materials cause negative GDD.

Higher-order φ_m-terms at their usual magnitude are not really important for the pulse durations discussed in this thesis. The GDD, on the other hand, must be taken into account.

The influence of GDD on pulse duration is the reason why advanced master equations need to take this order of dispersion into account. The inclusion of negative group delay dispersion into an oscillator cavity allows to obtain a short, Fourier-transform-limited, stationary pulse by counteracting positive GDD-contributions from material dispersion and self-phase-modulation (explained later in subsection 2.3.1). The formed pulse is called a soliton and the pulse formation regime will be called soliton mode-locking in the negative dispersion regime. Conventional means to introduce negative GDD into the oscillator cavity are prisms, dispersive mirrors and sometimes material plates. Dispersive multilayer mirrors are a very convenient method to control the GDD of the cavity. That is why such mirrors are used in this thesis. These multilayer mirrors are designed in such a way that the penetration depths of the spectral components and other interference effects with the layer structure result in the desired wavelength-dependent retardation [53, 60, p. 182].

Now that the laser oscillator emits its regular train of ultrashort pulses, the concept of the frequency comb and of the carrier-envelope phase first mentioned in chapter 1 will be introduced. Both concepts are linked to the pulse train and are needed to discuss the reproducibility of the electric field of the mid-IR excitation pulse.

For the regular train of light pulses emitted by an oscillator, it can be shown that the associated spectrum has a well-defined structure with spectral components ν_m [58]:

$$\nu_m = \nu_{CEO} + m\ \nu_{Rep}\ . \tag{2.41}$$

In this equation ν_{CEO} is the carrier-envelope-offset (CEO) frequency, m is a positive integer and ν_{Rep} is the repetition rate of the laser pulses. This regular arrangement of the spectral components forms a so-called frequency comb. The offset ν_{CEO} of the frequency comb defines the phase $\Delta\phi_{CEP} = 2\pi\nu_{CEO}/\nu_{Rep}$ by which the electric-field oscillation underneath the pulse envelope differs from pulse to pulse with respect to the pulse envelope [58]. The relative phase of the field oscillation to the peak of the pulse envelope is called the carrier-envelope phase (CEP). Its pulse-to-pulse evolution by the amount of $\Delta\phi_{CEP}$ can be controlled, for example, with loss or gain modulation inside the oscillator cavity [61]. The phase evolution then happens with a well-defined rate if ν_{CEO} was stabilized to a particular value, or the phase does not evolve if the frequency ν_{CEO} was somehow set to zero. The latter will be the case in the mid-IR generation process via intra-pulse difference-frequency generation, as will be shown later in eq. (2.67). For the mid-IR pulses generated in this way, a peak of the field oscillation will coincide with the envelope's maximum. Such a

pulse train is said to be CEP-stable, because the carrier-envelope phase is constant. The pulse train even has a CEP value of zero.

Some theoretical concepts of the temporal pulse structure were introduced up to now. The next subsection briefly outlines how the pulse duration and the spectral phase can be determined experimentally.

The Temporal Characterization of Ultrashort Laser Pulses

The temporal characterization of ultrashort laser pulses is challenging because they are the shortest events humans have created. One method to achieve this nevertheless is to gauge the pulses with themselves. This can be done with the help of a nonlinear process and a controllable temporal delay. In this thesis, noncollinear second-harmonic autocorrelation [53, 59, p. 65, p. 101] was used to measure the pulse duration of pulses longer than 100 fs. In this method, a sample of the oscillator output is split into two beams. The pulses of one beam are shifted in time with respect to the other beam by a delay stage. The beams are then focused into a nonlinear crystal where they cross each other under an angle. There in the focus, a nonlinear process creates second-harmonic light depending on the temporal separation (Δt) between the pulses of the two input beams. The created second-harmonic light is detected as the autocorrelation signal. The delay(Δt)-dependent signal of a sech^2-pulse is:

$$\text{Signal}(\Delta t) \propto \frac{\Delta t \cosh\left(\frac{\Delta t}{\tau_{sech}}\right) - \tau_{sech} \sinh\left(\frac{\Delta t}{\tau_{sech}}\right)}{\sinh\left(\frac{\Delta t}{\tau_{sech}}\right)^3} . \tag{2.42}$$

This formula allows the determination of the pulse duration. For sech^2-pulses the FWHM of the correlation signal Δt_{FWHM} and the pulse duration τ_p are related by $\Delta t_{FWHM} = 1.543\ \tau_p$ [53, p. 103]. Even though this measurement method cannot determine the spectral phase of the electric field, nor can it unambiguously determine the temporal intensity profile, it is still a fast pulse characterization method if one assumes a pulse shape, like the discussed sech^2-shape.

A measurement method that can deliver spectral phase information is frequency-resolved optical gating (FROG) [59]. A second-harmonic-generation FROG uses the same experimental concept as the noncollinear second-harmonic autocorrelation, except that it spectrally resolves the second-harmonic signal. This leads to a two-dimensional dataset of second-harmonic spectrum over delay. Spectral phase and amplitude information can be gained from this dataset by searching for the best matching input pulse, a process called retrieval. Suitable software for this process is available online [62]. One shortcoming of second-harmonic-generation FROGs is that they are insensitive to an inversion of the pulse in time. They can, therefore, not distinguish between $\phi(\omega)$ and $-\phi(\omega)$. Nonetheless, they are a powerful measurement method for practical applications and were used for the measurement of pulse durations shorter than 100 fs.

As could be seen on the previous pages, nonlinear processes are an influential, possibility-opening class of processes. The next section outlines the origin of such nonlinear pro-

cesses and discusses the processes of self-phase modulation, self-focusing and intra-pulse difference-frequency generation in appropriate detail.

2.3 Nonlinear Light-Matter Interaction

Lasers and especially ultrashort laser pulses can create high intensities and electric-field strengths. At such high field strengths, a dielectric material can begin to exhibit a noticeable nonlinear response. Sometimes this nonlinear response is desired; sometimes one wants to avoid it. For both cases, a theoretical description is helpful. A suitable description of the nonlinear response is given in many cases by a series expansion of the time-dependent dielectric polarization density (or simply the polarization response) $\mathcal{P}(t)$ [63, p. 2] of the following form:

$$\mathcal{P}(t) = \epsilon_0 \left[\chi^{(1)} E(t) + \chi^{(2)} E^2(t) + \chi^{(3)} E^3(t) + \dots \right] . \tag{2.43}$$

In this equation $E(t)$ is the applied electric field, ϵ_0 is the vacuum permittivity and $\chi^{(m)}$ is m-th-order susceptibility. The $\chi^{(1)}$-term in eq. (2.43) describes conventional linear optics. The other terms of higher order represent nonlinear contributions. Equation (2.43) is presented in its scalar form. In a more general form $P(t)$ and $E(t)$ are vectors and $\chi^{(m)}$ are tensors.

The nonlinear material response, as described in eq. (2.43), gives rise to a large number of optical effects. This happens because the higher-order susceptibilities have the ability to let electric fields interact in a nonlinear manner and the polarization, thus generated, acts as a source of new electromagnetic fields.

Some of the implications of a third-order susceptibility $\chi^{(3)}$ on ultrashort laser pulses will be discussed in subsection 2.3.1. In subsection 2.3.2 difference-frequency generation as an application of a second-order susceptibility $\chi^{(2)}$ will be introduced. Difference-frequency generation in the form of intra-pulse difference-frequency generation is the conversion process that enables the generation of the sought-after CEP-stable mid-IR radiation. A conceptual understanding of this process is required for the design of appropriate driving lasers.

2.3.1 Self-Phase Modulation and Self-Focusing

An intense beam of light experiences an additional interaction when it propagates through a medium with a third-order susceptibility $\chi^{(3)}$. For the isolated discussion of the resulting effects, it is assumed that all other nonlinear contributions are zero. Under this assumption, the polarization response is written as:

$$\mathcal{P}(t) = \epsilon_0 \left[\chi^{(1)} E(t) + \chi^{(3)} E^3(t) \right] . \tag{2.44}$$

The additional interaction caused by this nonlinear response can be accounted for as an intensity-dependent contribution to the refractive index, if an instantaneous material response is assumed [63, p. 210,p. 375]. The total, intensity-dependent refractive index $n(I)$

then becomes:

$$n(I) = n_0 + n_2\, I(x, y, t)\ . \tag{2.45}$$

In this equation n_0 is the usual, weak-field, linear refractive index, n_2 is called the nonlinear refractive index and $I(x, y, t)$ is the spatially resolved, time-dependent intensity of the beam.

Different spatial and temporal parts of the pulse are exposed to different refractive indices during propagation due to this intensity dependence. In this way, the pulse acts on its own propagation by acquiring an additional phase contribution.

Two manifestations of this self-influence will be introduced in the following in a decoupled manner. First, the effect in the temporal domain named self-phase modulation (SPM) is described. SPM is important for femtosecond oscillators and their pulses because it modifies the laser pulses' spectral content and phase. Afterwards, the effect in the spatial domain, called self-focusing, is discussed, which influences the beam propagation in material and enables Kerr-lens mode-locking. In reality, however, both effects occur simultaneously.

Self-Phase Modulation

Since the intensity of an ultrashort pulse varies in time, the leading and trailing edges of an ultrashort pulse experience a lower refractive index than the center. The corresponding phase of the different parts of the pulse can be obtained by replacing the refractive index n with $n(I)$ in the exponent of a traveling wave:

$$e^{i\left(\frac{2\pi}{\lambda_0} n z - \omega_0 t\right)} = e^{i(k_0 n_0 z - \omega_0 t)} e^{i k_0 n_2 I z} \tag{2.46}$$

$$= e^{i(k_0 n_0 z - \omega_0 t)} e^{i\phi_{NL}}\ . \tag{2.47}$$

In this equation k_0 is the angular wavenumber of the wave ($k_0 = 2\pi/\lambda_0 = \omega_0/c$) and λ_0 denotes the vacuum wavelength. Thus, the parts of the pulse experienced after a propagation of length L the additional nonlinear phase ϕ_{NL}:

$$\phi_{NL} = k_0 n_2 L I(x, y, t)\ . \tag{2.48}$$

This calculation assumed that the intensity distribution did not change during propagation. For a given x, y-coordinate, the phase of the pulse is then modified in time by:

$$\phi_{NL} = k_0 n_2 L I_{xy}(t)\ . \tag{2.49}$$

In the framework of the instantaneous frequency, this phase modification corresponds to a change in frequency [44, p. 362]:

$$\omega(t) = \omega_0 + \delta\omega(t) \tag{2.50}$$

$$= \omega_0 - \frac{\partial \phi_{NL}}{\partial t} = \omega_0 - k_0 n_2 L \frac{\partial I_{xy}(t)}{\partial t}\ . \tag{2.51}$$

This frequency variation $\delta\omega(t)$ can exceed the spectral width of the initial Fourier-transform-limited pulse. New frequencies are therefore added to the pulse. The pulse also exhibits a positive chirp with "red" spectral components in the leading part of the pulse and "blue" components in the tailing part of the pulse. The broadened bandwidth results in a shorter pulse after the removal of the chirp. In this way self-phase modulation can be used for spectral broadening and temporal compression.

The achieved pulse compression can be estimated, if one assumes a Fourier-transform-limited initial pulse, the absence of dispersion in the material and a specific time-bandwidth product for the final pulse. The spectral broadening factor $\Delta\nu_{out}/\Delta\nu_{in}$ (≈temporal compression factor) then scales proportionally to the phase shift acquired in the center of the beam [64, 65]:

$$\frac{\Delta\nu_{out}}{\Delta\nu_{in}} \propto \phi_{NL\text{-}max} \propto n_2 L I_{Peak} \propto n_2 L \, \frac{P_{Peak}}{w^2} \; . \tag{2.52}$$

In eq. (2.52) I_{Peak} denotes the peak intensity of the beam, which is related to the peak power P_{Peak} of the pulses, and w denotes the $1/e^2$-intensity radius (not to be confused with the angular frequency ω).

An undesired consequence of the SPM-related phase shift is that it limits mode-locked oscillators in the negative dispersion regime in their peak power because too much phase shift destabilizes the pulse-shaping process. Accordingly, such oscillators can tolerate only a limited phase shift per round trip, as discussed in more detail later in subsection 3.4.1. This phase shift ϕ_{NLC} can be estimated as the product of the internal peak power $P_{PeakInt}$ and the SPM coefficient γ. The equation below calculates this coefficient, which characterizes the nonlinearity of a cavity in radian per watt per round trip [66].

$$\phi_{NLC} = \oint_{Cavity} k_0 n_2(z) I_{PeakInt}(z) \, \mathrm{d}z \approx \oint_{Cavity} \frac{2k_0 n_2(z) P_{PeakInt}}{\pi w(z)^2} \, \mathrm{d}z \tag{2.53}$$

$$\phi_{NLC} \approx P_{PeakInt} \; \gamma \tag{2.54}$$

$$\gamma = 4k_0 \int_{L_{Cav}} \frac{n_2(z)}{\pi w(z)^2} \, \mathrm{d}z \tag{2.55}$$

This coefficient γ should be small. Accordingly, there should be little material in the cavity and the beam diameter should be large. These considerations will become important for the peak-power scaling of thin-disk oscillators in subsection 3.4.1.

Self-Focusing

The transverse intensity profile of a pulse is often Gaussian, where the intensity is highest in the center on the optical axis and decreases in radial direction. Accordingly, the refractive index in a nonlinear medium is higher in the center of the beam and leads to a delay of the wavefronts there. In this way, the wavefronts acquire a converging curvature. Thus, the material's nonlinearity and the intensity distribution of the beam act on the Gaussian beam like a focusing element. This is the reason why this effect is called self-focusing. It

can be approximated for a circular Gaussian beam as a lens — the so-called Kerr-lens — of focal length f if the beam profile does not change significantly in the nonlinear medium [41, 47, p. 202, p. 321]:

$$f = \frac{w_0^2}{4n_2 I_{Peak} L} = \frac{\pi w_0^4}{8n_2 P_{Peak} L} \ . \tag{2.56}$$

In this model, w_0 is the beam waist radius on the facet of the medium of thickness L. The refractive power of the Kerr-lens grows, therefore, with the peak power of the impinging pulse. This intensity dependence is an essential relationship for Kerr-lens mode-locking. The refractive power is also higher for smaller waist sizes. This is also utilized in Kerr-lens mode-locked oscillators, as mentioned in the paragraph on the Kerr-telescope on page 19. Equation (2.56) is only a first approximation, which describes neither the time dependence of the self-focusing action nor higher-order aberrations. Those effects lead to a degradation in beam quality at higher peak powers [64]. Therefore, one wants to avoid too strong self-focusing.

If the peak power surpasses a critical peak power $P_{crit} \approx \lambda_0^2 / (2\pi n_0 n_2)$ [41], then self-focusing exceeds the natural divergence of the beam. If the medium is long enough, then the beam diameter can collapse till other processes like damage formation occur. This collapse is a problem if one wants to amplify laser pulses beyond the critical peak power. The solution to this limitation is to reduce the peak power before the amplification by temporal stretching with dispersive elements as described in eq. (2.40). One then performs the amplification without beam quality degradation or crystal damage. After the amplification, the energy-rich pulse is compressed to its final peak power above the critical power by restoring its initial pulse duration [67]. This concept is called chirped pulse amplification and was awarded the Nobel Prize in Physics 2018. This concept will be applied in subsection 5.4.6 to mitigate nonlinear processes such as self-focusing in the amplifier crystals.

2.3.2 Intra-Pulse Difference-Frequency Generation

The nonlinear second-order susceptibility $\chi^{(2)}$ gives rise to a number of remarkable processes. This susceptibility is, however, not present in every material. It can be shown that only noncentrosymmetric materials can exhibit $\chi^{(2)}$-values [63, p. 44]. The polarization response of a material with $\chi^{(2)}$-term is given to the second order as:

$$\mathcal{P}(t) = \epsilon_0 \left[\chi^{(1)} E(t) + \chi^{(2)} E^2(t) \right] \ . \tag{2.57}$$

An impinging electric field, which consists out of two waves with different angular frequencies ω_1 and ω_2, can be written as:

$$E(t) = E_1 e^{-i\omega_1 t} + E_2 e^{-i\omega_2 t} + E_1^* e^{i\omega_1 t} + E_2^* e^{i\omega_2 t} \ . \tag{2.58}$$

If this linear combination is inserted into eq. (2.57) then five new frequencies appear in the polarization response. Those five frequencies describe five different frequency conversion

processes caused by the $\chi^{(2)}$-term [63, p. 7]. Difference-frequency generation (DFG) is one of them with the expression:

$$\mathcal{P}_{DFG}(t) = 2\epsilon_0\chi^{(2)}E_1E_2^*e^{-i(\omega_1-\omega_2)t} + \text{ c.c. }, \tag{2.59}$$

where c.c. denotes the complex conjugate. Efficient frequency conversion does not occur automatically. It requires the high field strengths of lasers or pulsed lasers, because the $\chi^{(2)}$-values are small. Further, special considerations, which are known as phase matching, must be taken into account to promote the process of interest. It is then possible to convert incident wavelengths into other wavelengths. This frequency conversion makes it possible to access spectral ranges that are not directly accessible with lasers, like the desired mid-IR region.

The frequency conversion can also be described within the framework of the involved photons. In the DFG process, the energy of an energetic photon called pump (γ_{pump}) is split between two new photons called seed and idler [42, p. 886].

$$\gamma_{pump} \longrightarrow \gamma_{seed} + \gamma_{idler}$$

Those photons and the corresponding laser beams are typically named according to the hierarchy $\omega_p > \omega_s > \omega_i$, where the indices from the above schematic are now used in abbreviated form. The photons of the conversion process need to fulfill energy conservation and momentum conservation:

$$\hbar\omega_p = \hbar\omega_i + \hbar\omega_s \tag{2.60}$$

$$\hbar\vec{k}_p = \hbar\vec{k}_i + \hbar\vec{k}_s \ . \tag{2.61}$$

The latter condition, with $\hbar$ as reduced Planck constant and $\vec{k}$ as wave vector, is equivalent to the condition of phase matching. A slight phase mismatch is tolerated in the experimental realization, but it reduces the output of the conversion process a lot [42, p. 890]. It should be mentioned that the DFG process is much more efficient if seed photons are also provided as input [63, p. 9]. In this thesis, one takes advantage of this fact, with the implication that the considered DFG process actually reads like this:

$$\gamma_{pump} + \gamma_{seed} \longrightarrow 2\,\gamma_{seed} + \gamma_{idler} \ .$$

The Infrasampler application is interested in mid-IR idler photons. Due to the photon nature of light, the conversion process takes place in discrete steps, as described above. Thus, a given number of pump photons can at best be converted into an equal number of idler photons. This limits the possible conversion efficiency because the generated idler photons, which have a lower wavelength, carry only a fraction of the initial pump-photon energy. The highest possible conversion efficiency $\eta_{DFG\text{-}max}$, which is obtained for a completely depleted pump beam where every pump photon is converted into an idler photon, is therefore:

$$\eta_{DFG\text{-}max} = \frac{P_{idler}}{P_{pump}} \propto \frac{h\nu_i}{h\nu_p} = \frac{\lambda_p}{\lambda_i} \ . \tag{2.62}$$

Occasionally, the energy difference between pump and idler is called quantum defect [68, p. 230], similar to the concept in classical laser amplification. In the DFG-context, a lower quantum defect allows a more efficient conversion from pump to idler. This will become relevant in section 4.1, where a doubling of the pump wavelength allows in principle a doubling of the conversion efficiency.

Complete conversion is, however, an extreme case. The more realistic scenario is a negligible depletion of the pump beam, which is equivalent to a low conversion. A corresponding model of the DFG process is presented in eq. (2.63) for the obtained idler intensity I_i. This equation (2.63) is based on the assumptions of monochromatic, collinear plane waves in a medium without absorption [68, p. 42].

$$I_i = \frac{8\pi^2}{\epsilon_0 c \lambda_i^2} \frac{d_{eff}^2}{n_i n_p n_s} L^2 \frac{\sin^2\left(\frac{\Delta k L}{2}\right)}{\left(\frac{\Delta k L}{2}\right)^2} I_s I_p \tag{2.63}$$

$$\Delta k = k_p - k_s - k_i \tag{2.64}$$

In this eq. (2.63), d_{eff} is the effective nonlinear coefficient of the interaction, which is a linear combination of $\chi^{(2)}$-tensor elements determined by the DFG-setup [68, p. 39]. The variable L is the length of the nonlinear crystal, n denotes the respective refractive index and Δk is the phase mismatch, see eq. (2.64). For the typical case of $\Delta k > 0$, it is instructive to simplify the equation to:

$$I_i = \frac{8\pi^2}{\epsilon_0 c \lambda_i^2} \frac{d_{eff}^2}{n_i n_p n_s} \frac{4}{\Delta k^2} \sin^2\left(\frac{\Delta k L}{2}\right) I_s I_p \ . \tag{2.65}$$

The corresponding conversion efficiency can be calculated with the plane wave approximation and an arbitrary area A to be:

$$\eta_{DFG} = \frac{P_{idler}}{P_{pump}} = \frac{I_i A}{I_p A} = \frac{8\pi^2}{\epsilon_0 c \lambda_i^2} \frac{d_{eff}^2}{n_i n_p n_s} \frac{4}{\Delta k^2} \sin^2\left(\frac{\Delta k L}{2}\right) I_s \ . \tag{2.66}$$

The equations (2.63) and (2.66) show that a large coefficient $d_{eff}^2/n_i n_p n_s$ promotes the conversion process. Therefore, a coefficient of this form will be used in section 4.1 to quantify the suitability of various nonlinear materials for the DFG process. The equations also show that the output and the conversion efficiency of the DFG process benefit from a high input intensity. The high input intensities should be maintained over the entire crystal length L. This can be achieved by having a high peak power available as input to the DFG process. This advantage of a high peak power was one of the motivations for the peak-power-oriented laser development of chapter 3.

The phase-mismatch Δk in eq. (2.65) causes an oscillating magnitude of the idler intensity as the light propagates through the crystal. This oscillation is caused by an evolving phase difference between the polarization response and the idler radiation and the so caused changing direction of the conversion process during propagation [68, p. 44]. Thus, the idler intensity drops completely to zero for certain critical propagation distances. The value of

Δk determines how rapidly these oscillations occur and the maximal achievable intensity at the conversion maxima. This behavior is shown in fig. 2.6. Therefore, it is usually tried to keep the phase mismatch small in order to approach the gray line of perfect phase matching and quadratic intensity growth.

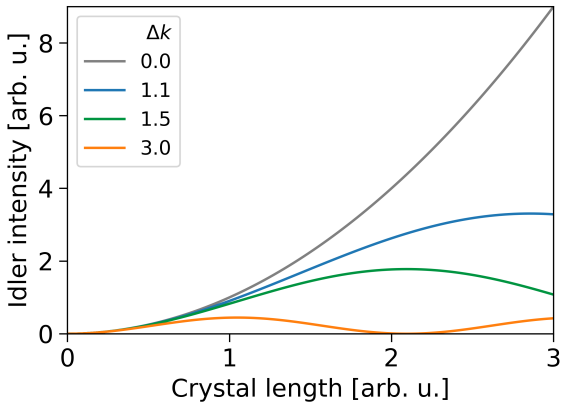

Figure 2.6: The evolution of the idler intensity along the crystal length L for different phase mismatches Δk. The figure is adapted from reference [68].

A general assessment of the phase mismatch for the later DFG application is difficult, because it depends on the crystal in use and the experimental setup, and needs to take the involved broad spectra into account. Moreover, pulse propagation effects like temporal walk-off and dispersive pulse stretching must be considered for precise predictions [68, p. 104]. Therefore, the model from eq. (2.65) can serve as a first orientation, but numerical methods are required for a precise modeling of the DFG application.

Difference-frequency generation in optical parametric amplifiers and optical parametric oscillators is typically performed with two distinct pump and seed beams. The approach of the Infrasampler project is to use intra-pulse difference-frequency generation (IDFG) [28, 69–71]. In this form of DFG, both pump and seed are applied to the nonlinear crystal as one short pulse of one beam. As introduced in chapter 1, this simplifies the experimental setup significantly and removes the need to establish and maintain a temporal and spatial overlap between pump and seed. Moreover, it delivers an intrinsic stabilization of the carrier–envelope-offset frequency because pump and seed share the same frequency comb (recall eq. (2.41)). The common frequency comb results in a carrier–envelope-offset frequency of zero for the idler beam [72], as can be seen in the equation below:

$$\nu_i = \nu_p - \nu_s = (\nu_{CEO} + m_1\nu_{Rep}) - (\nu_{CEO} + m_2\nu_{Rep}) = 0 + \Delta m\ \nu_{Rep}\ . \tag{2.67}$$

The carrier–envelope-offset frequency of zero guarantees the reproducibility of the electric-field oscillation of the mid-IR excitation pulse required for field-resolved infrared spectroscopy. This equation (2.67) also motivates the need for a broadband driving pulse because ν_p and ν_s belong to the same pulse and their difference defines the upper limit of the idler's spectral coverage. The generated mid-IR power scales quadratically with the

peak power of the driving pulse for IDFG with a fixed beam size (2.63), since pump and seed are part of the same driving pulse.

With this, the main concepts used in this thesis have been introduced. It only remains to present the special gain medium geometry used for some of the oscillators.

2.4 The Thin-Disk Geometry

The thin-disk gain-medium geometry [73], the fiber geometry and the slab gain-medium geometry are well known for their ability to deliver high average powers [74]. This ability is a prerequisite for the generation of powerful pulses at high repetition rates. What they have in common are good thermal properties due to a large surface to volume ratio. In the thin-disk geometry, this ratio is realized by attaching a roughly 0.1 mm thin disk of gain material with a diameter of about 9 mm to a heat sink via one of the circular surfaces. The low thickness of the disk results in a small increase in temperature, which arises due to the heat load in the pumped laser material.

This relationship between thickness and temperature increase can be explained with the following law, which applies under the assumptions of a one-dimensional heat flow and a concentration of the heat load onto the disk's front surface. In this case, the temperature difference ΔT for a given heat flux density q scales with the thickness of the disk Δz [75, p. 300]:

$$q = -k\frac{\Delta T}{\Delta z} \ . \tag{2.68}$$

In this equation, k is the thermal conductivity of the disk material and ΔT is, as mentioned, the temperature difference between the front side and back side of the disk. This equation is generally useful for thermal management considerations.

The one-dimensional heat flow towards the heat sink reduces additionally transverse temperature variations and, therefore, thermal lensing to a minimum. This reduced thermal lensing allows operation over a wide power range and supports transverse single-mode operation. The description as one-dimensional heat flow is justified by applying a top-hat-shaped pump beam and by the large transverse extent of the heated area in comparison to the disk thickness [73].

These features lay the foundation for the application of the thin-disk geometry in powerful thin-disk oscillators. Other advantages of this geometry that make thin-disk oscillators a suitable candidate as driving laser are discussed in detail later in section 3.1 and subsection 3.4.1.

A schematic of a thin-disk and the surrounding structure is provided in fig. 2.7. The slice of gain material is equipped with a highly reflective (HR) coating on the side of the heat sink, which allows the use of the thin-disk as an active (=amplifying) mirror within the cavity. For efficient operation, the front side is equipped with an anti-reflective (AR) coating, as depicted in fig. 2.7a. The coatings have the same functions for the seed beam and for the pump beam. This functionality allows the application of the pump light

from the front side. The absorption of one pass through the thin-disk is low due to the thinness. Therefore, the pump beam is reflected many times onto the disk with advanced arrangements of retroreflectors and a parabolic mirror, as indicated in fig. 2.7b. These multiple passes allow efficient pump light absorption and create a pumped area on the disk called the pump spot. For oscillator applications, the pump spot is typically about 3 mm in diameter.

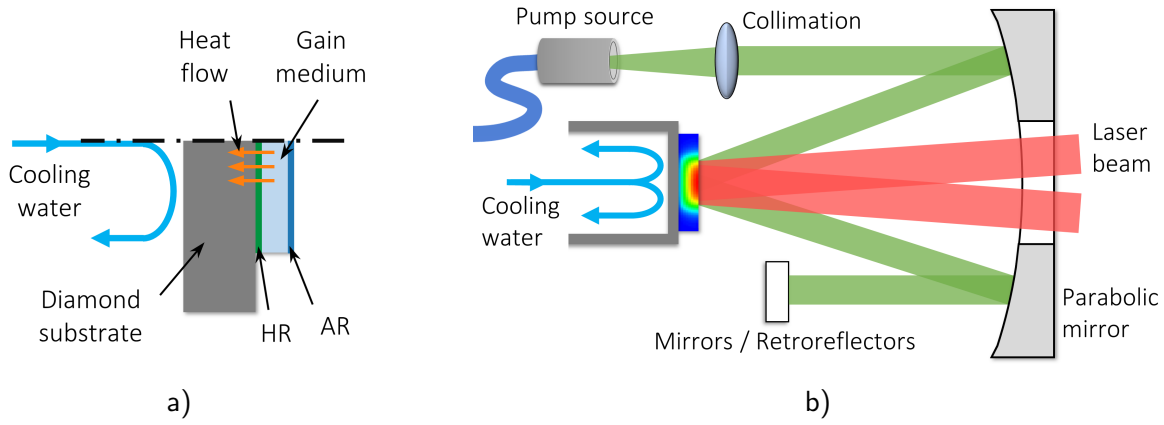

Figure 2.7: a) Close-up of a cut through the thin-disk. b) Schematic of the thin-disk and its surrounding structure. The pump light is collimated and then imaged many times onto the thin-disk by a parabolic mirror and retroreflectors. The pump and laser beams penetrate the disk and are reflected on the back of the disk. The false colors of the disk indicate the temperature profile within the disk.

Potential suppliers of thin-disks are TRUMPF Laser GmbH, Dausinger & Giesen GmbH and TRUMPF Scientific Lasers GmbH. The thin-disks of this thesis were purchased from TRUMPF Laser GmbH, who manufacture two types of thin-disks. They bond disks either to flat or curved diamond substrates as back-side-cooled heat sinks. The flat thin-disks have a remaining radius of curvature of about 20 to 15 m and the curved thin-disks have a radius of curvature (ROC) of about 2 m. The flat thin-disks are closer to the idea of an easy-to-integrate, active mirror. The curved thin-disks are useful for cavities without concave mirrors and can better match certain coating-stress-induced disk curvatures.

Chapter 3

Yb:YAG Thin-Disk Oscillator

3.1 Motivation to use Yb:YAG Thin-Disk Oscillators for Intra-Pulse Difference-Frequency Generation

The method of intra-pulse difference-frequency generation is the technique of choice to obtain the desired broadband spectral coverage in the mid-IR with CEP-stability for the Infrasampler application, as introduced in chapter 1 and in subsection 2.3.2. The conversion efficiency of this technique is, however, quite low when driven by 1 µm pulses [76]. Therefore, high average powers of the driving pulses are in general desired to obtain decent amounts of mid-IR radiation.

The great thermal management capabilities of the thin-disk geometry were introduced in section 2.4. These thermal properties allow the realization of high average powers in thin-disk systems. This is especially the case, at a wavelength of 1 µm, with thin-disks made of ytterbium-doped yttrium aluminum garnet (Yb:YAG). This material dominates the thin-disk oscillator development in terms of average power [77] and peak power [78]. Such Yb:YAG thin-disk oscillators are generally the most powerful oscillators in terms of average power [66, 77] and provide sufficient power — at over 100 W — for the IDFG process.

A prerequisite for all nonlinear processes is a high intensity. Such an intensity can be achieved by high peak powers of the driving pulses. Thin-disk oscillators can deliver high peak powers. They are, in fact, the most powerful oscillators in terms of peak power [57, p. 3], which makes them promising candidates for driving IDFG.

As outstanding oscillators, they narrow the gap between conventional oscillators and amplified systems in terms of pulse energy. Although they are not reaching the impressive performances of cutting-edge amplifier systems [79, 80], they still deliver pulse energies of several microjoules at repetition rates of multiple megahertz with modest complexity. As a result, the use of a thin-disk oscillator can allow one to skip the use of an external amplifier for some parameter ranges [81–83].

Omitting an external amplifier has many advantages. The resulting laser system can be less complex, is most likely lower in intensity noise and removes the need for temporal

stretching and compression, which is typically required for fiber amplifiers.

Thin-disk oscillators can also deliver higher repetition rates than conventional bulk amplifiers. They can deliver their energetic pulses at megahertz-scale repetition rates because they are able to emit the corresponding high average power. The use of higher repetition rates in experiments can have the advantages of shorter acquisition times and/or better signal-to-noise ratios. These advantages of thin-disk oscillators over amplified systems increase the appeal of thin-disk oscillators for IDFG and the Infrasampler application.

One shortcoming of thin-disk oscillators is the achievable pulse duration, as only a limited selection of materials is suitable for this geometry due to different properties required from the gain medium [84]. Titanium-doped sapphire (Ti:sapphire) — capable of generating few-cycle pulses — is not among them. Its development for the thin-disk geometry is ongoing but with limited success so far [85, 86]. Other ytterbium-doped gain materials are currently limited to about 20 W and 90 fs [56, 57].

Subsequent spectral broadening and temporal compression can overcome the shortcoming in achievable pulse durations. The search for a suitable and reliable broadening scheme led to the Herriott cell (HC) concept for broadening [87–89]. With this technology, it became possible to transfer the power capabilities of thin-disk oscillators into the sub-20 fs range [88]. It is this reduction in pulse duration which makes thin-disk oscillators useable for the Infrasampler application, because the pulse duration of the driving pulse defines the spectral width of the IDFG output and a short sampling pulse is also needed for electro-optic sampling [24]. As a side effect, this implementation of spectral broadening and temporal compression also boosts the peak power of the oscillator output further, which is beneficial for the IDFG process.

These are the reasons why the technologies of Yb:YAG thin-disk oscillators and spectral broadening in Herriott cells became part of the first implementations of field-resolved infrared spectroscopy in our research group. For example, the thin-disk oscillator I built during my master's project [90] became the front-end of "Infrasampler 1.2" and enabled the first demonstration of the superior sensitivity of field-resolved spectroscopy [20].

This was, however, only the first demonstration of field-resolved spectroscopy and there is still a lot of potential for further development of the thin-disk oscillator, as will be motivated in section 3.3. But before, some more general properties of Yb:YAG are introduced in the next section 3.2.

3.2 Properties of Yb:YAG as Laser Gain Medium

Many materials like ytterbium-doped calcium aluminum gadolinium oxide (Yb:CALGO) or ytterbium-doped lutetium oxide (Yb:Lu_2O_3) have been tested in the thin-disk geometry with the aim to realize short pulses with high average power [56, 84, 85]. Ytterbium-doped yttrium aluminum garnet is, however, still the only well-developed material in thin-disk geometry and is readily available commercially.

Yb:YAG has a broad absorption feature around 940 nm, as shown by the absorption cross-section in fig. 3.1a. This absorption feature can be utilized with widely available

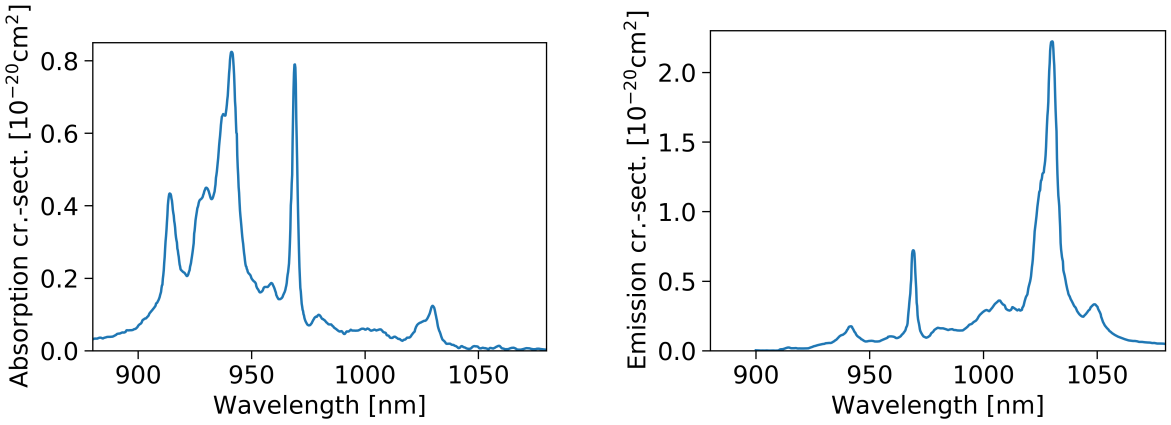

Figure 3.1: a) Absorption cross-section of Yb:YAG, with pronounced features at 940 nm and 969 nm. b) Emission cross-section of Yb:YAG, with its main emission feature at 1030 nm. The data was digitally extracted from reference [91].

high-power diode lasers. Another much narrower absorption feature at 969 nm can be used for pumping too. Its usage reduces the quantum defect but requires more expensive, wavelength-stabilized diode lasers. The energy levels of Yb:YAG form a quasi-three-level system. Therefore, a certain pump intensity is required before population inversion is achieved. This also applies to the holmium-doped YAG discussed in chapter 4.

The emission cross-section of Yb:YAG is displayed in fig. 3.1b. Its dominating feature is centered at 1030 nm and exhibits a width of about 9 nm (FWHM). This bandwidth, as a first estimation of the spectral width of the emitted pulses, would support 130 fs pulses. Longer pulse durations are, however, commonly emitted by oscillators [57]. Shorter pulse durations have been demonstrated too [92], albeit at a greatly reduced power level.

Doping concentrations of Yb:YAG thin-disks are typically in the range between 7 % [93] and 11 % [94]. Such high doping concentrations are possible because Yb:YAG exhibits, due to its simple energy-level structure, no detrimental loss processes like upconversion [45, 94]. The absence of such loss processes is an advantage, as holmium-doped YAG suffering from upconversion will show in chapter 4. The observable green or sometimes blue fluorescence of pumped Yb:YAG thin-disks results from energy transfer to rare-earth impurities (green) or from cooperative luminescence (blue) [95].

3.3 Development Goal for the Yb:YAG Thin-Disk Oscillator

Many different development goals for thin-disk oscillators exist because different applications value the various oscillator properties differently. Elementary properties of an oscillator are its repetition rate ν_{Rep}, pulse energy E_{Pulse} and pulse duration τ_p. They lead

to the quantities average power P_{Out} and peak power P_{Peak} as described in the equations below.

$$P_{Out} = \nu_{Rep}\, E_{Pulse} \tag{3.1}$$

$$P_{Peak} \approx 0.88\, \frac{E_{Pulse}}{\tau_p} \tag{3.2}$$

The calculation of the peak power assumed the presence of a $sech^2$-shaped intensity of the pulse. The actual pulse does not always have to have this pulse shape. For example, the shape can be different after a pulse compression stage. However, the calculation of the peak power will always have the form pulse energy divided by pulse duration. Other properties of the oscillator, which tend to become relevant at a later development stage, are properties like intensity noise, long-term stability, reliability and energy efficiency.

Higher average powers as development goal are mainly pursued for applications in material processing and to some extent for conversion processes with low efficiency. The shortest pulses are mainly developed for scientific applications as they define the temporal resolution and the spectral content provided by the pulses. The achievable peak power is also mainly of scientific interest, with nonlinear processes as application case. An overview in terms of achieved average power in thin-disk oscillators can be found in references [57, 77, 96]. Overviews over pulse durations and materials can be found in references [56, 57, 84, 92].

This thesis will focus on the aspect of peak power because it is the peak power that makes nonlinear optical processes accessible. For example, it is technically easier to realize nonlinear spectral broadening in HCs for pulses with higher peak power, because small spot sizes in the broadening medium are difficult to realize. Therefore, the relaxed requirement on focus spot size, which comes with an increase in peak power (eq. (2.52)), is highly beneficial. The corresponding ability to use curved mirrors with longer focal lengths, which form longer HCs, is welcomed since it increases the flexibility in spatially configuring the setup.

The exact pulse duration of the oscillator output is not of utmost importance for the Herriott cell broadening scheme. Reference [97] and [88] exemplify this. Both HC-systems reached about 20 fs pulse duration, although they started with 460 fs and 220 fs respectively. Consequently, one does not need a particular input pulse duration for the HC and one can accept the typically emitted pulse durations of 200 – 350 fs for KLM Yb:YAG thin-disk oscillators. Thus, the goal is to raise the oscillator's peak power while maintaining the typical pulse durations of KLM thin-disk oscillators. This is equivalent to more energetic pulses from the oscillator, as described in eq. (3.2).

The increase in oscillator pulse energy is also advantageous for the IDFG process. This increase should be transferred at least partially to the output of an appropriately adapted HC. This leads to a higher peak power at the output of this HC, because the adapted HC should be able to deliver the same compressed pulse duration again. As pointed out in subsection 2.3.2, the generated mid-IR power grows quadratically with this increase in peak power, which leads to better signal-to-noise ratios in the field-resolved measurements.

The emitted pulse energy and the repetition rate define the average output power of the oscillator (eq. (3.1)). This average output power faces a constrain defined by the pump spot size, the maximum permissible pump-power density and the limited conversion efficiency. This constraint requires a tradeoff between the oscillator's peak power and its repetition rate, where one tends to sacrifice the repetition rate to let the peak power grow. The reason for this is that the generated mid-IR power scales linearly with the repetition rate for a fixed driving peak power. The mid-IR power grows, however, quadratically with the applied peak power at a fixed repetition rate. Therefore, exchanging pulse repetition rate for peak power can be advantageous. Based on this, the development goal is to maximize a thin-disk oscillator for peak power at pulse durations of 200 – 350 fs and one is willing to reduce the repetition rate within the typical MHz-range for this purpose.

3.4 State of the Art of Yb:YAG Thin-Disk Oscillators

Table 3.1 provides an overview of thin-disk oscillators with a focus on peak power. The first three entries in this table are examples of oscillators under modified atmosphere. This approach holds the record in terms of peak and average power. The second half of the table lists the strongest oscillators operated in ambient air. Those oscillators are of direct relevance, as this thesis will focus on the realization of high peak powers under ambient conditions. The different approaches towards high peak power present in this table will be discussed in the next subsection 3.4.1. The last entry of the table represents a result from

Table 3.1: Overview of thin-disk oscillators with focus on the emitted peak power. Also listed are the output coupling rate as OC, the incorporated group delay dispersion per round trip as GDD, the average output power, the pulse duration and the repetition rate.

Environment	ML Type	OC [%]	GDD [-fs^2]	P_{Out} [W]	τ_p [fs]	ν_{Rep} [MHz]	P_{Peak} [MW]	Year [Ref.]
140 mbar air	KLM	15	12 000	155	140	15.6	62	2016 [98]
1 mbar air	SESAM	25	28 000	242	1070	3.0	66	2014 [78]
30 mbar N_2	SESAM	25	16 600	350	940	8.9	37	2019 [77]
ambient	SESAM	72	346 500	145	1120	3.5	32	2012 [99]
	SESAM	40	16 800	210	780	11.0	22	2018 [100]
	KLM	21	48 000	270	330	18.8	38	2014 [101]
	KLM	50	39 000	140	290	10.6	40	this work 2019 [102]

this thesis and holds currently the record in peak power under ambient conditions. This result was published in a peer-reviewed journal [102] and will be introduced in detail in subsection 3.5.2.

3.4.1 Peak-Power Scaling Approaches

The emission of high peak powers by oscillators is, in general, a challenge. One reason for this is that large nonlinear phase shifts in the spectral domain act against the formation of powerful pulses in the soliton regime of negative dispersion [66, 83, 103]. This is the case because the oscillator needs to find a steady state for all the round-trip-based effects such as wavelength-dependent gain, losses, wavelength-dependent dispersion, self-amplitude modulation and self-phase modulation (the nonlinear phase shift). A too large phase shift disturbs this pulse-shaping process and destabilizes the mode-locked operation [104, 105], leading to a limitation in intracavity peak power. Another hindrance arises due to self-focusing and the potential damages it causes, which is especially an issue in mode-locked fiber oscillators. Thin-disk oscillators can handle both challenges better than fiber and bulk oscillators since the intracavity radiation is only transmitted through very little material, namely the thin gain medium. The nonlinear interaction is further reduced by virtue of the large beam size on it (eq. (2.55)). A related advantage of Kerr-lens mode-locked thin-disk oscillators is the spatial separation of amplification and nonlinear interaction for mode-locking. Thanks to this decoupling, the interaction in the Kerr-medium can be tuned at will by using different dielectric media, without consequences for the experienced gain. Due to these advantages, thin-disk oscillators can realize higher peak powers than other oscillators.

The peak power of thin-disk oscillators can then reach up to the point at which more nonlinear phase shift cannot be handled anymore. Different strategies were developed to overcome this limitation in peak power. A general idea is to reduce the undesired nonlinear contributions, such as the air within the laser cavity. Accordingly, it was possible to improve the performance by operating the oscillator filled with helium, which is less nonlinear [106]. Taking this approach further, records in peak power were obtained with oscillators operated under reduced air pressure [57, 78, 98]. This approach's shortcomings are that it makes the oscillators harder to access, more expensive and more complex to handle, because the oscillators need to be operated within a vacuum chamber.

Another approach to avoid the generation of nonlinear phase shift is to stretch the propagating pulse in time. This can be achieved with mode-locked operation in the positive dispersion regime without narrowing the spectral bandwidth of the generated pulses. This strategy is successfully applied in fiber oscillators [107, 108] and in Ti:sapphire-based bulk oscillators [109]. However, up to now, this approach led only to a marginal relative power improvement in thin-disk oscillators at 1 µm [93, 110] and is known for a difficult initiation of mode-locked operation [93]. Other pulse formation processes for peak-power scaling, such as those based on similaritons or Mamyshev oscillators, are proposed too [111, 112], but remain to be demonstrated in thin-disk oscillators.

A different route is to counteract the induced nonlinearity with cascaded quadratic nonlinearities [100, 113]. Here the SPM generated in air is compensated partially with an intracavity phase-mismatched second-harmonic process [100]. This technology's full potential is not known yet, but the necessary tuning of the second-harmonic process makes it a delicate approach.

Alternatively, one does not need to tackle the peak-power limitation within the cavity. Instead, one can attempt to make more of the intracavity peak power available for external use. This can, in principle, be done by increasing the output coupling rate. However, this needs to be compensated by additional gain within the cavity, which can be obtained most easily by passing the pulse multiple times through the thin-disk per round trip. This multipass idea and the increased output coupling rate were demonstrated for SESAM mode-locked oscillators [99, 114, 115], but not for Kerr-lens mode-locked oscillators. In publication [99] these ideas allowed mode-locked operation with output coupling rates of up to 72 %, producing a pulse energy of 41 µJ and an external peak power of 32 MW. A key ingredient is the way how the additional thin-disk passes are implemented. The corresponding concept is called active multipass cell and will be introduced in the next subsection 3.4.2.

3.4.2 The Imaged Multipass Concept

The idea of the active multipass cell (AMC) [114] is to image the laser beam, which comes from the thin-disk, again onto the thin-disk multiple times. The adjective "active" in the name emphasizes the presence of the gain medium in the corresponding arrangement.

In the best case, the imaging is done without changing the complex beam parameter q, because then the beam caustic in the rest of the cavity remains unaffected by the inclusion of the imaging arrangement. A potential tool for the imaging is a $4f$-telescope. However, this telescope needs to take the refractive power of the thin-disk into account to achieve a conservation of the laser beam. Thus, the actual scheme of the imaging arrangement looks like the one depicted in fig. 3.2. The condition for the compensation of the additional

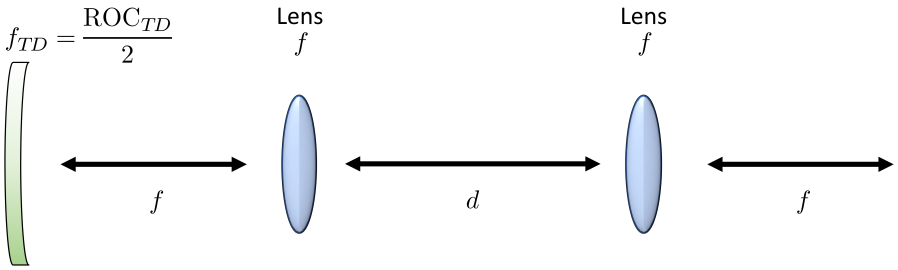

Figure 3.2: Scheme of the imaging arrangement, which is the basis unit of the multipass cell. The thin-disk is illustrated on the left. Its residual curvature acts as a concave mirror. The corresponding focal power needs to be compensated by distance d of the $4f$-telescope.

refractive power is specified to be [116]:

$$d = 2f - \frac{f^2}{f_{TD}} \,. \tag{3.3}$$

In this equation, d is the distance between the focusing elements with focal length f and f_{TD} is the focal length of the thin-disk, as depicted in fig. 3.2. This condition can be derived, if one executes the $ABCD$ matrix calculation for the imaging arrangement and equates it to the negative identity matrix:

$$\begin{pmatrix} 1 & f \\ 0 & 1 \end{pmatrix} \begin{pmatrix} 1 & 0 \\ -\frac{1}{f} & 1 \end{pmatrix} \begin{pmatrix} 1 & d \\ 0 & 1 \end{pmatrix} \begin{pmatrix} 1 & 0 \\ -\frac{1}{f} & 1 \end{pmatrix} \begin{pmatrix} 1 & f \\ 0 & 1 \end{pmatrix} \begin{pmatrix} 1 & 0 \\ -\frac{1}{f_{TD}} & 1 \end{pmatrix}$$
$$= \begin{pmatrix} -1 & 0 \\ \frac{d}{f^2} - \frac{2}{f} + \frac{1}{f_{TD}} & -1 \end{pmatrix} \stackrel{!}{=} \begin{pmatrix} -1 & 0 \\ 0 & -1 \end{pmatrix} . \tag{3.4}$$

Equation (3.4) then provides the condition for d to compensate the additional refractive power of the thin-disk:

$$\frac{d}{f^2} - \frac{2}{f} + \frac{1}{f_{TD}} = 0 \tag{3.5}$$

$$d = 2f - \frac{f^2}{f_{TD}} . \tag{3.6}$$

Transmission through such an imaging arrangement does not alter the laser beam, because the arrangement returns the same complex beam parameter q_2 as it started with (q_1):

$$q_2 = \frac{Aq_1 + B}{Cq_1 + D} \tag{3.7}$$

$$q_2 = \frac{-1q_1 + 0}{0q_1 - 1} = q_1 . \tag{3.8}$$

A shortcoming of this imaging arrangement is that the above is only true for a specific refractive power of the thin-disk. Deviations from this particular refractive power will still affect the laser beam. Consequently, the stability zone of the cavity with respect to the thin-disk's focal power shrinks with a growing number of images [116], simply because the intracavity laser beam is exposed to changes in focal power more often if multiple such arrangements are incorporated into the cavity. Similarly, aspherical aberrations of the thin-disk are also accumulated, which cause diffraction losses and promote higher-order transverse modes [117, p. 33].

Nonetheless, it is a better implementation of multiple reflections on the thin-disk than one can achieve with simple flat mirrors, because it has the ability to reproduce the laser beam on the disk and it can compensate at least a specific refractive power of the disk.

Another favorable feature of this imaging arrangement is that it allows multiple implementations of itself with only one set of optics. This then forms a so-called active multipass cell [114]. A schematic of such an AMC is depicted in fig. 3.3.

By looking at this fig. 3.3, the following key insights regarding the multiple passes through the AMC and the arrangement of the AMC components are gained. First, the laser beams, which leave the disk under different angles, are made parallel to each other

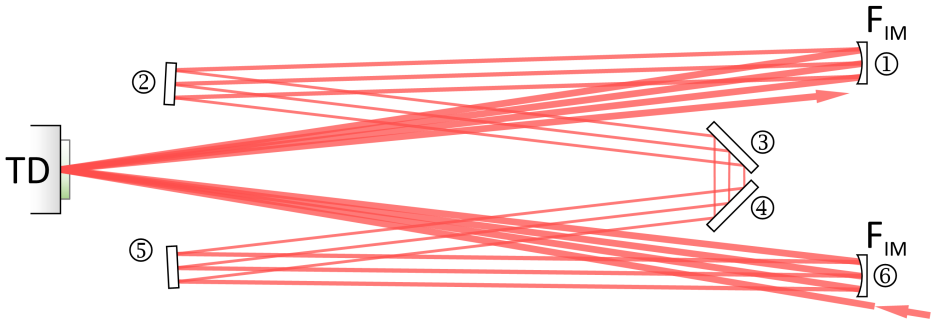

Figure 3.3: Schematic of an active multipass cell. The mirrors F_{IM} correspond to the focusing elements of the imaging arrangement in fig. 3.2. The laser beam is illustrated in red and starts at the bottom right. After its first reflection at the thin-disk it propagates along mirror 1 to 6, before it is imaged onto the disk again. This is repeated multiple times with one set of optics.

by the first curved mirror, because the thin-disk is one focal length away from this first curved mirror. One can then propagate the parallel beams at will for a distance d, before the second curved mirror makes them overlapping again on the thin-disk. The beams overlap on the thin-disk, because the second curved mirror is also one focal length away from the thin-disk. This is the macroscopic action of the arrangement on the beam alignment, which can be understood by regarding the laser beams as rays in geometrical optics.

In parallel to this beam steering, the laser beam also undergoes an evolution in diameter and divergence as it propagates through the AMC. The laser beam starts with a specific q-parameter right after the disk, propagates along the mirrors of the AMC back to the thin-disk, bounces off the thin-disk and ends up with the same q-parameter right after the disk. Thus, the diameter and divergence of the laser beam also remain the same on the disk. Somewhere along the way, however, the beam experiences a focus. The exact location of this focus depends on the beam which is sent into the AMC, but typically the beam undergoes a focus between the two concave mirrors. Therefore, each pass through the AMC adds one focus. This is a shortcoming from the perspective of nonlinear phase prevention and may negatively affect the peak power. An example of the evolution of the laser beam as it propagates through multiple imaging arrangements will be seen in subsection 3.5.1, fig. 3.5.

Each reflection on the thin-disk elongates the total length of the AMC and, therefore, the length of the laser cavity. This does not affect the beam caustic within the cavity, but it leads to a reduction in repetition rate. This side effect of the additional reflections on the thin-disk supports the realization of higher peak powers by reducing the risk of a limitation in average power, as it was discussed on page 37.

With appropriate optics, up to 11 reflections on the thin-disk have already been demonstrated in one AMC [99]. This large number of reflections provided the gain for an output coupling rate of 72 % and led to the oscillator of reference [99] in table 3.1.

3.4.3 Questions Addressed in this Chapter

As stated in section 3.3, the development goal is to optimize the peak power of a thin-disk oscillator at its typical pulse durations. Furthermore, the repetition rate is considered a secondary parameter and it is desired to operate the system in ambient air.

These goals could be fulfilled with the AMC-concept introduced in sections 3.4.1 and 3.4.2, because it might make a major fractions of the ≈100 MW intracavity peak power of Kerr-lens mode-locked oscillators in ambient air accessible. This concept was, however, only demonstrated for SESAM mode-locked thin-disk oscillators so far. Therefore, the question arose whether it is possible to combine Kerr-lens mode-locked operation with the AMC-concept and to push the performance frontier in this way.

The answer to this is not trivial. A potential obstacle for this union might arise from the dependence of the self-amplitude modulation on the position within the stability zone and the increased influence of thermal variations in the thin-disk on the stability zone. This can be a problem for KLM oscillators, because the self-amplitude modulation of those is much more dependent on their location within the stability zone than the self-amplitude modulation of SESAM oscillators. Thermal variations during mode-lock buildup could, therefore, act via the stability zone of the cavity onto the self-amplitude modulation and prevent mode-locked operation in this way. Furthermore, it is unclear if the intracavity peak power can be maintained with the AMC and its additional foci and nonlinear contributions in air.

Therefore, it was necessary to search for the answers in an experimental realization. The perspective of powerful oscillators in ambient air made it worth attempting.

3.5 Experiments and Findings

3.5.1 Scaling Behavior of the Oscillator with Imaged Thin-Disk Passes

A preparatory experiment was performed before the experimental realization of the KLM thin-disk oscillator with imaged thin-disk passes to assess the perspective of this endeavor. In this assessment, the number of reflections on the thin-disk in an oscillator was increased from 2 to 3 with the help of flat mirrors. Mode-locked operation was possible for this test oscillator. Its intracavity peak power remained at a usual level and operation with a record-high output coupling rate of 30 % was possible. Accordingly, a moderate performance improvement was achieved with the additional reflection on the thin-disk. This positive first assessment was part of my master's thesis [90].

Encouraged by the positive first assessment, the development was started. A well-known cavity was used as the starting point for the integration of the AMC. In this cavity, the focus for the Kerr-medium (the Kerr-telescope) was formed by two concave mirrors with a ROC of 1.0 m. A 3.0 mm thick sapphire plate placed under Brewster's angle served as the Kerr-medium. The thin-disk, purchased from TRUMPF, had a conventional thickness of

about 0.1 mm and was specified to have a ROC of about 16 m in the unpumped state. The pump spot diameter, observable due to the visible fluorescence, was estimated with the help of a CCD camera to be 3.4 mm. The path lengths in the cavity were roughly 33 cm from the end mirror to the Kerr-telescope, 130 cm from the telescope to the thin-disk and 275 cm from the thin-disk to the output coupler. This cavity with only one reflection on the thin-disk operated with an intracavity peak power of about 75 MW. Into this cavity, an active multipass cell was integrated.

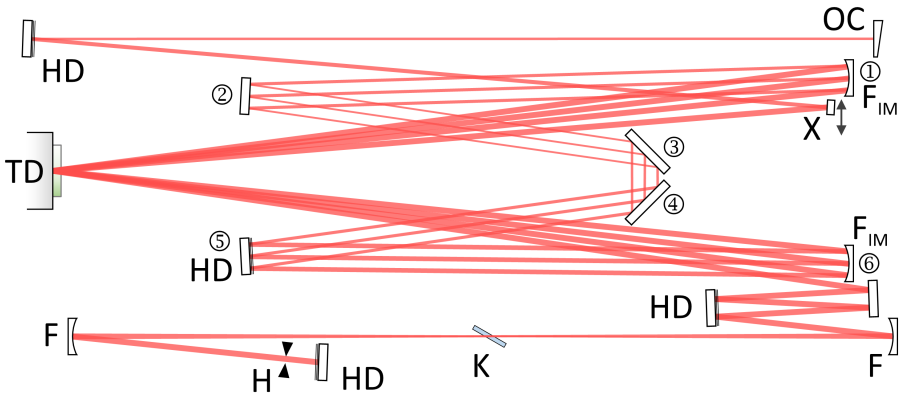

Figure 3.4: Schematic of the oscillator with active multipass cell. The abbreviations are: OC, output coupler; HD, high-dispersion mirror; TD, thin-disk; F, concave mirror of the Kerr-telescope; H, hard aperture; K, Kerr-medium. The placement of mirror X adjusts the number of AMC-passes. Non-labeled components are highly reflective mirrors.

The active multipass cell was built with two concave mirrors of 75 cm focal length. The cell mirrors were one inch in diameter except for a pair of 1.5-inch 45° mirrors. These 45° mirrors and the concave mirrors were placed on translation stages to allow an adjustment of the distances in the AMC. The development process for those components resulted in the oscillator configuration shown in fig. 3.4. As depicted in this illustration, the laser beam of the cavity started at the end mirror next to the hard aperture, propagated through the focusing section for the Kerr-medium, made two bounces on a pair of mirrors and finally reached the thin-disk for its initial reflection. The laser beam then entered the AMC by propagating towards the concave mirror number 1. From there, it followed the sequence from mirror number 1 to mirror number 6 before it was imaged onto the thin-disk again by the second concave mirror (mirror number 6). The position of the pick-off mirror X defined if and how many passes through the AMC were made by the laser beam. From this pick-off mirror, the laser beam was guided to the output coupler, which completed the respective cavity. The number of reflections on the thin-disk could be tuned between 1 and 4 with the positioning of this pick-off mirror X, without major modifications of the laser-beam evolution in the rest of the cavity. This means that the laser pulse propagated up to $4 * 2 * 2 = 16$ times through the disk thickness per round trip. The number of passes through the AMC was limited by the diameter of the optics used and by the size of the

laser beam on those optics.

An estimation of the beam-radius evolution within the cavity can be seen in fig. 3.5. The estimation is based on the $ABCD$ matrix formalism and CW operation, and does not include the Kerr-medium. In the current implementation, the laser beam has the foci of the AMC somewhere between mirror 2 and 3 in fig. 3.4. This should be kept in mind for future optimizations. Figure 3.5 illustrates the principle that the laser beam finishes each pass through the AMC in the way it started it. This can be seen by comparing the radii and slopes around the dashed vertical lines in fig. 3.5.

The dispersive mirrors in use were in-house coated HD73 mirrors with a dispersion of -3000 fs² per bounce in the wavelength range from 1025 nm to 1037 nm. It was necessary to select specific exemplars from these mirrors that could be used based on their individual spectral response. This selection was necessary, because those mirrors are rather narrow-band and small coating variations can shift their spectral response away from the targeted wavelength. One of those dispersive mirrors was incorporated into the AMC to achieve the needed dispersion of -39 000 fs² for the configuration with four reflections on the thin-disk. This spatial proximity of GDD to the SPM generation in the foci of the AMC influences the pulse dynamics within the cavity [118] and is perhaps beneficial.

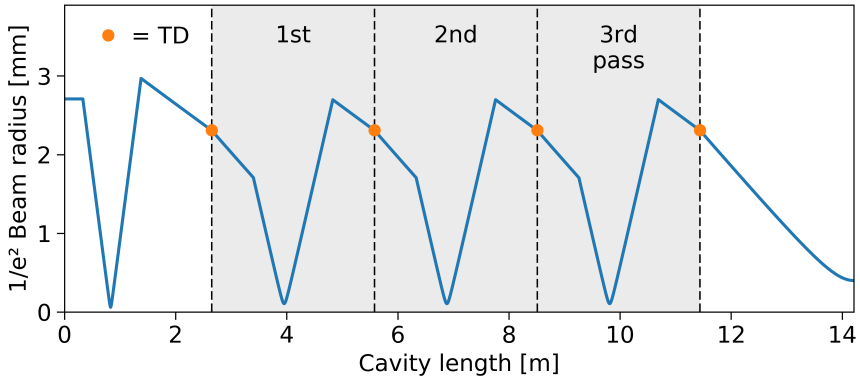

Figure 3.5: Estimated beam-radius evolution in the laser cavity with three passes through the active multipass cell. The AMC is shown against a gray background. The dashed, vertical lines separate the individual passes. TD denotes thin-disk.

A picture of the oscillator can be seen in fig. 3.6. The oscillator was built in a massive aluminum housing with outer dimensions of 70 cm $*$ 140 cm. Such a housing contributes to the long-term stability of the oscillator and is still transportable. During mode-locked operation, the housing was closed with lids to shield the oscillator against air turbulences.

The development strategy for this oscillator was to find and optimize mode-locked operation for a gradually increasing number of reflections on the thin-disk. The most important parameters for this task were the amount of deployed pump power, the length of the Kerr-telescope (as introduced on page 19), the Kerr-medium position (also in mode-locked operation), the alignment of the cavity, the amount of GDD and the hard aperture size. A partial optimization of these parameters was performed before another pass through

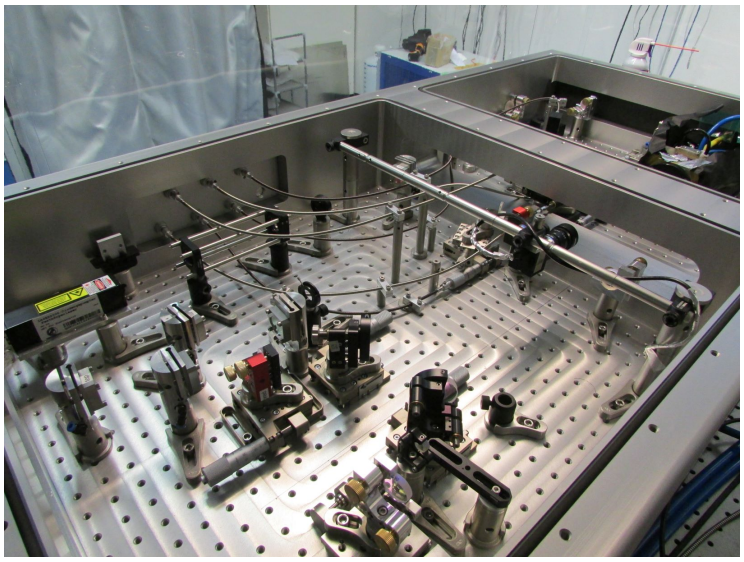

Figure 3.6: Picture of the oscillator. The thin-disk mount is located in the upper right corner of the picture next to the blue hose and is barely visible. The bent shafts near the center of the picture are mechanical remote controls, which allow an adjustment of the cavity while the housing is covered with lids.

the AMC was added. Initially, this procedure was repeated for gradually increasing output coupling rates until, at some point, it was possible to work only on the configuration with four reflections. For this configuration, a hard aperture with a diameter of 4.4 mm has delivered the highest peak powers.

Table 3.2 summarizes some of the results, which have been obtained during this exploration and optimization process. The first four entries of this table show the mode-locked performance for a rather high output coupling rate of 21 % and different numbers of thin-disk reflections. The first entry with only one reflection seemed to suffer from its unfavorable combination of gain and loss, as it required a high pump power for its operation. The maximum in optical-to-optical efficiency over the number of reflections in the first part of the data could be due to the shift in optimum output coupling rate with growing gain. This behavior was found in simulations of CW operation in reference [118]. In these simulations, the maximum reachable efficiency value shifted to larger output coupling rates for a growing number of thin-disk reflections. Accordingly, the configuration with two reflections seems to be near its optimum output coupling rate with the tested 21 %. These 21 % would then be too low for the configuration with three and four reflections and could therefore explain why the efficiency is lower for those configurations.

It appears plausible that multiple reflections on the thin-disk should introduce the soft-aperture effect multiple times and should thereby have the ability to improve or, if implemented incorrectly, undermine hard aperture mode-locked operation. This holds great potential for future optimizations of Kerr-lens mode-locked thin-disk oscillators. However, the presence of such an effect is not yet visible in the data of table 3.2. It takes probably

a specially designed experiment to probe the existence of this effect.

Table 3.2: A selection of the mode-locked performances. The asterisk indicates that the value was corrected downwards to account for a potential beam clean-up. The term η_{OO} denotes the optical-to-optical efficiency.

Reflections on TD	OC [%]	GDD [-fs^2]	τ_p [fs]	P_{Out} [W]	η_{OO} [%]	$P_{PeakInt}$ [MW]
1	21	21 000	325	72*	21*	34*
2	21	27 000	250	75*	28*	71*
3	21	33 000	250	60*	23*	75*
4	21	39 000	265	50*	19*	74*
4	29	39 000	265	71*	27*	77*
4	40	39 000	265	106*	27*	83*
4	50	39 000	290	140	27	80

The four last entries of table 3.2 document the change in performance as the oscillator's output coupling rate is raised. It is remarkable that the pulse duration and internal peak power did not degrade much with growing output coupling rate. Also, with the AMC, the oscillator was able to reach the typical intracavity peak power of this arrangement of about 75 MW.

The configuration with an output coupling rate of 50 % delivered the best performance. Only during the last experiments with this configuration was a disadvantageous transverse feature noticed that accompanied the emitted beam profile. This feature seemed to originate from diffraction at the hard aperture within the cavity and needed to be clipped away by an additional external hard aperture for beam quality improvement. This led to a reduction in output power by 8 %. The values with an asterisk in table 3.2 were reduced by this amount to take this potentially necessary beam cleaning into account.

3.5.2 Final Oscillator Performance

The performance of the oscillator configuration with an output coupling rate of 50 % is presented in detail in this section.

As mentioned, the emitted beam of this oscillator was accompanied by a faint circular pattern. This beam profile is documented in fig. 3.7. The surrounding pattern degraded the focus of the beam considerably. This was mitigated with an external hard aperture and a power loss of 8 %.

The average power measured after this second external hard aperture was 140 W. This power was generated with an optical-to-optical efficiency of 27 %. The oscillator with its four reflections on the thin-disk operated at a repetition rate of 10.6 MHz, which results in a pulse energy of 13.2 µJ.

The pulse duration of the generated pulses was determined with a commercial autocorrelator (pulseCheck, APE GmbH). The recorded data and the corresponding autocorrelation

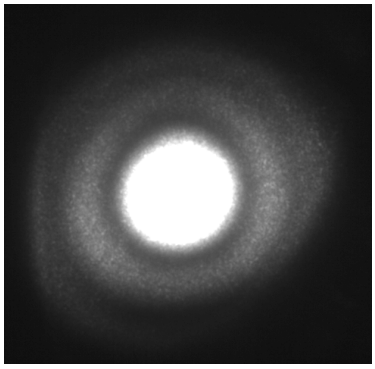

Figure 3.7: A picture of the emitted far field beam profile on a detector card. The beam in the center is surrounded by a faint, undesired, circular pattern.

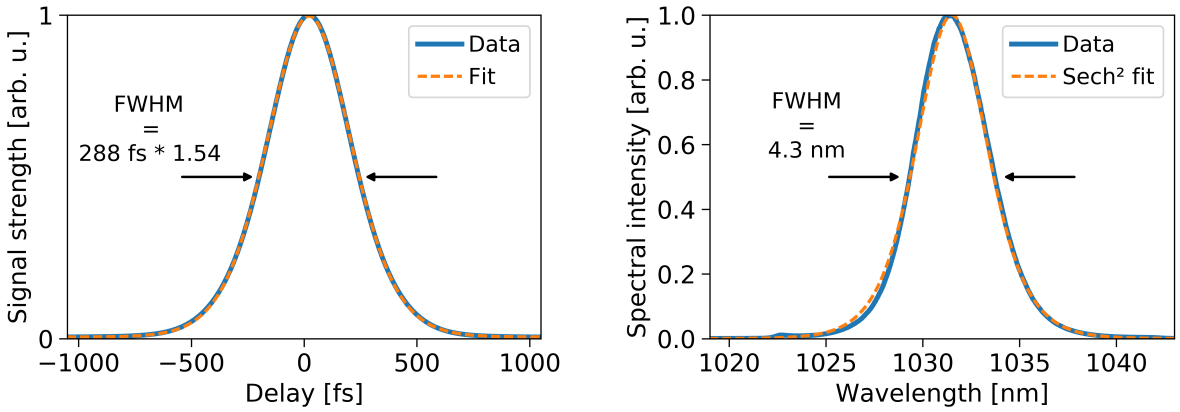

a) b)

Figure 3.8: a) Measured autocorrelation data and its fit for the mode-locked oscillator. b) Spectral data and its fit for the mode-locked oscillator.

fit for a $sech^2$-shaped pulse are displayed in fig. 3.8a. This measurement determined the pulse duration to be about 290 fs.

The recorded spectrum in fig. 3.8b, with its lack of spectral spikes, confirms that no CW radiation was part of the emitted power. The recorded spectral shape agrees well with the assumption of a *sech*-shape of the field in the temporal domain. It has a spectral width of 4.3 nm. This spectral width results together with the measured pulse duration in a time-bandwidth product of 0.351 instead of the theoretically expected 0.315. This could be due to a slight chirp, which results from the variation in pulse energy and associated SPM generation during the round trip [118]. The measured spectrum supports a Fourier-transform-limited pulse duration of 260 fs. No attempt was made to compress the pulses to this limit.

The measured pulse energy together with the measured pulse duration result in 40 MW emitted peak power for this oscillator.

The beam quality of the emitted radiation was characterized with a commercial M^2-meter (CinSquare CS200, CINOGY Technologies GmbH) after the additional external hard aperture. The M^2-values were measured to be 1.09 $\pm$0.02 and 1.06 $\pm$0.01 in two orthogonal directions.

A risk for oscillators in the negative dispersion regime is that the oscillator can emit multiple pulses per round trip. Therefore, it was necessary to check if the stated power was emitted as a pulse train of individual pulses. The presence of any accompanying satellite pulse on short timescales was ruled out with the help of a home-built long-scan autocorrelator and independently with an optical spectrum analyzer. The presence of additional pulses on the long timescale was ruled out by monitoring the pulse train with a 175-ps-rise-time photodiode on a 3.5 GHz oscilloscope. In this way, it was confirmed that the pulse train consisted only of individual pulses.

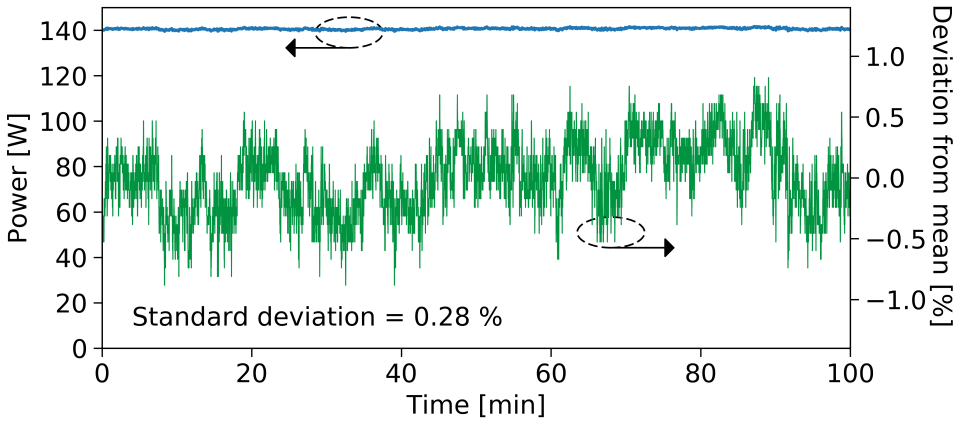

Figure 3.9: Long-term power stability measurement of the mode-locked oscillator. The upper blue line depicts the power reading. The green line in the middle presents the relative deviation of the power from its mean power.

Power fluctuations on a short time scale were characterized with the measurement of

the square root of the integrated relative intensity noise (integrated RIN_{rms}). For this measurement, a fraction of the beam was sent onto a photodetector (PDA20CS2, Thorlabs GmbH). The electrical signal, after filtering out the DC component, was analyzed with an RF spectrum analyzer (E4447A, Agilent). The evaluation of the measured intensity noise resulted in an integrated RIN_{rms} of 0.0545 % for the range from 10 Hz to 1.25 MHz. The underlying calculation is described in appendix A. The data of this RIN measurement was provided by my colleague Sebastian Gröbmeyer.

The long-term power stability of the oscillator is presented in fig. 3.9. For this measurement, the emitted power of the oscillator was recorded with a thermopile power sensor (Plus2, LaserPoint s.r.l.) for 100 minutes. The measurement shows a stable power level of the oscillator with a standard deviation of 0.3 % from its mean value. This data was sampled at a rate of 4 Hz.

The oscillator is also stable on a much longer time scale. It is operational on a daily basis for three years by now and this without damages on intracavity optics or major degradation.

Besides the beam profile, the oscillator showed another unusual behavior. Mode-locked operation was typically initiated at an output power of about 100 W with a pronounced CW feature. The CW feature was then removed by increasing the pump power and thereby raising the output power to 140 W (which corresponds to an intracavity power of about 280 W). This is surprising because a CW feature is usually an indication of an excess of energy within the cavity and should be removed by reducing the pump power. The transition from mode-locked operation with CW feature to pure mode-locked operation was most likely caused by varying thermal lenses within the cavity, which modified the position of the cavity within the stability diagram. In this way, a thermal lens can influence the self-amplitude modulation, as discussed before on page 19. Detailed, additional studies would be needed to clarify the circumstances behind this atypical removal of the CW feature.

3.6 Chapter Summary and Outlook

This chapter reported on the successful union of Kerr-lens mode-locking with the active multipass cell concept. Kerr-lens mode-locked operation with multiple reflections on the thin-disk was not prevented by the increased influence of thermal variations in the thin-disk. The additional gain provided by the additional reflections on the thin-disk allowed mode-locked operation with an output coupling rate of up to 50 %. This is currently the highest demonstrated output coupling rate for Kerr-lens mode-locked thin-disk oscillators. The corresponding performance makes it the most powerful oscillator in terms of emitted peak power under ambient conditions. A comparison with other oscillators was given in table 3.1. The obtained record-performance was published in a peer-reviewed journal [102]. The oscillator is now operational for three years with no signs of irreversible degradation.

A very encouraging finding is that the oscillator with the active multipass cell was able to maintain its initial intracavity peak-power level. This finding makes promises for further peak-power scaling by integrating the AMC-concept into evacuated thin-disk oscillators,

where additionally any detrimental influence of the additional foci in the AMC would be nullified. Thus, based on the peak powers demonstrated for evacuated oscillators [98] and the 50 % output coupling rate demonstrated in this thesis, emitted peak powers on the 200 MW scale could become reality. This finding also recommends AMCs for gain-limited gain media, because these would equally benefit from the 2 to 4 times [118] higher output coupling rates.

In a future implementation of an active multipass cell, one would free oneself from the self-imposed constraint to build a symmetric AMC-arrangement. With the so gained freedom, one would try to achieve the largest possible separation between the foci in the AMC and its mirrors. This would reduce the danger of damages and potential nonlinear effects in the mirrors and might be required for further power scaling. One could then also attempt to work without the 45° mirrors in the AMC, because 45° mirrors perform intrinsically weaker for the present p-polarization in terms of reflectivity and dispersion. The replacement of the 45° mirrors with one flat mirror would also free some space between the concave mirrors and thereby allow to reduce the astigmatism experienced on the thin-disk. Furthermore, one would also remove the double pass on the flat mirrors before the AMC, as the amount of needed dispersion is now much better known. One would also organize larger mirrors for the AMC, such that one can afford more distance to the edges of the mirrors and has the possibility to realize even more reflections on the thin-disk. Further dispersion optimization with broader, reliably known mirrors might enable a reduction in pulse duration. A variation of the Kerr-medium thickness might optimize the performance too, as this parameter has not been studied. There is, therefore, room for future optimization and peak-power scaling.

The demonstrated oscillator with its average power of 140 W, pulse duration of 290 fs and peak power of 40 MW is already a step forward in comparison to other oscillators operated in air. For example, the existing and so far only Infrasampler commissioned for sample analysis is based on the oscillator from the preparatory study. This oscillator from the preparatory study drives the experiment with an average power of 100 W, a pulse duration of 220 fs and a peak power of 14 MW. Colleagues have compressed this output in Herriott cells to an average power of 60 W and a pulse duration of 16 fs [20, 88], which can generate 50 mW of mid-IR radiation in the wavelength range from 6.5 µm to 11 µm [20, 27]. Extrapolating this performance, the new oscillator can generate ≈150 mW of mid-IR radiation despite its lower repetition rate (10.6 MHz instead of 28.3 MHz [88]), under the assumptions that the mid-IR generation scales quadratically with peak power (eq. (2.65)) and that the initial advantage in peak power is preserved during compression. This is the reason why colleagues recently started to build a new Infrasampler (Infrasampler 1.6) based on the oscillator presented here.

Chapter 4

Ho:YAG Thin-Disk Oscillator

4.1 Motivation for the Development of a 2 µm Thin-Disk Oscillator

In the previous chapter on the development of a 1 µm laser for IDFG, the idea was to scale the mid-IR output by using driving lasers with even more peak power. This approach is, however, not the only way in which the mid-IR generation can be optimized. For example, one can change to a 2 µm driving source. This change in wavelength brings a couple of advantages for the generation of mid-IR radiation.

First of all, it doubles the fundamentally possible upper conversion efficiency, as discussed in eq. (2.62). Further, the change in wavelength enables the use of nonlinear crystals with larger nonlinearity. Empirical data shows that high nonlinearity comes together with a low bandgap of the crystal [119]. Short pump wavelengths lead to two-photon absorption for a low bandgap, because two-photon absorption can occur when the laser photon energy hc/λ_p is larger than half of the bandgap $hc/\lambda_p > E_{gap}/2$ [34, 120]. This two-photon absorption process is disadvantageous because it can lead to material damages or a reduction in conversion efficiency. Therefore, longer pump wavelengths are required for crystals with high nonlinearity.

Table 4.1 compares some of the frequently used crystals for IDFG in terms of transparency and the figure of merit d^2/n^3 to show the advantage of such highly nonlinear crystals. The figure of merit d^2/n^3 was calculated in reference [34] with an average nonlinearity d and a mean refractive index n [34]. This type of figure of merit was motivated in the context of eq. (2.66).

The first column of table 4.1 describes the crystal lithium gallium sulfide ($LiGaS_2$; colloquially LGS). It is one of the best nonlinear crystals for powerful, broadband mid-IR generation driven at 1 µm [76]. As motivated before, it has a relatively low nonlinearity, which is reflected by the low value of its figure of merit. For broadband mid-IR generation, it achieves an optical-to-optical conversion efficiency of only 0.2 % [76] with respect to the average power of driving pulses with a peak power of 23 MW.

Crystals with higher nonlinearity and deeper transparency into the mid-IR become

usable for 2 µm driving pulses. One such example is gallium selenide (GaSe) in column two of table 4.1. It has an approximately 50 times larger figure of merit and a transparency up to 19 µm. Two-photon absorption is prevented in GaSe for wavelengths longer than 1.24 µm [120]. Another very promising crystal is zinc germanium phosphide (ZnGeP2; colloquially ZGP). The pump wavelength for this crystal should lie above 2 µm due to residual linear absorption [34]. For ZGP, the nonlinearity is again larger than for LGS, and ZGP is at least as transparent as LGS. Driving sources at 2 µm promise, therefore, a more efficient

Table 4.1: Comparison of IDFG crystals for 1 and 2 µm driving pulses. Figure of merit values d^2/n^3 are taken from reference [34] and serve as a rough assessment of the nonlinearity.

	LGS	GaSe	ZGP
Driving wavelength [µm]	≈1	≈2	≈2
Transparency [µm]	0.32 – 11.6	0.62 – 19	0.74 – 12
d^2/n^3 [pm^2 V^{-2}]	3	156	181
Reference	[34, 121]	[34, 120]	[34, 122]

and possibly broader mid-IR generation, as will be seen at the end of this chapter and at the beginning of chapter 5.

Another aspect of the change in wavelength is the electro-optic sampling. In the current Infrasampler design [20], the driving laser is also used for the electro-optic sampling and this EOS is affected in its performance by the wavelength used in its sample beam. Changing the wavelength from 1 µm to 2 µm results in a broader phase matching and a stronger signal for the EOS of mid-IR fields, due to the dispersion properties of typical EOS crystals like GaSe. The more favorable dispersion obtained allows the use of thicker detection crystals without compromising the detection bandwidth and thus increases the signal strength for a given detection bandwidth [123].

Therefore, many reasons motivate a change in driving wavelength to the 2 µm region. Those reasons, together with the arguments promoting thin-disk oscillators (section 3.1), motivated the development of a 2 µm thin-disk oscillator. A promising gain material for this purpose is holmium-doped yttrium aluminum garnet (Ho:YAG), which will be introduced in the next section 4.2.

4.2 Properties of Ho:YAG as Laser Gain Medium

As mentioned in chapter 3 on Yb:YAG thin-disk oscillators, substantial effort was already devoted to the development of new 1 µm thin-disk gain media. However, hardly any of those media reached a competitive performance level because an effective operation in the thin-disk geometry requires a special combination of material properties.

The mechanical and thermal properties of a gain medium are largely determined by the host crystal. Therefore, a successful development becomes more likely if one sticks to an already established host material like YAG. In addition, the entire grinding process to

about 0.1 mm thickness can be copied from the fabrication of Yb:YAG thin-disks and does not require additional development. Holmium as dopant in YAG benefits from all these advantages.

The laser emission in Ho:YAG originates from a quasi-three-level system, which is the same type as in Yb:YAG. Ho:YAG emits, however, at about 2090 nm, as can be seen from the emission cross-section in fig. 4.1a. Its main emission feature has a FWHM width of about 15 nm, which supports some 300 fs pulses at this wavelength. The emitted wavelength makes Ho:YAG a suitable front-end for the very promising nonlinear crystal ZGP, because it lies above ZGP's absorption edge at about 2 µm.

The absorption cross-section of Ho:YAG in fig. 4.1b shows a few pronounced features. The highest feature is a relatively narrow absorption feature located at 1907 nm. However, at this wavelength lies also a water vapor absorption line. One can evade this water vapor absorption to a large extent by slightly shifting the pump wavelength to 1908 nm, where Ho:YAG still absorbs reasonably. The pump and laser wavelengths of Ho:YAG result in an equally low quantum defect as in ytterbium with pumping at 940 nm.

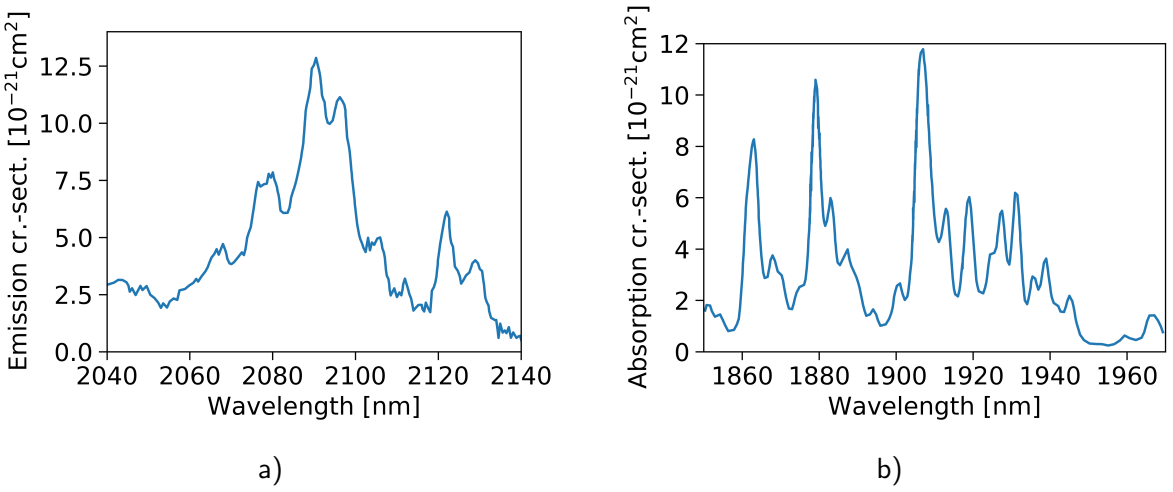

Figure 4.1: a) Emission cross-section of Ho:YAG. b) Absorption cross-section of Ho:YAG. The data was digitally extracted from reference [124].

Pump sources at the wavelength of 1908 nm are not widely available. Potential candidates are diode lasers, thulium-doped yttrium lithium fluoride (Tm:YLF) lasers and thulium fiber lasers. One would like to use affordable, high power diode lasers with a top-hat beam profile for the thin-disk application. However, available on the market are only 60 W diode laser modules (QPC Lasers Inc.). Thulium-based fiber lasers are the alternative with more power and more potential suppliers. Nevertheless, the choice is still rather limited because only a fraction of the suppliers offers their lasers at the wavelength of 1908 nm. The supplier IPG Photonics offers one of the most attractive fiber lasers. This laser has an average power of 120 W and costs about the same as the diode laser from QPC Lasers Inc. Therefore, thulium fiber lasers are currently the pump source of choice.

One serious shortcoming of Ho:YAG is the presence of a parasitic upconversion process, which involves two holmium ions in the upper laser state. They exchange energy such that one of them returns to the ground state and the other is promoted to an undesired higher state. This higher state is subject to a relaxation process, which reduces the chance of a reversal of the upconversion process and which takes away the corresponding excitation from the amplification process [125]. The probability for the upconversion to happen depends strongly on the proximity of the excited ions. Therefore, the upconversion rate depends on the doping concentration and on the population density in the upper laser state [125]. This is one reason why Ho:YAG-based bulk laser use about five times lower doping concentrations than Yb:YAG thin-disk lasers. The exact holmium concentration depends on the application. In q-switched bulk lasers, losses due to upconversion become significant at doping concentrations of about 1.5 % [126, 127]. For thin-disk oscillators, this value is higher, as will be discussed in the coming subsections.

The idea of realizing a Ho:YAG thin-disk technology is appealing. It is accordingly not an entirely new idea. This will be seen in the next section 4.3, where the state of the art of Ho:YAG thin-disks is reviewed.

4.3 State of the Art of Ho:YAG Thin-Disk Oscillators

Table 4.2 provides an overview of the Ho:YAG thin-disk oscillators in CW operation demonstrated so far. Its first entry describes the first realization of a Ho:YAG thin-disk. Since then, three other groups have worked on this topic, each roughly doubling the demonstrated output power. The achieved improvements in performance are probably due to better equipment and the change from I-shaped cavities to V-shaped cavities. This change in cavity configuration doubles the interaction between the intracavity laser beam and the thin-disk per round trip. The enhanced interaction results in more gain for the intracavity laser beam and is, therefore, beneficial for laser operation. The improvement of the equipment concerns the available pump power and the disk bonding-technique. The applied pump powers were higher in later experiments and the latest thin-disks were manufactured with TRUMPF's optimized bonding technology. More and cheaper pump power would support the further development of the demonstrated CW powers because the current thin-disk lasers do not exhaust their capabilities with the pump powers currently in use.

Zhang and other colleagues managed to demonstrate the second to last entry in table 4.2 [131] and realized mode-locked operation of a thin-disk at 2 µm for the first time [133]. These achievements initiated the experiments presented in this chapter. These experiments started at the end of the year 2017 and built on the previously [131, 133] gained knowledge.

The first mode-locked operation of a Ho:YAG thin-disk was a breakthrough for oscillators above 1.5 µm in terms of ultrashort pulses at high average power [133]. The so demonstrated mode-locked performances are listed in table 4.3. These Kerr-lens mode-locked operations were realized with different output coupling rates. Higher output coupling rates led to an increase in emitted peak and average power because the oscillator managed to maintain its intracavity peak power of about 30 MW.

Table 4.2: Overview of the developed Ho:YAG CW thin-disk oscillators. Listed are the cavity configuration, the doping concentration and thickness of the thin-disk, the output coupling rate, the emitted average power, the slope efficiency η_{Slope}, the optical-to-optical efficiency and the beam quality factor (if specified).

Cavity shape	Doping [%]	Thickness [mm]	OC [%]	P_{Out} [W]	η_{Slope} [%]	η_{OO} [%]	M^2	Year [Ref.]
I	2.0	0.4	2.1	9.4	40	36	5.2	2006 [128]
I	2.5	0.3	0.3	22	≈26	≈24	–	2015 [129, 130]
V	2.5	0.2	1.8	50	61	58	5.3	2018 [131]
V	2.0	0.19	3.0	96	43	46	1.1	2020 [132]

Table 4.3: Mode-locked performances of the Ho:YAG thin-disk oscillator reported in reference [133]. Listed are the applied pump power P_{Pump}, the output coupling rate, the emitted average power, the pulse duration, the emitted peak power, the optical-to-optical efficiency and the peak power within the cavity.

P_{Pump} [W]	OC [%]	P_{Out} [W]	τ_p [fs]	P_{Peak} [MW]	η_{OO} [%]	$P_{PeakInt}$ [MW]
56	1	5.8	220	0.3	10.4	30
72	1.8	12	230	0.6	16.7	33.3
83	3	18.4	220	0.96	22.2	32
114	4	25	270	1.06	22.0	26.5

The oscillator configuration which led to the results in table 4.3 had the following characteristics [133]. Its Kerr-telescope was formed by two concave mirrors with a radius of curvature of 100 mm. For mode-locked operation, this oscillator was operated in the second stability zone at the shorter edge with respect to the telescope length (as introduced on page 19). As Kerr-medium, a 1 mm sapphire plate under Brewster's angle was used. Dispersive mirrors with a total round-trip dispersion of -16 000 fs^2 were incorporated into the cavity. Two thulium fiber lasers with a wavelength of 1908 nm generated a pump spot of about 3 mm diameter on the thin-disk after being transferred through a multimode fiber with a core diameter of 550 µm. The multimode fiber was used to degrade the beam quality factor of the pump light and thus prevent small foci in the pump head, which may cause damage to the optics, and to obtain a top-hat beam profile [131]. The thin-disk in use had a thickness of 200 µm and a doping concentration of 2.5 %. The disk was mounted on a flat diamond substrate and had a residual curvature of about 20 m in the unpumped state. The curvature in the pumped state should not differ much from this. The cavity was arranged with flat mirrors in such a way that the intracavity laser beam was reflected twice at the thin-disk. The lengths of the cavity were roughly 58 cm from the end mirror to the thin-disk, 40 cm from the first reflection at the thin-disk to the second reflection, 41 cm from the second reflection to the Kerr-telescope and about 45 cm from the telescope to the output coupler.

Both tables 4.2 and 4.3 showed that Ho:YAG oscillators typically operate best with only a few percent of output coupling. The next subsection 4.3.1 will introduce the open questions addressed in this chapter. Some of these questions will deal with the current low output coupling rates.

4.3.1 Goals and Questions Addressed in this Chapter

One scaling approach for Ho:YAG thin-disk oscillators is the operation with higher output coupling rates. Table 4.3 in the previous subsection demonstrated that the realization of higher output coupling rates is a rewarding route in terms of performance if the system can maintain its intracavity performance. The effectiveness of this scaling approach was also already seen in chapter 3, and the approach is particularly promising for the low output coupling rates present in Ho:YAG systems, as they offer room for significant improvement.

Another reason for the pursuit of higher output coupling rates is that even moderate cavity losses of, for example, 0.5 % represent a significant fraction in relation to low output coupling rates (a seventh for 3 %, a third for 1 %). This large share limits the efficiency of the system. Thus, it is rewarding to minimize the cavity losses and to push the output coupling rate to higher values, such that one extracts more of the available power through the output coupler.

Therefore, one wants to realize higher output coupling rates by increasing the gain within the cavity. It was intended to achieve this additional gain by optimizing the doping concentration and thickness of the disk because these parameters had not been thoroughly investigated before. The use of an active multipass cell is a promising next step after the optimization of the thin-disk.

A higher doping concentration and a larger thickness of the disk enhance the pump absorption and the laser amplification of the thin-disk. The higher disk thickness comes, however, together with an increase in temperature and temperature gradient. The higher temperature reduces the population inversion because the lower laser level is thermally more populated. The higher temperature gradient leads to more thermal lensing and other wavefront distortions. A higher doping concentration, in turn, enhances the upconversion process because the excited ions can be located closer to each other. The enhanced upconversion process can limit the population inversion and reduce the efficiency of the laser [125]. It was, therefore, not clear where the optima for these two parameters are.

Publications on Ho:YAG lasers with thin-disk geometry did not indicate an upper limit for the doping concentration, nor did they specify an optimum disk thickness at the time of this thesis' experiments. The study of literature on Ho:YAG lasers with bulk geometry was also not very helpful. Those publications report on operation with doping concentrations in the range of 0.5 % to 2 % [126, 134]. These low concentrations did not agree with the positive impression that doping concentrations of 2 % and 2.5 % made in the thin-disk geometry [128, 131]. That is why one wanted to test higher doping concentrations.
No data was available on the optimum disk thickness, because references [131, 133] were the first use of TRUMPF's proprietary bonding technique for Ho:YAG and it was considered possible that this bonding technique leads to a different optimum due to a better thermal contact. Therefore, one goal was to test and optimize the thickness and doping concentration of thin-disks bonded by TRUMPF.

The oscillator in reference [133] was not only the first mode-locked Ho:YAG oscillator, but also the first Ho:YAG oscillator in our group. Accordingly, one hope was to make this type of oscillator stabler and more reliable by improving its technical implementation. Therefore, another goal was to duplicate the oscillator prototype in a technically well-implemented form and then to surpass the demonstrated performance.

It was envisioned to accomplish this performance improvement either by the use of an optimized thin-disk or by the operation of the oscillator under a modified atmosphere. The latter approach was already introduced in subsection 3.4.1 as a peak-power scaling approach in Yb:YAG thin-disk oscillators.

By the proposed modification of the oscillator's atmosphere, one can make sure that the intracavity peak power is not limited by the generation of too much nonlinear phase-shift in air, as discussed earlier in subsection 3.4.1. Thus, an evacuation of the oscillator chamber allows one to exclude an intracavity peak-power limitation as a limitation of the oscillator performance. A limitation might be present in Ho:YAG, because the demonstrated 30 MW of internal peak power are rather low.

In addition to the exclusion of a limitation in peak power, the modification of the oscillator's atmosphere would remove the residual influence of water vapor absorption. This should increase the efficiency of the system and contribute to its stability by reducing the heating up of the air in the beam path and, therefore, of the entire laser system. Therefore, one requirement was that the well-engineered implementation of the new oscillator supports the evacuation of the oscillator chamber.

For quite some time, the only thin-disk in question for the implementation of this

second oscillator was, however, a curved thin-disk instead of a flat one used in the original demonstration. This had quite some consequences for the mode-lock-ability of the cavity, as will be explained later in subsection 4.4.2. This circumstance raised the question of whether one can mode-lock the cavity from reference [133] if it contains a curved disk. The development of a new cavity design was regarded as riskier and more time-consuming.

These were the development goals and open questions for Ho:YAG. They will be addressed and discussed in the next section 4.4.

4.4 Experiments and Findings

4.4.1 Doping Concentration and Disk Thickness Optimization

The implementation of state-of-the-art thin-disk technology depends on industry partners. In this thesis, the industry partners were LAYERTEC GmbH, for the polishing and coating of the disk blanks, and TRUMPF Laser GmbH for the bonding and auxiliary technologies.

Although large parts of the manufacturing process could be copied from Yb:YAG, many unexpected obstacles still had to be overcome. In the course of this project, it happened, for example, that a disk was erroneously mounted on a curved instead of a flat diamond substrate or that a batch of disks was too strongly curved for bonding to flat diamond substrates due to coating induced stress. Sometimes those incidents can reveal interesting physics, such as a quadratic dependence of the disk blank curvature on the disk thickness (from ROC≈280 mm at 100 µm thickness to ROC≈2500 mm at 300 µm), but primarily these incidents delay progress.

Once one has the required components, one can start with implementing the first experiment — in this case, the investigation of CW performance. This performance was investigated in multimode operation for comparability with the publications of table 4.2. To this end, a pump spot of about 2.3 mm diameter was generated on the thin-disk under investigation. The pump light with a wavelength of 1908 nm was supplied by a 120 W thulium fiber laser from IPG Photonics. This laser's emission was coupled into a multimode fiber with a core diameter of 550 µm using a lens with a focal length of 150 mm. On the other end of the fiber, the pump light was collimated with two lenses with focal lengths of 15 mm and 20 mm before the pump light was $4f$-imaged into the pump head.

In one series of experiments, the influence of the doping concentration on the laser performance of 100-µm-thick thin-disks was investigated. For better readability, the 100-µm-thick thin-disks are referred to as 100 µm thin-disks in the following. A disk thickness of 100 µm was investigated because this thickness or even thinner is a typical thickness for Yb:YAG thin-disks. Three 100 µm thin-disks with doping concentrations of 2.5 %, 4 % and 6 % were sequentially tested for their performance in terms of output power in a V-shaped cavity. A concave mirror with a ROC of 800 mm formed one end of this V-cavity. A flat output coupler was located at the other end of this V-cavity. The lowest available output coupling rate of 1 % was found to be the ideal output coupling rate for all 100 µm thin-disks. The cavity itself was kept as short as possible in order to assist energy extraction by

the presence of higher-order transverse modes. Consequently, each cavity mirror was only about 2 cm away from the pump head. The resulting cavity had a calculated fundamental transverse mode that was about 2.5 times smaller than the pump spot. This diameter mismatch led to the desired multimode operation.

A representative selection of the so obtained output power trends is displayed in fig. 4.2a. This figure shows that the performance is worse for the higher doped disks. The determination of their performances was even discontinued at some point due to their poor performances in comparison to the thin-disk with a doping concentration of 2.5 %. The upper limit in doping concentration is now, after this experiment, located in the range from 2.5 % to 4 %. A further restriction of this value range is given by reference [135], which was published in the middle of the year 2018. The data in this reference suggests a decline in performance already for a doping concentration of 3 %. Given the good performance reported in reference [132] for a doping concentration of 2 %, the ideal doping concentration is now expected to be in the range of 2 % to 3 %.

The thickness of the thin-disk was the other promising parameter for performance improvement. Therefore, a set of thin-disks, with a doping concentration of 2.5 % and thicknesses of 100 µm, 200 µm and 300 µm, was tested in the same manner as before. A minor shortcoming of this investigation is that the 200 µm thin-disk was erroneously mounted on a curved diamond substrate and, therefore, had a ROC of 2 m. The other two disks were essentially flat, as initially intended, with a ROC greater than 20 m. It was attempted to minimize the consequences of this difference in curvature by ensuring that the obtained cavities support similar multimode operation. The diameters of the fundamental transverse modes differed in the used cavity arrangement by only 10 % at the thin-disks. This is a small difference in comparison to the much larger pump spot and should ensure comparability.

Figure 4.2b displays some of the collected output power trends. The displayed data were recorded with an output coupling rate of 3 % and highlight the different potentials for operation with high output coupling rates. The data show that the 200 µm thin-disk performs best. The gentle rollover of the 300 µm thin-disk might be due to its stronger heating up, which can provoke the earlier (subsection 4.3.1) mentioned disadvantageous effects.

The 200 µm thin-disk delivered the best performance in general. The respective best performances of the thin-disks with a doping concentration of 2.5 % are listed in table 4.4. Those performance values were found after testing different output coupling rates and cavity arrangements for each thin-disk. Output coupling rates higher than 3 % were not tested for the 300 µm thin-disk because the power improvement was less than 2 W in the step from 1.8 % to 3 % output coupling. This trend gave too little hope for an outperforming of the 200 µm thin-disk, which laid 8 W ahead.

In conclusion, the best CW operation was obtained for the 200 µm thick thin-disk with a holmium doping concentration of 2.5 %. The corresponding efficiency values are comparable with the flat but otherwise equal disk from reference [131], which is a positive first quality check. The output power of this thin-disk showed only a very modest rollover with the applied pump power (fig. 4.2b). Therefore, it should be possible to reach the

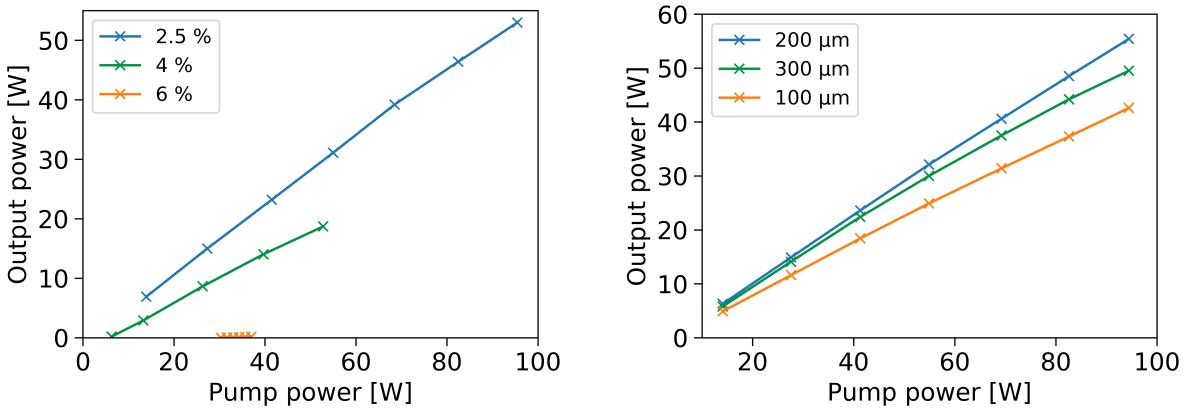

a) b)

Figure 4.2: Emitted power over applied pump power recorded for a) thin-disks with a thickness of 100 µm, but different doping concentrations. The output coupling rate was 1 %. b) thin-disks with a doping concentration of 2.5 %, but different thicknesses. The output coupling rate was 3 %.

Table 4.4: Best CW performances for 2.5 % Ho:YAG disks with different thicknesses.

Thickness [µm]	ROC_{Disk} [m]	OC [%]	P_{Out} [W]	η_{Slope} [%]	η_{OO} [%]
100	20.5	1.0	53.0	56.8	55.5
200	2.0	1.8	57.4	63.2	60.8
300	23.0	3.0	49.5	54.5	52.4

100 W-power level of the most recent publication in the literature [132] by applying the same amount of pump power. Open is the question, if the disk and pump technology at hand can deliver this power in single-mode operation as in reference [132]. In the experiments discussed here, no attention was paid to the beam quality of the output because the priority in the performed tests was the achievable output power.

General Notes on the Operation of Ho:YAG Thin-Disks

The thin-disk was monitored during laser operation with a CCD camera, as it is common for ytterbium oscillators. The corresponding video provides information about the alignment because less fluorescence is emitted in regions where laser light is emitted. The camera is also used to estimate the diameter of the pump spot. This method delivers only an estimation because the spot's perceived size grows with the applied pump power. The spot size was found to change by roughly 20 % for an increase in pump power by 80 W. The growth in diameter could be due to the growth in power in the outer parts of the pump beam or maybe due to some thermal effects in the pump beam path. The diameters specified in this chapter were, therefore, all determined with a pump power of about 14 W. The camera can also indicate mode-locked operation because red third-harmonic light is generated in the Kerr-medium and is clearly visible on the thin-disk. The color of the light was inferred from beams escaping the cavity.

Patterns on the thin-disks were noticed with the CCD camera. An example of such a pattern can be seen in fig. 4.3a. The pattern reacted to the touching of the pump transfer fiber and is probably a consequence of the beam profile emitted by the multimode fiber. This pump inhomogeneity should be disadvantageous for efficient single-mode operation. The single-mode result from conference contribution [132] might have benefited from the more homogeneous flat-top pump profile, which was mentioned in the talk of this contribution [132].

The pumped area is also visible to the eye because it emits a pale red glow. This visible light consists mainly of light around 650 nm with a strong emission line at 667 nm. It also contains an at least ten times weaker emission at about 550 nm. These emissions can be explained with the energy level diagram of Ho:YAG in fig. 4.3b. The wavelengths match the transition from $^5F_5$ to the ground state of holmium $^5I_8$ (667 nm) and the transition from $^5S_2$ ($^5F_4$) to $^5I_8$ (549 nm) [136]. How these highly excited states become populated from laser operation in the $^5I_7$ and $^5I_8$ state and upconversion dynamics into the $^5I_5$ and $^5I_6$ level needs further investigation. Two more emission features were found at 920 nm and 888 nm, see fig. 4.3c. These emission features would energetically match the transition from $^5I_5$ to $^5I_8$. This transition could provide insights into the magnitude of upconversion in future studies because $^5I_5$ is the upper state of this process.

The rise in temperature of each thin-disk was initially checked for safety reasons with a thermographic camera (A325, FLIR Systems). It was confirmed that the temperature of the thin-disk is higher without stimulated emission. Therefore, high average power systems might demand a safety circuit to interrupt pumping if lasing is interrupted. For the non-lasing thin-disks with equal doping but varying thickness, it was found that the heating

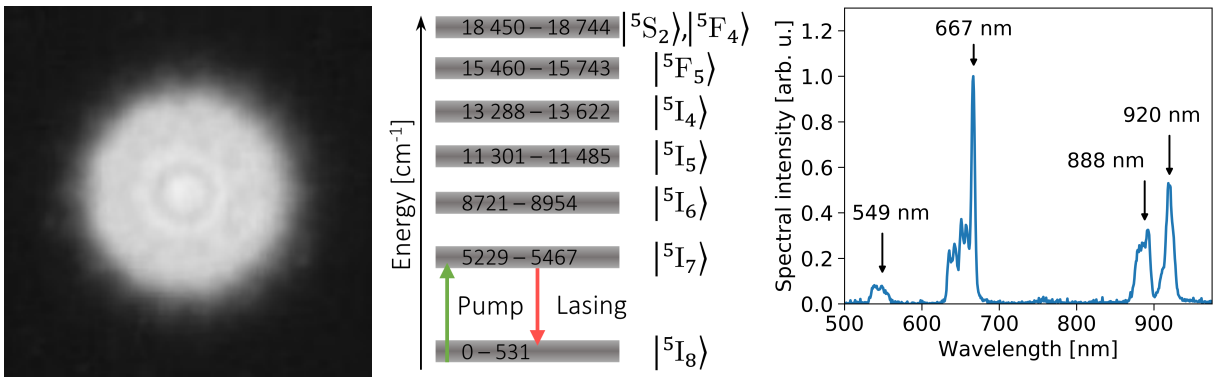

a) b) c)

Figure 4.3: a) Pump spot on a Ho:YAG thin-disk with brightness pattern. b) Energy levels of Ho:YAG. The wavenumber values are taken from reference [137] and indicate the width of the levels. The depicted energy levels consist in reality of many discrete sub-levels. This illustration is not to scale. c) A part of the visible to near-infrared fluorescence spectrum of a pumped Ho:YAG thin-disk with a doping concentration of 2.5 %.

up roughly scales with the increase in thickness. A doubling of the thickness led to an about 2.1 times larger temperature increase. The tripling of the thickness led to an about 3.2 times larger temperature difference. This nearly proportional dependence agrees quite well with the first-order approximation described in eq. (2.68).

4.4.2 Mode-Locking Experiments

One goal of this thesis was to duplicate the Kerr-lens mode-locked femtosecond oscillator form reference [133] in a well-engineered, vacuum compatible way. A corresponding amount of effort was therefore invested into the technical realization of this oscillator. The pictures in fig. 4.4 try to give an impression of this effort to realize a sturdy, vacuum-compatible oscillator.

The oscillator in reference [133] had the disk blank attached to a flat diamond substrate. The last available identical disk blank with a doping concentration of 2.5 % and a thickness of 200 µm was, however, erroneously mounted on a curved diamond substrate, which caused the thin-disk to have a ROC of 2 m instead of the nearly flat 20 m.

This difference in refractive power greatly influenced the laser cavity, especially since two reflections were made on the thin-disk. This can be seen in fig. 4.5a, where the stability parameter of the cavity with and without strong disk curvature is plotted over the length of the Kerr-telescope. The presence of the strong curvature shifts one stability zone to nearly zero length and makes this zone practically inaccessible.

The consequences become even more apparent if one compares the laser beams which form within the respective cavity. This comparison is made at the relevant second inner stability limit for the cavity design of reference [133]. The comparison can be seen in

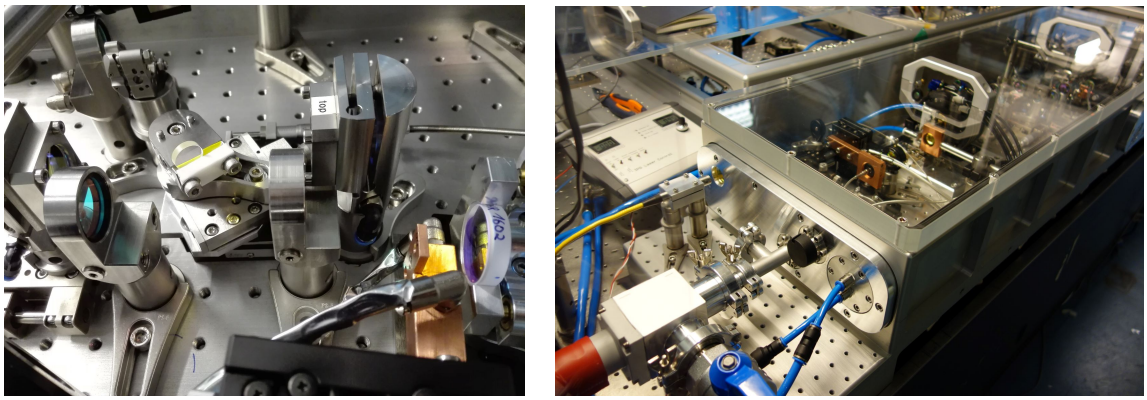

a) b)

Figure 4.4: a) Picture of some oscillator components. All components were implemented in the most rugged way available. To the left of the center, one can see the Kerr-medium, to the left and right of the medium the two concave mirrors in adjustable mounts, in the foreground two dispersive mirrors in rigid mounts and in the lower right corner the hard aperture and the end mirror. b) The sealed, vacuum compatible oscillator chamber.

fig. 4.5b. The plot shows that the parts to the left and right of the focusing section exchange their beam-radius evolution. This change in beam-radius evolution introduces a great deal of uncertainty in the realization of mode-locked operation because it is not clear how this new beam-radius evolution will respond to the Kerr-lens of mode-locked operation. It is, however, the change in beam radius when mode-locked that generates the self-amplitude modulation in Kerr-lens mode-locking, as was discussed on page 19. Therefore, this altered beam-radius evolution can have far-reaching consequences for the suitability of the cavity for Kerr-lens mode-locking.

The initially planned replication of the oscillator from reference [133] was, therefore, no longer possible, because only the curved thin-disk was available at that time due to a shortage in identical disk blanks and the long lead-time of the manufacturing process. That is why the question from subsection 4.3.1 arose if it is possible to mode-lock a cavity similar to reference [133] if it contains a curved thin-disk. The cavity from reference [133] was used as a starting point, because no better-suited cavity design was known for a curved thin-disk and a development from scratch was regarded as riskier and more time-consuming. As a first adaptation to the changed circumstances, the hard aperture was moved to the now collimated arm. The development then started with the best possible guess for the remaining degrees of freedom.

A favorable finding was that mode-locked operation was possible for the cavity with the curved thin-disk. Mode-locked operation depended, however, on a particular horizontal detuning of the end mirror. An observable consequence of this detuning was that the two depletion spots, which arose from the two reflections on the thin-disk, moved apart and approached the edges of the pump spot. Therefore, it is believed that an additional soft aperture at the edges of the pump spot gave rise to mode-locked operation with horizontal

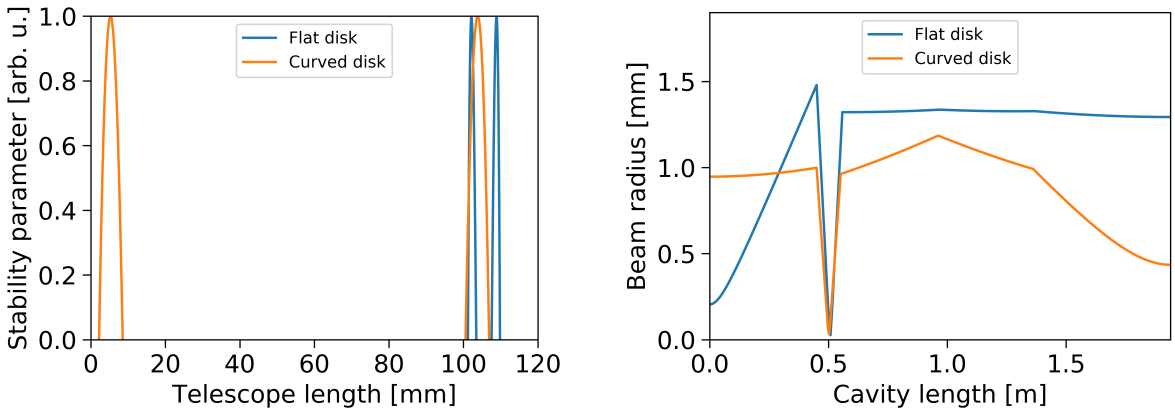

a) b)

Figure 4.5: a) The stability parameter of the cavity plotted over the length of the Kerr-telescope for the nearly flat and the concave disk. b) Simulated beam-radius evolution within the laser cavity for the nearly flat and the concave disk. Both cavities operate at the shorter limit of the second stability zone with respect to the Kerr-telescope length [in fig a) the orange curve at 101 mm and the blue curve at 108 mm]. However, their laser-beam evolution is of opposite character with opposite beam diameters at the end mirrors.

detuning. The experience that horizontal detuning can facilitate mode-locked operation was already made before [90]. Some detuning was also required in the oscillator of reference [133], as was learned in verbal communication with the author of reference [133].

A schematic of the oscillator can be found in fig. 4.6. The distance from the output coupler to the thin-disk was about 65 cm. For guiding the beam to the second reflection, another 39 cm were needed. The beam traveled then 41 cm to the focusing section of the Kerr-medium, for which a length of about 10.6 cm was measured, before another 42 cm led the beam to the hard aperture and end mirror. The pump spot on the thin-disk had a diameter of about 2.7 mm.

It was possible to improve the mode-locked performance with known measures like increasing the output coupling rate, reducing the nonlinear action in the Kerr-medium by lowering its thickness, and reducing the amount of negative dispersion. Also, the second reflection on the thin-disk supported the achieved performance, as reported in reference [133]. With only one reflection on the curved disk, mode-locked operation was only possible for an output coupling of 1 % and was, thus, limited to an output power of about 5 W.

The best performance obtained had an output power of 15.5 W in pure mode-locked operation with a spectral bandwidth of 14 nm. This performance was obtained with an output coupling rate of 3 % and dispersive mirrors (HD1501) with a round-trip GDD of $-14\,000\,\mathrm{fs}^2$. The Kerr-medium in use was a 1 mm thick sapphire plate. A horizontal detuning was necessary to initiate this mode-locked operation. The optical-to-optical efficiency was 20 %.

It was challenging to achieve this performance because the mode-lockable range of

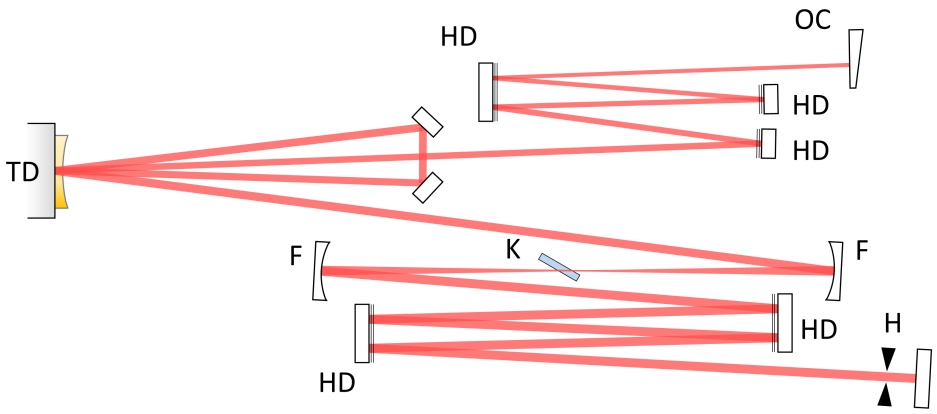

Figure 4.6: Schematic drawing of the Ho:YAG thin-disk oscillator. The abbreviations are: OC, output coupler; HD, high-dispersion mirror; TD, thin-disk; F, concave mirror of the Kerr-telescope; K, Kerr-medium; H, hard aperture. The non-labeled mirrors are highly reflective mirrors.

the alignment and of other parameters decreased as the performance increased. These small ranges caused difficulties in finding mode-locked operation. In addition, damage to the Kerr-medium occurred frequently. These issues prevented a further optimization of mode-locked operation. They even forced a gradual reversal of the performance-enhancing measures in order to regain a reliable configuration.

As said, the strong dependence on the horizontal detuning was one reason for the repeatability issue. If this detuning was needed due to insufficient self-amplitude modulation, then the cavity design was inappropriate for the presence of a curved thin-disk, because modifications of the hard aperture in size and position could not replace the need for horizontal detuning. In other words, maybe the intensity-dependence of the beam caustic in the resulting oscillator was not really suitable for mode-locked operation (recall the discussion of fig. 4.5b on page 63). Perhaps a cavity development from scratch could have overcome the problems with mode-lock initialization, but it was considered as a too big leap into the unknown.

Another contribution to the repeatability issue could be the inhomogeneity of the pump spot. The illumination pattern affects the output power, which is especially noticeable while touching the fiber. This change in power could result from a change in the gain profile or a change in the thermal lens. Both effects can potentially influence the mode-locking behavior.

The configuration, which was finally found to be reliable, used a 2 mm thick sapphire plate, an output coupling rate of 1.8 % and dispersive mirrors with a round-trip GDD of $-16\,000\,\mathrm{fs}^2$. In this configuration, the oscillator emitted an output power of 7.2 W with an optical-to-optical efficiency of 10.7 %. This emission was relatively stable, as shown in the long-term power recording in fig. 4.7a. It is interesting to mention that a decrease in output power accompanied the initiation of mode-locked operation. This behavior is another

indication of the peculiar character of this detuning-dependent oscillator configuration.

The emitted spectrum was analyzed with a rotating grating spectrometer (waveScan 800-2600 nm, APE GmbH) and is displayed in fig. 4.7b. The spectral width of 15.3 nm corresponds to a bandwidth-limited pulse duration of 300 fs.

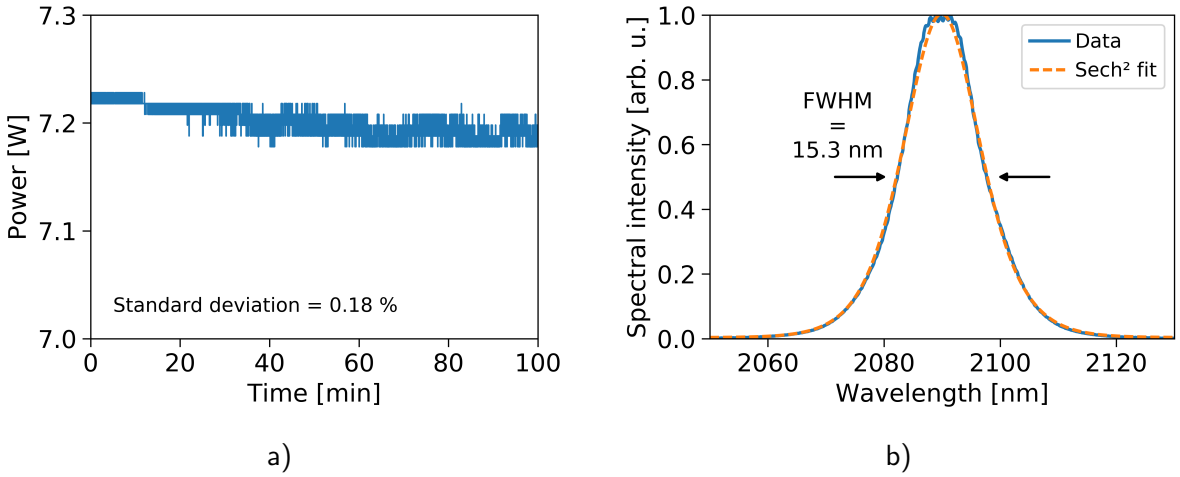

Figure 4.7: a) Long-term power recording of the reliable oscillator configuration in mode-locked operation. b) Spectral bandwidth of the mode-locked laser beam.

The repetition rate of the oscillator was 76.4 MHz. The pulse train was electronically analyzed to get an impression of its stability. For this purpose, the pulse train was recorded with a photodiode and analyzed in the proximity of the repetition rate with an RF spectrum analyzer (E4447A, Agilent). The result is shown in fig. 4.8a. This graph was recorded with a resolution bandwidth of 30 Hz and threefold averaging. The graph shows a suppression of the oscillator noise by 80 dB against the repetition rate signal. This suppression indicates as stable mode-locked operation as in reference [133].

A typical beam profile, emitted by the oscillator in mode-locked operation, can be seen in fig. 4.8b. The beam profile shows unusual deviations that go beyond those of an elliptical beam profile. These additional distortions might be caused by the horizontal cavity detuning and the corresponding clipping of the laser beam on the pump spot.

At some later point, it was also attempted to realize mode-locked operation with the at-that-point-available flat 100 µm thin-disk with a doping concentration of 2.5 %. The flatness of this thin-disk should have restored the intracavity beam caustic from reference [133]. However, it was not possible to find mode-locked operation for this thin-disk, even with a closed cavity. This was surprising and is another example of the difficulty of finding a mode-lockable configuration for this gain material.

The mode-lockable oscillator based on the 200 µm thin-disk was then used to study the influence of the atmosphere on the oscillator performance. These experiments will be reported in the next subsection 4.4.3.

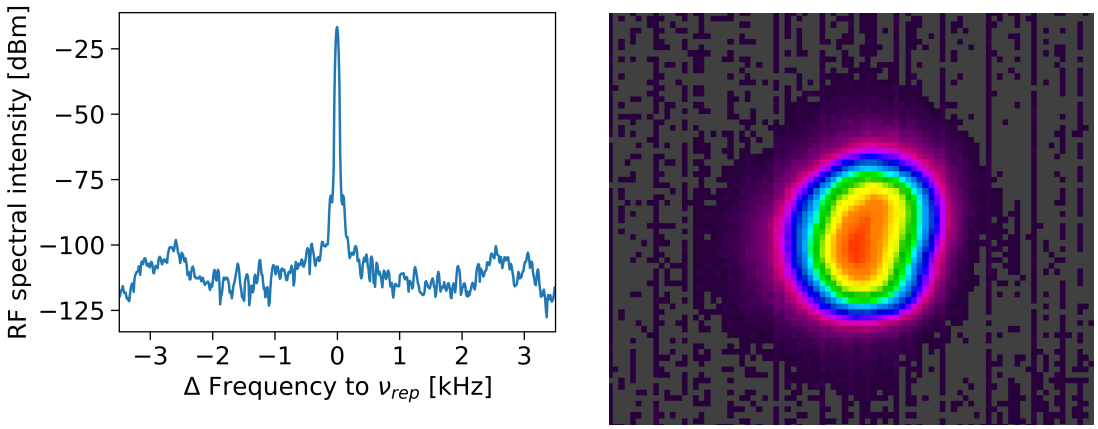

a) b)

Figure 4.8: a) Intensity noise at frequencies around the oscillator's repetition rate. The resolution bandwidth was 30 Hz. b) A typical intensity beam profile emitted by the oscillator in mode-locked operation.

4.4.3 Mode-Locked Operation under Modified Atmosphere

One direction of the Ho:YAG development was to investigate the behavior of the oscillator under modified atmospheres. This investigation promised improved efficiency, increased stability, and scaling of peak power. For this investigation, it was necessary to make the housing of the oscillator gastight. The result of this effort was shown in fig. 4.4b. It was possible to evacuate the oscillator housing with a scroll pump down to 1 mbar. This partial vacuum was retained quite well, rising by only 14 mbar over 16 hours. This tightness of the housing also allowed a dehumidification of the chamber volume with silica gel or dry nitrogen gas.

The operation of the mode-lockable oscillator was first investigated in CW to reduce complexity. The influence of humidity on CW operation was investigated by dehumidifying the chamber with silica gel. In this experiment, the humidity was reduced from a relative humidity of 40 % to 13 %, which resulted in about 21 % more output power at all pump power levels, see fig. 4.9a. The two possible influencing factors of dehumidification on CW operation are thermal lensing and absorption. The similar improvement at all pump powers is an argument against a dominant role of thermal lensing, because the strength of thermal lensing scales with the applied pump power [138]. Accordingly, thermal lensing as the cause of the improvement would have a negligible positive impact at low pump powers, which then should increase with pump power. As this behavior is not reflected in the data, it is probably the reduction in absorption that led to the observed increase in power due to dehumidification.

Next, the evacuation of the cavity was investigated. In this investigation, the oscillator was still in the mode-lockable configuration, which is not the most efficient configuration for CW operation. The evacuation of the cavity also resulted in an increased CW performance.

However, in this case, it is very likely that thermal lensing improved the CW performance by modifying the oscillator's location within the stability zone. This hypothesis is plausible, because the emitted power always depends on the location within the stability zone and the thermal lens of the gas in front of the thin-disk depends on the air pressure [138]. The observed dependence of the emitted CW power on the air pressure is shown in fig. 4.9b. The performance maximum at about 250 mbar is compatible with the hypothesis of modified thermal lensing as the cause, because it is conceivable that the best matching thermal lens in terms of output power is obtained at this air pressure. Moreover, a reduction in absorption alone cannot explain the observed power evolution because absorption alone would lead to a power maximum at 0 mbar. Furthermore, the power improvement by evacuation is greater than the corresponding effect by dehumidification. A pressure reduction from 930 mbar to 300 mbar corresponds to the previously described humidity reduction from 40 % to 13%, but the pressure reduction gave a power improvement of 48 % instead of the 21 % by dehumidification. Therefore, a modification of the thermal lens was almost certainly involved in the observed pressure dependence of CW operation.

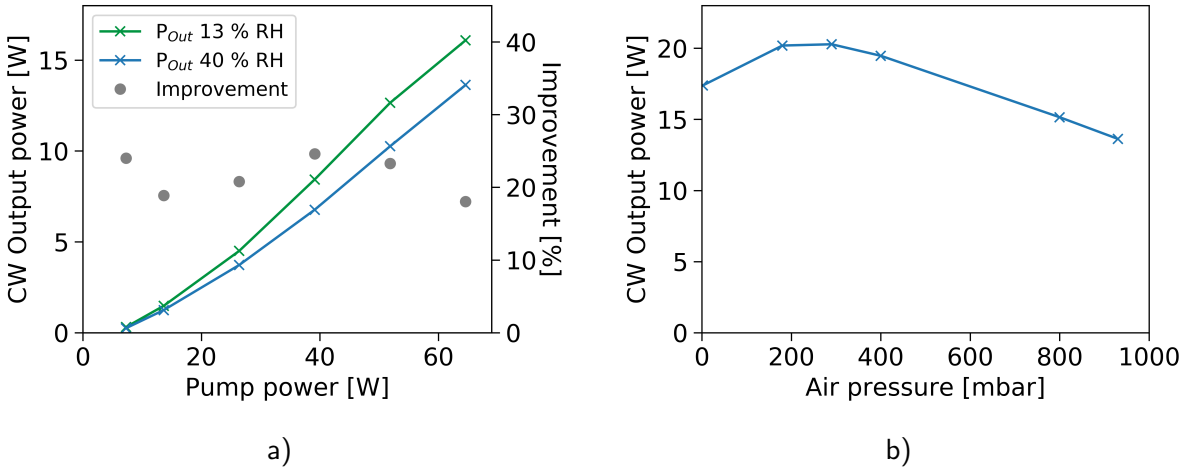

Figure 4.9: a) CW output power over pump power for the cavity being surrounded by air with a relative humidity of 13 % and 40 %. Also, the improvement is displayed at each pump power. b) CW output power as a function of the air pressure in the cavity. The pump power was fixed to 65 W.

For mode-locked operation, changes in dispersion and self-phase modulation are additional influential effects of atmospheric modifications.

The goal of the investigation of mode-locked operation under modified atmosphere was to check for an improvement potential and to exclude the presence of a peak power restriction. For this, mode-locked operation under ambient conditions was compared to mode-locked operation under modified atmosphere. In these experiments, the mode-locked oscillator delivered an output power of about 9.3 W with an output coupling rate of 3 % under ambient conditions. An abstract of the observed improvements of this performance is given in table 4.5. The values in this table are mean values. The power improvements

fluctuated typically by ±2 percentage points and the bandwidth improvements by ±1 percentage point.

Table 4.5: Performance change of mode-locked operation under modified atmosphere.

	Δ Power [%]	Δ Bandwidth [%]
Dried air < 13 % RH	+18	+ 4
Nitrogen < 10 % RH	+21	+ 7
Air 800 mbar	+10	+ 6
Air 660 mbar	+20	+12

For the first two entries in table 4.5, the improvement is probably due to the removal of water vapor from the cavity, because the power improvement agrees well with the improvement due to dehumidification in CW operation. The reduction of water absorption is, therefore, a reliable approach to achieve about 20 % more power. The thermal lens, the dispersion and the self-phase modulation do not seem to be strongly dependent on the water vapor content.

The evacuation of the chamber, in contrast, involves all four effects. The observation for evacuation was that the output power and bandwidth increased as the air pressure was decreased. This trend continued up to the point, at just below 660 mbar, where mode-locked operation was lost. A direct performance comparison between ambient pressure and lower pressures was, therefore, not possible with this oscillator configuration. The achieved improvement in output power by 21 % and in bandwidth by 12 % boosted the obtained peak power correspondingly. However, this growth in peak power was not as pronounced as had been hoped for. Brons [98], for example, observed a much stronger pressure dependence for Yb:YAG KLM oscillators. The different dependence suggests that the presence of air is not yet the limiting factor for the peak power in Ho:YAG oscillators. Therefore, a promising next step for peak-power scaling in the near future is to test longer Kerr-telescopes with larger waist sizes in the Kerr-medium [101]. Prior to this step, the availability of sufficient output power in single-mode operation should be ensured to be able to exploit the potential of the longer Kerr-telescopes.

4.4.4 Mode-Locking with Positive Dispersion

Subsection 3.4.1 introduced mode-locked operation in the positive dispersion regime as a peak-power scaling approach. As the last experiment for the Ho:YAG oscillator, it was investigated how easy one can obtain this mode-locked operation in the 2 µm range. For this, positively chirped mirrors were inserted into the cavity. It was indeed possible to initiate mode-locked operation in this regime, but only two times. Attempts were made to improve the repeatability and stability of this mode-locking regime, but variations of the dispersion, the Kerr-medium, the applied pump power, the position in the stability zone,

the Kerr-medium position, and the alignment did not lead to an improved behavior. The situation was aggravated by the fact that the Kerr-medium was frequently damaged, as well as occasionally some of the dispersive mirrors.

The configuration, for which mode-locked operation was spotted, used a 3 mm thick YAG substrate as Kerr-medium and operated without output coupling. The cavity contained positive dispersive mirrors with a round-trip GDD of 7000 fs^2. Some leakage from the cavity was used for the recording of the spectrum in fig. 4.10. The recorded spectrum shows the characteristic rectangular shape for the positive regime [109] and had a width of about 25 nm. The spectrum is of low quality due to the limited resolution of the spectrometer (NIR Quest, Ocean Insight), the low signal level and the missing opportunity to improve it.

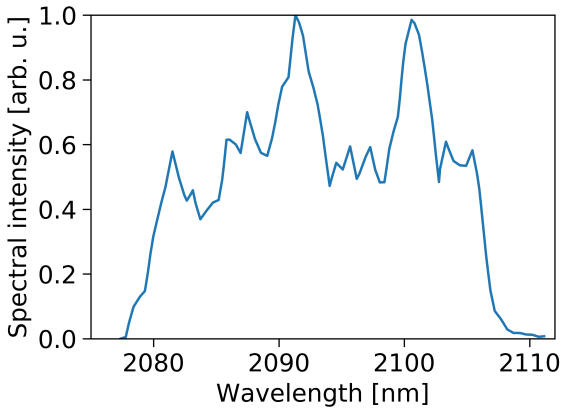

Figure 4.10: Spectrum obtained for mode-locked operation in the positive dispersion regime.

In conclusion, it was found that mode-locked operation in the positive regime is harder to obtain than in the negative regime, just as it is the case at a wavelength of 1 µm [93]. With this last result, the development of the Ho:YAG thin-disk oscillator was stopped. The gained insights are summarized in the next section 4.5.

4.5 Chapter Summary and Outlook

In this chapter, the range for the ideal doping concentration of Ho:YAG thin-disks was narrowed down based on tests of different thin-disks. As a result, the ideal doping concentration should be located in the range from 2 % to 3 %. A disk thickness of 200 µm was found to be a good tradeoff between absorption and gain on the one hand and thermal properties on the other hand.

This chapter also reported on the realization of a Kerr-lens mode-locked Ho:YAG thin-disk oscillator. This oscillator delivered an output power of 15.5 W and a bandwidth of 14 nm at its best performance. In its reliable configuration, the oscillator emitted an output power of 7 W with a pulse repetition rate of 76 MHz and a bandwidth of 15 nm. It was

found that operation in dry nitrogen gas benefits mode-locked operation with 21 % more average power and 7 % more bandwidth.

The best obtained mode-locked performance in ambient air fell short by about one-third in power when compared to reference [133]. This falling short of expectations and the repeatability issues with the initiation of mode-locked operation point to the need for a dedicated cavity design for curved thin-disks.

Mode-locked operation in the positive dispersion regime was found to be possible, but it was harder to obtain than conventional mode-locked operation in the negative dispersion regime.

In the following, further ways to improve femtosecond Ho:YAG thin-disk oscillators are provided because the development of such oscillators is still an active field of research, as indicated by recent results of others [132, 139].

The realization of higher output coupling rates is a promising development direction for Ho:YAG thin-disk oscillators. Those higher rates would allow to access a larger share of the intracavity peak power and they would reduce the impact of parasitic losses on efficiency. Such higher output coupling rates could be realized with the additional gain provided by an active multipass cell, as was demonstrated in chapter 3. The implementation of such an active multipass cell holds, therefore, promise for significant improvements and should be pursued in future experiments. Experiments with an active multipass cell were planned in the frame of this thesis but not realized.

In future oscillators, one should use pump-transfer fibers longer than 2 m to obtain a more homogeneous pump profile. In addition, the core diameter of the pump transfer fibers should be larger than the current 550 µm to support even more transverse modes, because in Yb:YAG oscillators core diameters of 800 µm are used for wavelengths of half the length. More pump power would be useful too, because the thin-disks do not saturate at the current pump powers, recall for example fig. 4.2b. Therefore, one should consider investing in more powerful multimode pump sources in the future. The avoidance of parasitic cavity losses is an important topic. Thus, one could try to mount the Kerr-medium on a rotation stage for proper tuning to its Brewster's angle. A direction to explore for peak-power scaling is the use of larger ROC values for the Kerr-telescope and the resulting larger beam diameters in the Kerr-medium [101].

High inversion-densities are needed in the thin-disk geometry to obtain reasonable amplification over the short disk thickness. The correspondingly high population densities in the upper laser level are problematic due to the upconversion process and its increasing occurrence with shrinking distance between excited ions. It could, therefore, be rewarding to discuss the matter of holmium cluster formation with material suppliers. Measures to ensure equal separations between the holmium ions would reduce upconversion to a minimum in future disk batches.

The improvement ideas mentioned above should allow for plenty of future improvement. And although Ho:YAG thin-disk oscillators are still at an early stage of development, they have already demonstrated remarkable performance in the generation of mid-infrared radiation via intra-pulse difference-frequency generation.

At the driving wavelength of about 2.1 µm, 7 W of fiber-compressed Ho:YAG power

were used by colleagues for the generation of mid-IR light. The 2.1 µm pulses had a duration of 15 fs and a peak power of 2 MW. This was sufficient performance to achieve 24 mW of mid-IR in the range from 5 µm to 20 µm [71]. Compared to the result obtained by other colleagues using a 1 µm driving source, where 60 W of 16 fs long pulses with a peak power of 60 MW generated 50 mW of mid-IR light in the range between 6.5 µm to 11 µm [20, 27, 88], the performance of Ho:YAG driven IDFG demonstrates the very efficient conversion of 2 µm radiation into the mid-IR if one considers the many times lower peak and average power used in this case. Other 2 µm systems reported similarly favorable performance [28, 69, 70]. Therefore, the change from 1 µm to longer 2 µm driving radiation holds the promises made in section 4.1.

However, up to now, Ho:YAG thin-disk oscillators are quite delicate to handle. For example, it was not trivial to initiate mode-locked operation even in the oscillator of references [133] and [71], as was learned in verbal communication with the author of these publications. Furthermore, the less alignment-sensitive pulse compression in Herriott cells still needs to be developed for the order-of-magnitude lower peak-power level emitted by Ho:YAG thin-disk oscillators. In addition, the Ho:YAG thin-disk technology is as expensive as the Yb:YAG thin-disk technology but not yet as reliable and developed as the Yb:YAG thin-disk technology. Therefore, Ho:YAG is not yet an advancement over Yb:YAG for generating the desired broadband mid-IR.

Fortunately, bulk-laser technology based on chromium-doped zinc sulfide made quite some progress in our research group at that time, such that it became a promising alternative to Ho:YAG as 2 µm driving source. Chromium-doped zinc sulfide and chromium-doped zinc selenide, and my contributions to their laser development will be introduced in the coming chapter.

Chapter 5

Cr:ZnS Amplifiers

5.1 Motivation for Developing Cr:ZnS/Cr:ZnSe-based Bulk-Laser Technology

The application strategy for the thin-disk oscillators described in chapter 3 and 4 was to start with their high average power and rather long pulses and to perform some post-compression for them. Either in a Herriott cell, as it was done by colleagues for ytterbium-based driving lasers [88, 89], or in a nonlinear optical fiber, as it was done by colleagues for a holmium-based driving laser [71]. In this way, some average power is lost, but the necessary short pulse duration for broadband IDFG and electro-optic sampling is obtained.

For lasers based on chromium-doped zinc sulfide (Cr:ZnS) and chromium-doped zinc selenide (Cr:ZnSe), the sequence of actions is reversed. One starts with short pulses straight from the oscillator and enhances their power in an amplifier. In this way, one can obtain, with a simple single-pass amplifier, pulses with a pulse duration of down to 26 fs [36] and an average power of up to 7.4 W [46] in the 2 µm range. Since the average powers involved in this approach are much lower, the whole arrangement is less dangerous to handle and is exposed to weaker thermally induced perturbations. An overview of systems realized in this way will be provided in section 5.3.

Systems of this type have already demonstrated great performances in the generation of mid-IR radiation via IDFG. They can generate in GaSe mid-IR powers of about 20 mW already with about 4 W of output power and 80 MHz repetition rate [140, 141]. The mid-IR power, in this case, is contained in a spectrum spanning from 6.7 µm to 17 µm. They can reach even 250 mW levels by launching only 3 W of their radiation into a ZGP crystal [140, 142]. The generated mid-IR then has a bandwidth of 6.7 µm to 12 µm.

In both conversion examples [140, 141], the chromium-based driving laser took advantage of the favorable IDFG properties of 2 µm sources introduced in section 4.1. Likewise, the electro-optic sampling should benefit from the wavelength of chromium-based lasers.

In addition, a cascading of difference-frequency processes was reported for chromium-based implementations. Those cascaded parametric processes allow the generation of a broader mid-IR spectrum than the pulse duration of the driving pulse actually supports

and some parts of the additional spectrum should be CEP-stable like the initial DFG band [140, 143].

It is expected that a chromium-based system with an average output power of 7 to 10 watts can cover the power requirements of an Infrasampler system for mid-IR generation and electro-optic sampling. With the development of diode-pumped Kerr-lens mode-locked Cr:ZnS and Cr:ZnSe oscillators in our group [144, 145], cost-effective, low-noise front-ends were available. It then needed the development and optimization of potent power amplifiers to make the great potential of the Cr:ZnS/Cr:ZnSe bulk-laser technology accessible for the Infrasampler application. This chapter reports on this amplifier development and the next section 5.2 introduces the gain media in more detail.

5.2 Properties of Cr:ZnS and Cr:ZnSe as Laser Gain Medium

Chromium-doped zinc sulfide and chromium-doped zinc selenide are rather new as laser gain media. The first demonstration of laser operation took place in 1996 [146]. The development of an effective fabrication technology in the years afterward facilitates their usage nowadays [36] and enables the current rapid development of the corresponding laser technology. Their favorable properties were recognized early on [146]. Among those properties are their ability for room-temperature lasing and their very broad absorption and emission bands, which are shown in fig. 5.1.

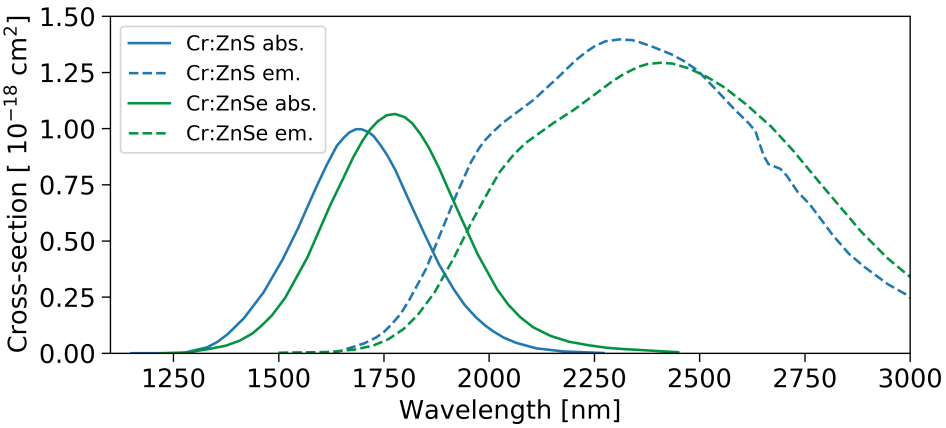

Figure 5.1: Emission and absorption cross-sections of Cr:ZnS and Cr:ZnSe. The displayed data was digitally extracted from reference [46].

Both materials offer a broad emission bandwidth. For Cr:ZnS, this bandwidth already allowed the generation of sub-35 fs pulses by oscillators [36, 145]. Such pulse durations at a wavelength of 2.3 µm correspond already to pulses with about four optical cycles. Therefore, those gain media are sometimes called "Ti:sapphire of the mid-IR".

The displayed absorption bands determine the selection of potential pump sources. Those pump sources are diode lasers, erbium fiber lasers, thulium fiber lasers and more exotic lasers like Co:MgF_2 lasers [35] or others [46].

Relevant diode lasers are available, for example, from SemiNex Corporation in the range between 1532 nm and 1650 nm. Currently, mainly multimode single-emitter laser diodes are used in diode-pumped applications due to their higher radiance. Such single-emitter laser diodes are based on indium phosphide and provide an average power of 3 W to 4 W. Up to now, it was not possible to benefit from the higher average powers but lower radiance offered by larger diode laser modules [147]. Single-emitter laser diodes are currently the most suitable diode lasers.

Erbium fiber lasers are available in the conventional-wavelength band (about 1530 nm to 1565 nm; C-band) and long-wavelength band (about 1565 nm to 1625 nm, L-band). Of these, a laser at the very edge of the C-band at 1567 nm [36] is usually used as a tradeoff between the available power of the fiber laser and the absorption coefficient of the chromium-doped gain crystal. The choice of a fiber laser simultaneously provides access to higher pump powers and better beam quality than is available with diode lasers.

The second, relevant, readily available fiber-laser technology is thulium fiber lasers. Those usually operate at a wavelength of about 1950 nm. Pumping with a thulium fiber laser has the advantage of a much smaller quantum defect in comparison to an erbium fiber laser. In erbium-laser-pumped amplifiers, at least 31 % of the absorbed pump power are not usable for the laser emission as calculated with eq. (2.12). By switching to a thulium-based pump source, this value is reduced to only about 16 %. This means that all heat-related issues are alleviated by a factor of two by switching to thulium. Or in other words, twice as much power can be absorbed for thulium-pumping before potential limitations are encountered.

This advantage matches well with the good power scalability of thulium fiber lasers. Average powers of more than 1 kW have already been demonstrated for such single-mode fiber laser systems [148]. This performance is already competitive with the very well developed ytterbium fiber technology [148]. In comparison, the highest reported powers for erbium are 302 W from a single-mode fiber [149] and 656 W for a multimode fiber [150].

Furthermore, two powerful thulium lasers were already available in the lab for experiments. Therefore, thulium fiber lasers were selected as the pump source for the development of powerful amplifiers.

As one can see in fig. 5.1, the regions of absorption and emission overlap for the wavelengths of thulium pump lasers. As discussed in the context of eq. (2.16) and eq. (2.17), this overlap affects the pump light absorption and the inversion formed. This effect makes the choice among the possible thulium wavelengths very important, as will be seen in subsection 5.4.3.

The figure above also shows the spectroscopic similarity of Cr:ZnSe and Cr:ZnS. The spectral shift present in these properties makes Cr:ZnSe more suitable for pumping with thulium fiber lasers. However, Cr:ZnS has the better material properties for high power operation [151]. It has, for example, a lower temperature derivative of the refractive index, which is important for reducing thermal lensing, and it has a higher thermal conductivity,

which is important for efficient heat removal. Cr:ZnS is therefore of greater interest for the development of powerful amplifiers. The numerical values of the discussed properties are compared in table 5.1 for both gain media. In addition, the corresponding values of titanium-doped sapphire are provided for reference.

Table 5.1: Relevant properties of Cr:ZnS, Cr:ZnSe and Ti:sapphire. Listed are the thermal conductivity k, the change of refractive index by temperature $\mathrm{d}n/\mathrm{d}T$ and the nonlinear refractive index n_2. The values are taken from reference [36].

	Cr:ZnS	Cr:ZnSe	Ti:sapphire
k [$\mathrm{W\,K^{-1}\,m^{-1}}$]	27	18	35
$\mathrm{d}n/\mathrm{d}T$ [$\mathrm{K^{-1}}$]	$54{*}10^{-6}$	$61{*}10^{-6}$	$12{*}10^{-6}$
n_2 [$\mathrm{cm^2\,W^{-1}}$]	$\approx 10^{-14}$	$\approx 10^{-14}$	$3{*}10^{-16}$

It is worthwhile to point out the high nonlinear refractive indices of Cr:ZnS and Cr:ZnSe. They allow to drive substantial nonlinear spectral broadening based on SPM in the amplifier crystal and can thereby counteract and even overcompensate gain narrowing. An example of this ability will be seen in subsection 5.4.6. On the other hand, a high nonlinear refractive index also causes self-focusing with possible consequences ranging from mode-mismatch in the amplifier, to beam quality degradation and the potential risk of catastrophic beam collapse.

Another relevant property of Cr:ZnS is the temperature dependence of the upper-state lifetime. This dependence is depicted in fig. 5.2. The graph shows that the lifetime is greatly reduced for temperatures above 300 K ($\approx 27\,^{\circ}\mathrm{C}$). This shortening is disadvantageous and indicates a potential benefit of a low-temperature operation.

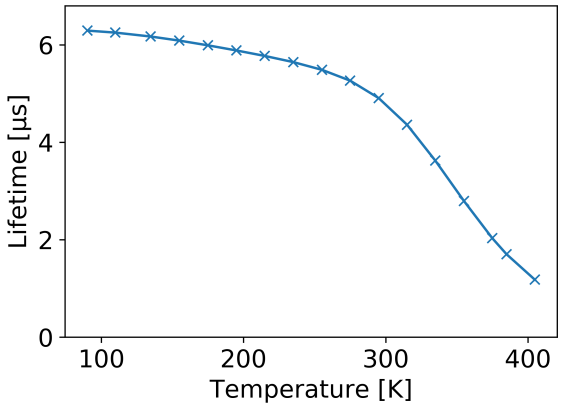

Figure 5.2: Temperature dependence of the upper-state lifetime in Cr:ZnS. Data digitally extracted from reference [151].

The supply of the very promising Cr:ZnS crystals is very limited. The polycrystalline Cr:ZnS crystals used in this thesis were purchased from IPG Photonics. The next section

will show that a lot of development and improvement took place for amplifiers based on polycrystalline Cr:ZnS over the last few years.

5.3 State of the Art of Cr:ZnS/Cr:ZnSe-based Amplifiers

The amplifiers reported in the literature can be divided into the class of amplifiers with pulsed pump and the class with continuous pump.

The amplifiers with pulsed pump are used for the amplification of ultrashort pulses [152] or narrowband pulses [153]. They are based on Cr:ZnSe and can achieve amplifications of several orders of magnitude [154]. Their repetition rate goes up to 1 kHz.

The aim of this thesis is, as mentioned in chapter 1, to amplify the entire pulse train with its pulse repetition rate of tens of megahertz. Thus, only continuously pumped amplifiers are of interest for this application. The majority of the continuously pumped amplifiers are based on Cr:ZnS. A selection of such systems is given in table 5.2.

Table 5.2: Overview of chromium-based femtosecond amplifiers. The erbium-based pump lasers had a wavelength of 1567 nm and the thulium-based pump lasers had a wavelength of 1908 nm.

Pump	P_{Seed} [W]	Crystal	P_{Out} [W]	Gain factor	Year [Ref.]
21 W erbium	1.6	9 mm Cr:ZnS	7.4	4.6	2017 [46]
20 W erbium	1.1	9 mm Cr:ZnS	6.4	5.8	2018 [36]
17 W erbium	1.1	9 mm Cr:ZnS	4.1	3.73	2019 [155]
14 W thulium	1	6 + 9 mm Cr:ZnS	3.35	3.35	2019 [143]
105 W thulium	1.2	spinning ring 12 mm Cr:ZnSe	27.5	22.9	2018 [156]

The field of Cr:ZnS-amplifiers saw rapid development over the last years. Back in 2014, the output power level was still on the 0.25 W level [157]. In the meantime, a range of much higher performances has been demonstrated. The dominating amplifier design is the single-pass configuration in one amplifier stage. The development mainly focused on amplifiers pumped by erbium fiber lasers, making single-pass amplifiers with erbium pump lasers the most developed technology. From such amplifiers, an output power of about 6 W can be obtained, which is achieved with a gain factor of about 6. The publications indicate that the optimization goal for erbium-laser-pumped, single-stage, single-pass amplifiers has shifted a bit more towards spectral coverage instead of power, as recent publications report on lower output powers. The targeted spectral coverage is important for DFG and frequency comb applications.

Many of the essential parameters defining such erbium-laser-pumped, single-pass amplifiers, such as the pump waist diameter and seed waist diameter, were not disclosed at the beginning. Only recently, the last details of such amplifiers were published. Thus, it

was not possible to fully exploit the state of development and to transfer a complete system design to amplifiers with thulium pump lasers. Therefore, the development of those amplifiers began under the guidance of published details such as the crystal length and under the constraint of the actually available components. This development work by Wang and other colleagues culminated in the second to last amplifier in table 5.2 [143]. With this amplifier, Wang et al. managed to amplify a seed power of about 1 W to an output power of 3.35 W. Their amplifier was based on two consecutive single-pass amplifiers, which were pumped by a thulium fiber laser at 1908 nm with a total power of 14 W.

Beside this amplifier, one more thulium-laser-pumped femtosecond amplifier is published. It is the last amplifier in table 5.2. This amplifier used a disk-shaped gain medium, which was mounted on a rotating shaft. In this way, thermal-optical limitations were overcome by continually shifting the amplification process into newly thermalized gain material. This made it possible to use a pump power of 105 W, to increase the output by a gain factor of about 23 and to add a power of about 26 W to the output. The reported beam profile shows a deformation in one direction, presumably from the inversion gradient in the azimuthal direction. An important open question is how pronounced intensity fluctuations are in such a system. The concern is that material inhomogeneities are translated into intensity fluctuations of the output. It is presumably also necessary to decouple the amplifier from the optical table to avoid the transmission of vibrations. For these reasons, the spinning disk technology is regarded as a backup option. Instead, attempts were made to achieve the targeted average output power of 7 to 10 watts with conventional approaches without moving parts. This should be possible with Cr:ZnS amplifiers according to table 5.2.

5.3.1 Goals and Questions Addressed in this Chapter

The state of development described in the previous section led to the scientific questions and development goals addressed in this chapter. The question was how and to what extent the gap in performance between conventional thulium- and erbium-laser-pumped amplifiers could be closed and ideally reverted.

The exploration and the development of Cr:ZnS amplifiers pumped by thulium lasers were still at their beginning. It was envisioned to change this by optimizing the single-pass performance and then by following some concepts known from Ti:sapphire, like the implementation of more passes through the same amplifier crystal or the operation below 0 °C. All the findings obtained in this context will be presented in the following section on experiments.

5.4 Experiments and Findings

5.4.1 Description of Seed Oscillators

Two different seed sources were provided by colleagues and used for the amplification experiments performed. The most significant difference between these two oscillators is the amount of provided average power. The amount of applied seed power is specified if it is relevant. The other specifications are provided below and complete the description of the seed source.

The initial experiments were performed with a soft-aperture Kerr-lens mode-locked Cr:ZnSe oscillator. This oscillator was pumped by one laser diode at 1650 nm. This oscillator was the first of its kind and is described in more detail in reference [144]. An accident with a mirror mount resulted in a changed beam path within the cavity. Thus, the repetition rate of this oscillator was altered from 65 MHz to 56 MHz. The typical output power of this oscillator before the accident was about 450 mW right after the oscillator, which corresponded to about 400 mW at the amplifier crystal. After the accident, the power at the crystal was about 330 mW. The work was continued at this lower power level. The evaluations in the following subsections take these varying seed powers into account. Not much attention was paid to the spectral width of the emitted beam because the focus of the initial experiments was only on output power optimization. The presence of mode-locked operation without a CW background was, however, verified whenever needed. The central wavelength of this Cr:ZnSe oscillator was about 2.35 µm. This oscillator is referred to as Miranda 1.

Later experiments were performed with a more powerful oscillator. This oscillator was a soft-aperture Kerr-lens mode-locked Cr:ZnS oscillator pumped by two laser diodes with a wavelength of 1650 nm. This oscillator took advantage of the increased pump power, a refined pump and cavity design, and a further developed mirror technology. In this way, it could emit an average power of about 750 mW with a pulse duration in the range of 35 fs at a repetition rate of 49.9 MHz. More details on this oscillator can be found in reference [145]. Also, the output power of this oscillator experienced variations in the range of 700 mW to 800 mW over the course of about one year. The respective seed powers were determined with a thermal power sensor (S302C, Thorlabs GmbH) and are specified in the experiments or were taken into account in the evaluations. The central wavelength of this Cr:ZnS oscillator was slightly shorter at about 2.29 µm. This oscillator is called Miranda 2.

5.4.2 Description of the Pump Source

This subsection describes the pump source used for almost all amplifier experiments. It describes the characteristics of this pump source and the various forms in which this pump source has been used. This pump source was a 120 W thulium fiber laser (TLR-120-WC) manufactured by IPG Photonics. This laser will be referred to as the IPG laser in the following. It was designed to operate at a wavelength of 1908 nm, due to its previous

use as Ho:YAG pump source. The fiber laser had a collimation unit at the fiber output, so a roughly collimated beam was emitted from the unit. A Keplerian beam expander was employed to adjust the beam diameter for the application in the amplifier. For most experiments, the beam diameter was enlarged by a factor of two. The adjusted pump beam was guided in three different manners to the amplifier. All of them are discussed in the following and are illustrated in fig. 5.3.

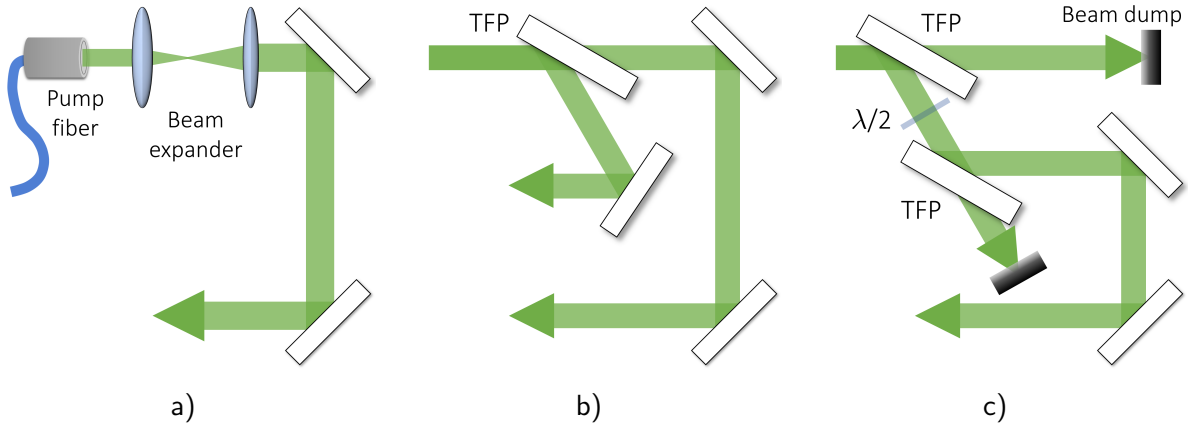

Figure 5.3: Schematics of the pump configurations (=pump schemes) used. a) Direct application of the pump light to the amplifier. The beam expander is not depicted in the other two schematics, but is still used. b) Generation of two pump beams with a thin-film polarizer (TFP). c) Generation of one power-adjustable pump beam with polarization optics.

The direct application of the pump light in fig. 5.3a was used for initial experiments. In this configuration, the pump power was regulated by setting the laser to different power setpoints.

In later experiments, additional amplifier stages were constructed. The expanded pump beam was thus split into two almost equally powerful pump beams with the help of a thin-film polarizer. A schematic of this setup can be seen in fig. 5.3b. The laser module's polarization, which was specified as "random", allowed this splitting without further components. The pump power in this configuration was again tuned via the setpoint of the laser.

A third pump configuration was realized in order to exclude setpoint-dependent variations of the pump beam. This configuration is depicted in fig. 5.3c. In this configuration, the pump source is operated at a fixed power setpoint and the applied pump power is tuned via the half-wave plate and the action of the second polarizer. This scheme eliminates variations of the pump caustic and of the intensity noise described later. It was implemented for some final investigations.

The pump beam was usually focused into the amplifier with a lens after propagation through one of the above arrangements, see fig. 5.7 on page 84 for better comprehension. The focus diameter, waist position, M^2-value and alignment of the pump beam are key parameters for the amplifier performance, as discussed in the next subsection 5.4.3. The am-

plifier's initial characterization and alignment were performed at low average power levels of about 1 W due to the damage threshold of the scanning slit beam profiler (NanoScan2-PYRO/9/5, Ophir Spiricon Europe GmbH). The actual operating point was at much higher pump powers of 20 W to 30 W. Therefore, it was necessary to check for a potential influence of the selected power setpoint on the beam caustic. This was necessary in order to clarify what conclusions could be drawn from the experiments.

A series of M^2-measurements at varying power levels was taken to check the validity of the low power measurements for higher pump power levels. The obtained data are presented in fig. 5.4. As can be seen in fig. 5.4a, the M^2-values and the waist diameter of the pump beam stayed essentially unaffected by the varying pump power level. For the location of the beam waist, a shift in propagation direction (z) can be observed in fig. 5.4b. In a separate experiment, these trends were found to continue even up to pump powers of more than 60 W. The steadiness of the waist diameters and M^2-values were prerequisites for the validity of the characterization at low pump power and the permissibility of the direct regulation of the pump source. The shift of the pump waist position was regarded as uncritical for the power optimization of the amplifiers, because the waist position was tunable via the z-position of the focusing lens and would have been optimized for the highest possible output power at high pump powers anyway. Thus, the maximal achievable output power was not affected by the variation of the pump source and a direct adjustment of the pump power via the power setpoint was permissible, so long as one can ignore the variation in the relative intensity noise of the pump source. This variation in intensity noise will be introduced at the end of this subsection.

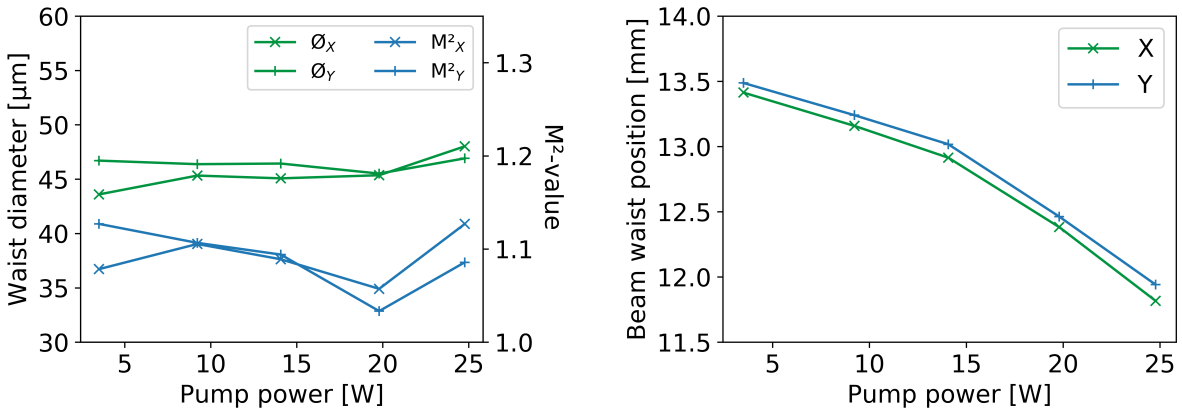

Figure 5.4: a) Evolution of the diameters and M^2-values of the IPG pump laser over the chosen pump power. b) The location of the pump waist in z-direction plotted over the applied pump power.

After the focusing lens, the converging pump beam usually enters the amplifier through an input coupler. For this input coupler, another interesting pump-power-dependent effect was observed. The type of input coupler used heated up, as documented by the recording

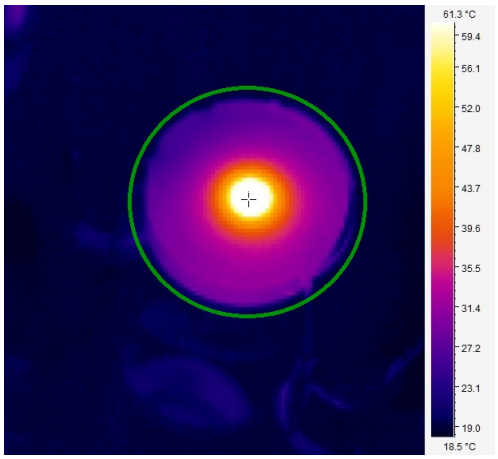

Figure 5.5: Thermal image of an IC1605 input coupler under pump load. The hot spot indicates the region where the pump beam penetrates the mirror. The mirror substrate is circled in green and has a higher temperature than the cold background. The thermographic camera (EC060V, Trotec GmbH) was not calibrated for this measurement.

with a thermographic camera in fig. 5.5. The heating up of the input coupler was noticed as a drift in seed beam alignment, which significantly influenced the performance of the amplifier. The heating up of the mirror substrate was also proven with thermochromic film. The observed alignment drift is then probably simply a consequence of the subsequent heating up of the mirror mounting tip and of the mirror mount. The drift was, to a large extent, reproducible. This means that the amplifier essentially returned to its previous hot-state performance after an interruption with a cooling of the structure. Nonetheless, the alignment drift represents an additional source of variation. Therefore, the alignment optimization was always performed as part of the determination of the maximum output power. The heating up and its thermal bulge were ruled out as the main cause of the shift in waist position, because the shift was also observed when the input coupler was bypassed. The input coupler used was the model IC1605. Its HR-coating was identified as the cause of the warming because comparable bare mirror substrates did not show this effect. The production of an alternative input coupler with other coating materials was organized. Like most of the specialized mirrors, these new mirrors were also produced at our institute. These mirrors with the name IC2003 are available at the time of writing. Their performance remains to be tested.

The intensity noise of the amplifier output is an important parameter for the Infrasampler application. It is partially determined by the intensity noise of the pump source. Therefore, a series of noise measurements was made to quantify the pump noise. In one set of measurements, the question was addressed, if the polarization splitting from fig. 5.3b and fig. 5.3c influences the intensity noise of the pump light. For this purpose, the pump light was analyzed under the same circumstances before and after the polarizer. The recorded intensity noise spectra of the polarized pump light and of the original pump light can be seen in fig. 5.6. These power spectra already suggest a difference between these two pump

beams. A quantitative measure of the intensity noise is the calculation of the integrated RIN_{rms} as defined in appendix A. The computation of this quantity for the displayed frequency interval resulted in a value of about 0.42 % for the original beam and in a value of about 0.65 % for the polarized beam. This means that the beam after the polarizer exhibits more intensity noise. This observation can be qualitatively explained by assuming that the available amplification in the laser leads to some anticorrelation between the powers of the two polarization axes. While a single polarization axis might exhibit stronger fluctuations, these fluctuations would then partially compensate each other when measuring the sum of both axes. Thus, the full extent of the fluctuations would only be visible after a polarizer. In this way, polarization splitting could degrade the noise properties of the pump source. This degradation is unfavorable for the later application because it increases the intensity noise of the amplifier output. It is thus advisable to get polarization-independent, partially reflective optics for a splitting of this source as in fig. 5.3b.

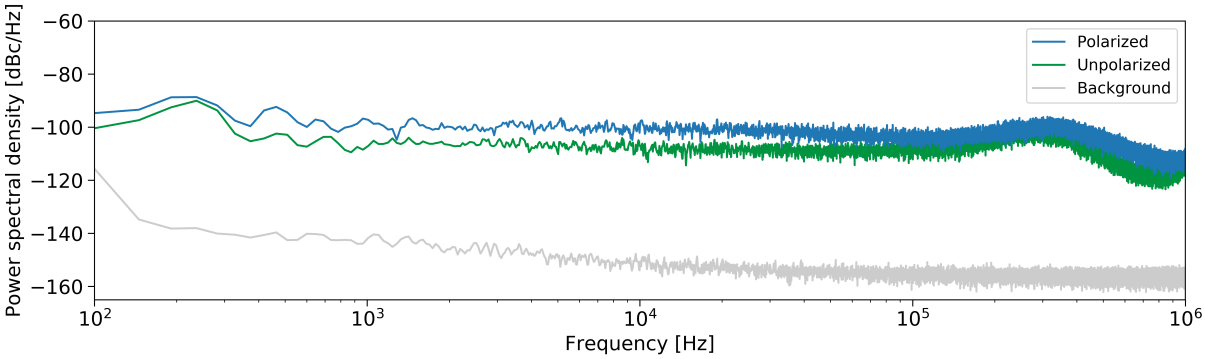

Figure 5.6: The power spectrum of the intensity fluctuations of the IPG pump source before and after a polarizer.

Another general observation is that the intensity noise power spectrum of this pump laser changes its shape as one changes the power setpoint. The peak at about 300 kHz in fig. 5.6 shifts to higher or lower frequencies for higher or lower output powers. This could be exploited to optimize the noise performance in a certain low-frequency band. The measurements shown in fig. 5.6 were taken at a total output power of about 55 W.

The surrounding infrastructure has now been described in sufficient detail. Now the design and optimization of the single-pass amplifier can be discussed in the next subsection.

5.4.3 Optimization of the Single-Pass Amplifier

A single-pass amplifier is the simplest realization of an optical amplifier. A possible implementation of such an amplifier is depicted in fig. 5.7. It consists of a gain crystal, an input coupler (=a dichroic mirror), a second mirror for the seed beam and a focusing lens. The input coupler focuses the seed beam into the gain crystal and enables the combination of the seed beam with the pump beam. The second mirror allows the alignment of the seed

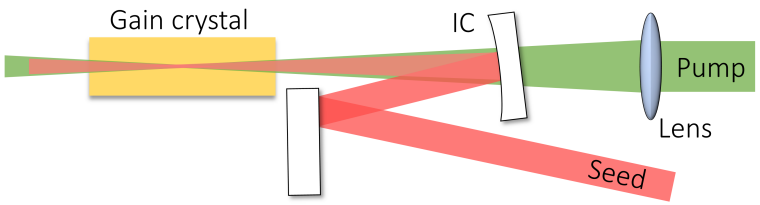

Figure 5.7: Schematic of a single-pass amplifier. IC stands for input coupler.

beam to the pump beam. The focusing lens focuses the pump beam through the input coupler into the gain crystal. The focusing lens is usually mounted on a linear translation stage to have control over the z-position of the pump waist. Also, the crystal in its mount is usually attached to a 3-axis translation stage to allow a repositioning of the crystal. Two additional input couplers were used to separate pump and seed again after the gain crystal.

Key design parameters of single-pass amplifiers are the diameters of the pump and the seed beam within the gain crystal, and the doping concentration and length of the gain crystal. The parameters of the gain crystal were initially selected on the basis of reported values and availability. The goal for the diameters is to maintain high intensities over the entire crystal length. Thus, one needs to find a good tradeoff between the minimal diameter of the beam (the beam waist with a diameter of $2w_0$) and how fast it then diverges, recall eq. (2.28) and eq. (2.29). In addition, the pump beam should ideally show the same caustic as the seed beam, such that there is maximum overlap between the two and no pump energy is wasted. An identical beam caustic is, however, not possible for beams of equal beam quality due to the difference in wavelength and the slightly different divergence, which comes with this.

The ideal focusing parameters and their analytical dependencies are usually unknown due to the complex interplay between the caustics and the amplification process [158]. Good focusing parameters must be sought by numerical [158] or experimental means. Even if the ideal parameters are known, in the real implementation, one has to work with the given M^2-values and the accessible waist sizes, which are defined by the available input couplers and the available lenses. Therefore, considerations of minor details of the beam caustics should be avoided.

However, some simple considerations with a beam propagation tool (e.g. reZonator) are useful for the estimation of the waist sizes during the design of the amplifier. In such simulations, the seed waist is defined by the ROC values of the available input couplers and by the properties of the incident seed beam. The latter can be modified with refractive elements if necessary. The considerations for the pump beam are more complex than for the seed beam. A constrain is that the focusing lens in fig. 5.7 must have a longer focal length than the input coupler to allow an overlap of the waists in z-direction. This sets a lower limit for the usable focal length of the focusing lens. The simulation of the pump beam focusing should take the input coupler into account because it acts as a plano-concave lens on the pump beam. The focal length f of this plano-concave lens can be estimated by eq. (5.1), which is a special case of the Lensmaker's Formula [29, p. 167]. In this equation,

ROC is the radius of curvature of the input coupler (caution with the sign conventions) and n is the refractive index of the input coupler substrate.

$$f = -\frac{\mathrm{ROC}}{(n-1)} \tag{5.1}$$

Regarding the pump waist diameter, a diameter of 50 µm was used in the early publication [159]. In verbal communication with the author of reference [143], it was learned that the amplifier in this reference used a pump waist diameter of 75 µm and a seed waist diameter of 70 µm. Therefore, a waist diameter of about 60 µm was initially targeted for 9 mm long gain crystals. A crystal length of 9 mm was chosen since nearly all relevant amplifiers use this length, see, for example, table 5.2. If one performs the previously mentioned beam simulations for the targeted waist size, then one finds that a quite large pump beam is needed as input to the focusing lens. This may require the use of a beam expander, as is the case with the thulium fiber pump source, as illustrated in fig. 5.3.

More detailed information about the influence of the waist diameters on the amplifier performance was not available. To determine this influence, the parameter space formed by the pump waist diameter and seed waist diameter was examined. This investigation was performed along the diagonal of equal diameters since this direction was suspected to be the most influential direction. Accordingly, four amplifiers with different input couplers and lenses were built to realize four different diameter configurations. The gain crystal for these experiments was specified by the manufacturer (IPG Photonics) to have the dimensions $1.9 * 2.9 * 9.0$ mm. The $1.9 * 2.9$ facet was AR-coated with a residual reflectivity of below 1 % over the range from 1500 nm to 3000 nm. The doping level of the crystal was specified via its transmission at 1560 nm. For this wavelength, the transmission was 3.4 % through the length of the crystal. The crystal was wrapped in indium foil to establish a good contact between the crystal and the cold surfaces of its mount. The mount was made out of copper and clamped the crystal gently. O-ring seals can be used instead of washers to introduce a desired amount of flexibility into the clamping. The picture in fig. 5.24a on page 110 displays such a copper mount. The pump light of the thulium laser was directly applied to the amplifier, as described in fig. 5.3a. The seed power was about 410 mW from the Cr:ZnSe oscillator "Miranda 1" and the applied pump power was 20 W. Such an amplifier arrangement has the following remaining degrees of freedom: the position of the gain crystal, the propagation direction of the seed beam (the alignment) and the waist location of the pump beam. The performance of each amplifier was optimized by tuning these parameters during operation. The findings of these experiments are summarized in fig. 5.8.

The configuration with waist diameters of 260 µm and 270 µm, located in the top-right corner of fig. 5.8, proves that too large beams with too little intensity in pump and seed do not lead to efficient amplification. For such beams, the pump generates a less pronounced population inversion and more of the excitation decays before the low seed photon density can trigger a stimulated emission process.

Accordingly, amplifiers with smaller waist diameters perform better. This trend should continue until an ideal focal spot size is reached. For even smaller waist diameters, the

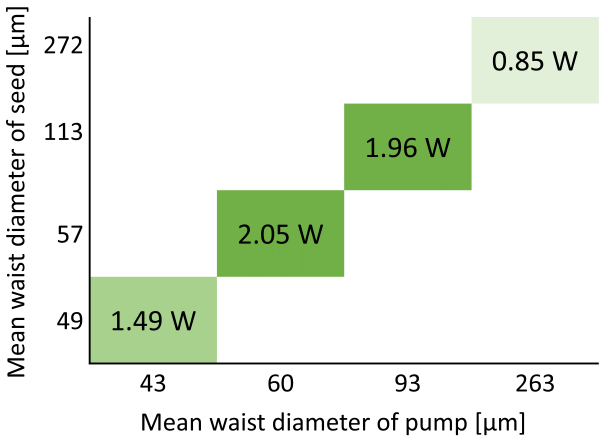

Figure 5.8: Output powers of amplifiers with different pump and seed waist-sizes. The mean diameters are displayed because the variations between the x- and y-direction were small. It was attempted to keep the distance between the laser beam and the bottom of the crystal constant because this distance significantly influenced the emitted power.

caustic diverges more and remains confined over a shorter distance. For a beam centered in the middle of the crystal, this would lead to two sections with a rather large diameter and a very short section with very high intensity. Therefore, such a smaller waist diameter should result in lower performance. This idea could explain the performance drop observed for the configuration with waist diameters of 40 µm and 50 µm. However, a more likely explanation for this decay is probably the experimental implementation and its limitations. This amplifier used a ROC 100 mm input coupler. Accordingly, there were only about 45 mm left between the input coupler and the crystal facet. This space had to be sufficient for one more mirror and the steering of the seed beam onto the input coupler, as depicted in fig. 5.7 on page 84. This constraint made rather large angles of incidence necessary and the resulting arrangement degraded the seed beam in terms of astigmatism and beam quality. The presence of strong astigmatism can be seen in the unusually large separation of about 2.5 mm between the foci of the seed beam, as shown by the blue lines in fig. 5.9a. For comparison, this figure also shows a seed waist with the usual focus separation of about 0.7 mm in green. The data in fig. 5.9b indicate the expected negative influence of astigmatism on the amplification process. This measurement shows the output power of the amplifier for various pump lens positions. The pump lens position defines the location of the pump waist. While optimizing this pump lens position, two power maxima were found, which were about 2.5 mm apart. As expected, the amplification process is stronger when the pump waist is adjusted to a seed waist. It, therefore, seems very plausible that the amplification would have been even stronger if both seed foci had coincided. These observations make it likely that the experimentally induced astigmatism largely contributed to the performance reduction of this configuration.

The amplifiers with waist diameters of 100 µm and with waist diameters of 60 µm did not differ much in performance. This observation can be justified with the Rayleigh length

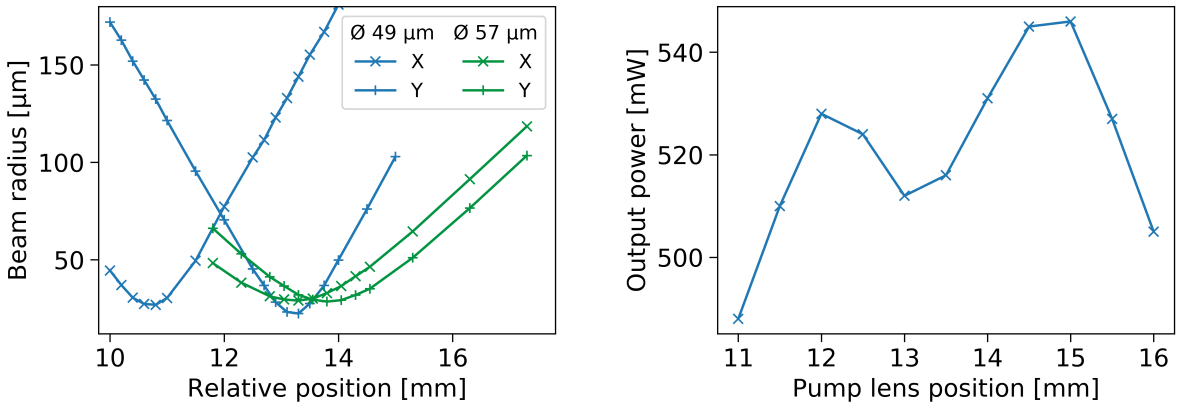

a) b)

Figure 5.9: a) Recorded seed focus for the ROC 100 mm (Ø 49 µm) and ROC 200 mm (Ø 57 µm) input coupler. X and Y are the labels for the two orthogonal axes of the scanning slit beam profiler. The waists of the 49 µm-configuration show a much greater separation than the typical separation shown in the 57 µm-configuration. b) Output power recorded for the amplifier with ROC 100 mm input coupler over various pump lens positions. Two maxima were found for the shift in pump lens position.

z_R, which was introduced in eq. (2.28). For a seed beam with a diameter of roughly 76 µm, the Rayleigh length equates to roughly half the length of the 9 mm long gain crystal. Thus, a high intensity is established and maintained over the entire crystal length. Matching the double Rayleigh length to the crystal length seems to be close to the optimal design, because the corresponding diameter is located between the very similar 100 µm- and 60 µm-configuration. Most of the subsequent experiments were then performed with waist diameters of 60 µm to 70 µm.

Challenging in this investigation was that the output power of the amplifiers exhibited a strong dependence on the location of the gain volume within the amplifier crystal. Output powers higher than those stated in fig. 5.8 were possible by moving the laser beams even closer to the bottom of the crystal. Therefore, it was attempted to operate all amplifiers with the same distance between the laser beams and the crystal's bottom. There is still some uncertainty in this measurement because the construction of a new amplifier configuration required an unscrewing of one of the crystal-mount's stages. While this small source of variation could not be avoided, the experiments nevertheless resulted in the clear trend reported here. The observed location dependence is discussed in more detail below.

Location Dependence of the Amplifier Performance

An investigation of the achievable power depending on the transverse location in the crystal can be seen in fig. 5.10a. This graph illustrates with a color-coding the obtained output power at the minimum pump power for different locations within the crystal. It can be

seen in this graph that the output power in this crystal depended with up to 9 % on the horizontal position and with up to 27 % on the vertical position. In fact, the vertical position was even more crucial at higher pump powers, as the scan in fig. 5.10b illustrates. In this graph 5.10b, the output power changes by 167 % for the same vertical position change as before and height changes of as little as 50 µm caused power changes of up to 10 %.

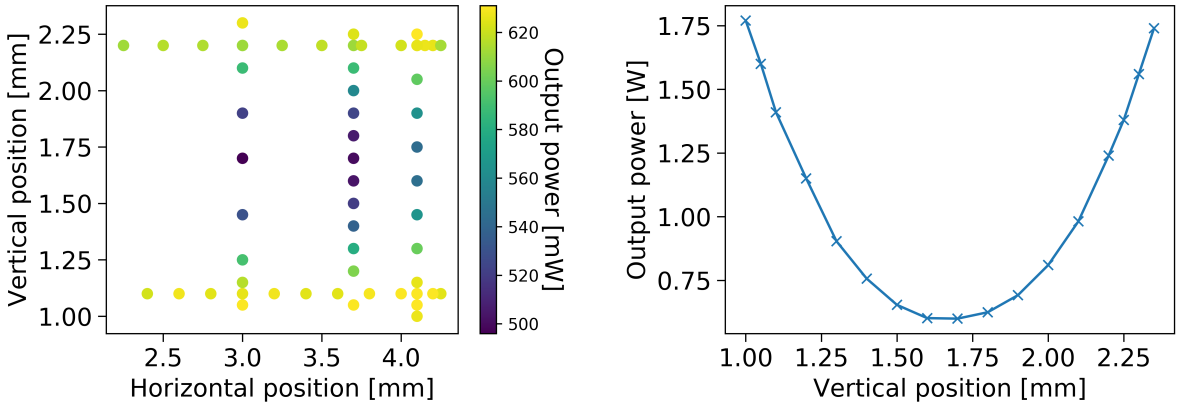

a) b)

Figure 5.10: a) A spatially resolved plot of the output power obtained for various positions within the gain crystal. A pronounced dependence on the vertical position and a moderate dependence on the horizontal position was observed. The best performances were obtained at the top and bottom of the crystal. The displayed position values are relative values without well-defined references. Under the assumption of equal residual distances, the crystal edges have been approached to about 0.3 mm in the vertical direction and to about 0.4 mm in the horizontal direction. Depending on the input beams, a distance of at least about 0.2 mm is required for the beam caustics. This scan was performed with the lowest possible pump power of about 1 W and a seed power of 425 mW. b) The graph shows the obtained output power for different locations of the gain volume in vertical direction in more detail. This scan was performed with a pump power of about 10 W and a seed power of 416 mW. It exemplifies the huge role of the vertical position for the amplification in this crystal.

In later experiments, it was possible to identify the reason for the spatially varying amplification performance. The observation was that the variation in performance correlated with the small-signal pump light absorption of the crystal. Such measurements are shown in fig. 5.11. These measurements were made for a crystal with a specified transmission of 5.3 % through its length of 9 mm for a wavelength of 1560 nm. For the measurement of the small-signal pump light absorption, the crystal in the amplifier configuration was exposed to 28.5 mW of pump light. At such low power levels, the measured absorption is a good approximation of the small-signal absorption. The spatially resolved absorption was then obtained by measuring the light transmitted through the crystal with a thermal power sensor (S302C, Thorlabs GmbH) for the respective vertical positions of the crystal. This led

to the displayed absorption-height profile in fig. 5.11. The observation was that the small-signal absorption increased toward the borders of the gain crystal. This could have been due to a deteriorating optical quality of the crystal or an increase in doping concentration, and the next experiment suggests that it is due to the doping concentration.

For the spatially resolved gain measurement in fig. 5.11, the amplifier was pumped with 31 W. After thermalization and optimization of the amplifier, the emitted output power was recorded for the respective vertical position and normalized to the incident seed power. In this way, it was again found that the amplifier performance strongly depends on the proximity of the pumped volume to the edge of the crystal. There at the cooled edges of the crystal, a slightly lower temperature in the pumped crystal region might also contribute to the stronger amplification. However, this improved cooling is a moderate contribution at best, because the influence of temperature is too small, as will be seen in subsection 5.4.4, and some of the other Cr:ZnS crystals bought from the same supplier do not exhibit comparable height dependencies.

The combination of the observations suggests the presence of a spatially varying chromium concentration in the corresponding crystals and a strong influence of the doping concentration on the performance of the amplifier. Accordingly, the influence of the doping concentration is further investigated later in subsection 5.4.7. These investigations verified the strong influence of the doping concentration.

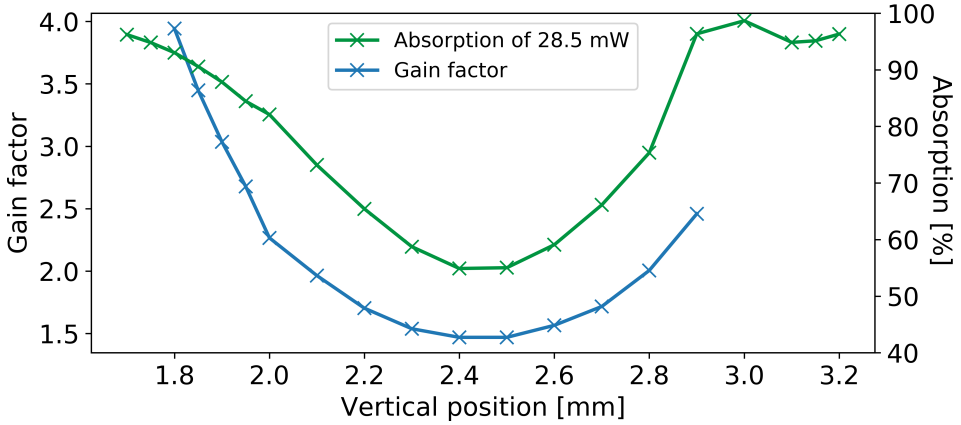

Figure 5.11: The graph displays the vertical dependence of the gain factor and the pump light absorption. The graph could be as symmetric as the one in fig. 5.10b, but during the measurement, a damage at the front surface occurred at position 3.0 mm. The vertical position values are relative values without well-defined reference. The measurement covered 1.5 mm of the crystal height of 1.9 mm and should be centered.

The crystal supplier (IPG Photonics) confirmed that their crystals can exhibit spatially varying doping concentrations and clarified that the specified transmission value is an averaged value. It is advisable to determine the transmission profile at mW pump power level in each new amplifier. In this way, one gains insights into the doping structure and gets familiar with the possible stage positions.

After these first few important insights into the key design parameters of Cr:ZnS amplifiers, the influence of the wavelength of the thulium pump laser is discussed next.

Influence of the Pump Wavelength

Thulium fiber lasers are available with slightly different wavelengths. The IPG thulium fiber laser used so far operated at a wavelength of 1908 nm, which is an atypical wavelength for thulium fiber lasers. The experiment reported in this paragraph tested if a more common wavelength such as 1946 nm could be used as well. A laser with such a wavelength was available at our institute. This new laser, which has lower intensity noise then the IPG laser, was manufactured by Futonics Laser GmbH and could deliver an average power of about 17 W to the crystal. It produced a beam caustic that remained essentially unaffected by a change in output power. The question, if one can use this low noise laser at 1946 nm as pump source for Cr:ZnS amplifiers, was addressed by comparing the performance of a particular amplifier configuration, which was pumped once with the laser at 1946 nm and once with the laser at 1908 nm. The amplifier had pump and seed diameters of 70 µm

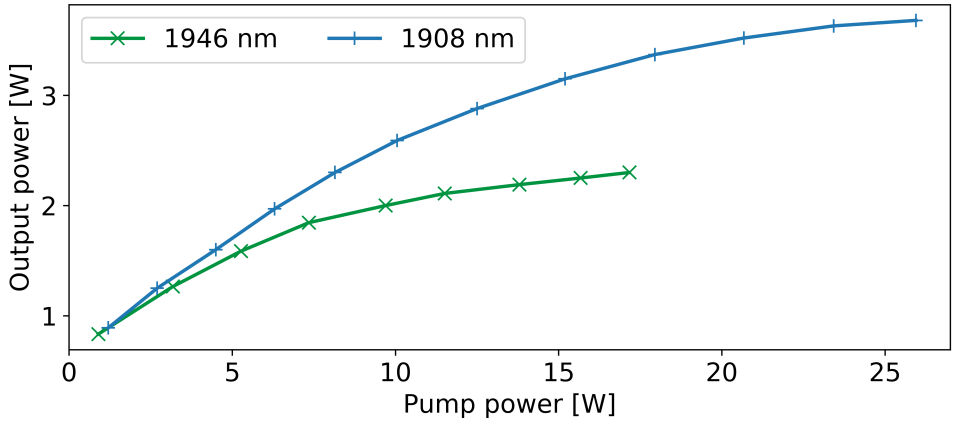

Figure 5.12: The measured output power - pump power performance of one amplifier configuration realized for two different pump wavelengths.

and was operated at the same crystal height setting for both pump light sources. The crystal in use was specified to have a transmission of 5.2 % at 1560 nm through its length of 9 mm. The amplifier was seeded with an average power of about 730 mW from the more powerful Cr:ZnS oscillator "Miranda 2". Regardless of the equal amplifier configuration, the obtained performance for the pump sources differed quite a bit. For the pump wavelength of 1908 nm, an output power of 3.68 W was reached, which corresponds to a gain factor of about 5. For the amplifier pumped at the wavelength of 1946 nm, less pump power was available. Nonetheless, it is clearly visible in fig. 5.12 that this configuration will not reach competitive power levels, even with more pump power. The amplifier with the pump source at 1946 nm was bound to a gain factor of about 3. The observed reduction in performance is most likely due to the change in absorption. The pump absorption changes

unfavorably for increasing pumping wavelength for two reasons. First of all, the absorption cross-section itself shrinks with increasing wavelength. Secondly, the reemission at the pumping wavelength becomes more likely due to an increasing emission cross-section for longer pumping wavelengths (eq. (2.15)). An increase in chromium doping concentration can partially compensate for these changes. However, it is unclear how much the doping concentration can be raised and if the higher doping has side effects. Conceivable limiting factors for the doping concentration are a degradation of the crystal in optical quality and the occurrence of concentration quenching. In conclusion, Cr:ZnS amplifiers with wavelength-tuned thulium pump sources are more promising.

This was the only experiment in which a pump source other than the tuned IPG laser was used. All experiments described below use again the IPG laser.

Output-Power Rollover

The previous figure 5.12 also exemplifies a typical behavior encountered in all amplifiers up to now. The graph shows that the increase in output power decreases with growing pump power. This decrease continues until hardly any slope is left or even a decrease in output power occurs.

It was excluded that this rollover is caused by the waist shift of the IPG laser by optimizing the pump lens position and the crystal position. Other possible reasons for this rollover could be a bleaching of the crystal, a self-focusing in the crystal, the formation of a strong thermal lens or a reduction of the upper-state lifetime due to a raising core temperature. Some of these potential causes will be tested later on page 98, because the elimination of the rollover would result in significantly higher output powers. These experiments are discussed later since they involve the Peltier-cooled crystal mount.

Dependence of the Relative Intensity Noise on the Applied Pump Power

The previously described power rollover also motivated an investigation of the amplifier's intensity noise and its dependence on the applied pump power, because the observation is that the output of the amplifier saturates at some point with respect to the applied pump power. If this behavior is also valid on much shorter time scales t <1 ms, then spikes in pump power should only be partially transferred to the output of the amplifier. This would be equivalent to a damping in the pump-seed noise transfer and should naturally be more pronounced for pump noise at higher frequencies. The experiment now being discussed attempted to test the presence of this effect. For this purpose, the specialized pumping scheme of fig. 5.3c had to be used, because the IPG pump laser itself varies in noise for different power setpoints. This scheme avoids these variations of the pump laser by operating the unpolarized pump laser at a high power level and by tuning the amount of applied pump light with two polarizers and one half-wave plate. In this way, the amount of applied pump light is decoupled from the noise properties of the pump light. The accordingly constructed amplifier had pump and seed diameters of about 65 µm, was seeded with about 735 mW and delivered an output power of up to about 2.9 W. A series

of intensity noise measurements was made for this amplifier at different pump power levels over the entire operating range. The obtained data can be seen in fig. 5.13. The output

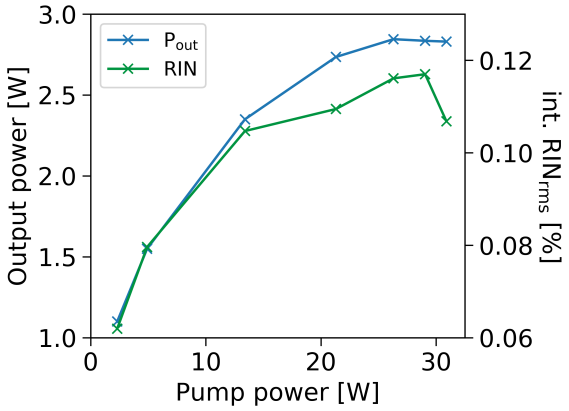

Figure 5.13: The graph shows the dependence of the emitted output power and the dependence of the measured square root of the integrated relative intensity noise on the applied pump power.

power curve in this graph shows that the amplifier was tested well into its saturation. The green curve in fig. 5.13 describes the integrated relative intensity noise root-mean-square for the range from 1125 Hz to 1.9 MHz. This graph shows that the intensity noise grows as the seed is amplified. This is expected because a larger fraction of the emitted power is then dependent on the supplied pump power. The trend in the saturated regime is not absolutely clear due to the deviation of the last data point. This data point could be an outlier or indicate a pump-power threshold of the noise damping. As this data is the result of one measurement campaign, one would need to risk more investigations at higher pump powers to obtain a conclusion on this matter. The risk of these measurements is the occurrence of crystal damage as described in subsection 5.4.7. Independent of the existence of damping, future pump sources should have as little intensity noise as possible.

As a result of the optimization of the amplifier implementation, a single amplifier stage can deliver now an output power of about 3 W with a gain factor of about 4. A single stage is now as powerful as the double stage demonstrated in reference [143]. The targeted power for powerful mid-IR generation and electro-optic sampling is, however, higher, such that further investigations were carried out. One pursued approach was to amplify at low temperatures. This direction of development is presented in the next subsection.

5.4.4 Influence of Temperature on the Amplification Process

Temperature and thermal management become an important topic in laser physics as soon as high average powers are targeted. As introduced in subsection 5.2, Cr:ZnS has, like many other gain materials, a temperature-dependent upper-state lifetime. This lifetime is important for the amplification process, because it affects the rate of spontaneous emission, which competes with the desired stimulated emission for the available population in the

upper laser level. This lifetime shows a rapid decline for temperatures higher than ambient, as was shown in fig. 5.2 on page 76. The shorter this lifetime becomes, the more excitation is lost by spontaneous emission. Therefore, one wants low crystal temperatures for longer lifetimes. This temperature-dependent lifetime was also regarded as a possible explanation for the rollover of the output power at high pump powers, because it was conceivable that an increase in core temperature could cause the stagnation of the output power. Figure 5.12 showed such a rollover. Without the rollover, the initial slope would lead to much higher output powers. Accordingly, the potential for improvement by lowering the crystal temperature was estimated to be high. This reduction in temperature would additionally cause a rise in thermal conductivity [160]. This higher thermal conductivity would reduce the magnitude of the temperature gradient within the crystal. The reduced gradient, in turn, leads to even slightly lower core temperatures and, more importantly, to less thermal lensing. Therefore, another expectation was that a lower crystal temperature would also lead to an improved beam quality by reducing higher-order aberrations introduced by the thermal lens [161]. A reduction in crystal temperature required a further reduction in the temperature of the crystal mount and the removal of ambient air, as the temperature of the crystal mount was already close to the dew point. Since condensation of atmospheric moisture had to be prevented in any case, a temperature well below freezing became the target for the crystal mount. Such a temperature can be achieved in different ways. An option would be to equip a suitable recirculating chiller with an ethylene glycol-water mixture as working fluid and to cool the crystal mount with this fluid to sub-0 °C temperatures. In this approach, one needs to prevent the condensation not only at the crystal but also along all the supply tubes. The alternative to this approach is to generate the cold locally, for example, with Peltier elements. The Peltier elements allow a very flexible and stable temperature control and the realization of the targeted temperature with little effort. Furthermore, when using Peltier elements, one needs to prevent condensation only at the crystal and its surrounding copper structure, which can be achieved by operation in a sealed-off, dry-nitrogen-flushed volume. If this volume is reduced in size to contain only the necessary parts, then the translation stages and mirrors of the amplifier remain directly accessible. The mount should then be further reduced in size so that it fits into the existing amplifier configurations. During the course of this thesis, it was possible to design and assemble a mount that meets all of the above requirements. A picture of this mount in parts and a picture of this mount in operation can be seen in fig. 5.14.

Seed and pump light were transmitted through standard AR-coated ZnSe windows (Thorlabs GmbH) into the miniature chamber surrounding the gain crystal. The enclosing dome was made of transparent polymethyl methacrylate. The transparency was, however, lost during production. Therefore, the ZnSe windows had to be used for crystal observation as well. The sealing of the volume does not need to be perfect because a small leakage of dry nitrogen helps to counteract the inflow of water vapor from the surrounding. The usage of gaskets is, therefore, not mandatory. The constructed mount can host one $30 * 30$ mm Peltier element below the crystal and one $20 * 20$ mm Peltier element above the crystal. A stacking of equally sized Peltier elements is possible, but it does not significantly lower the achievable temperature due to the additional heat generated by the additional

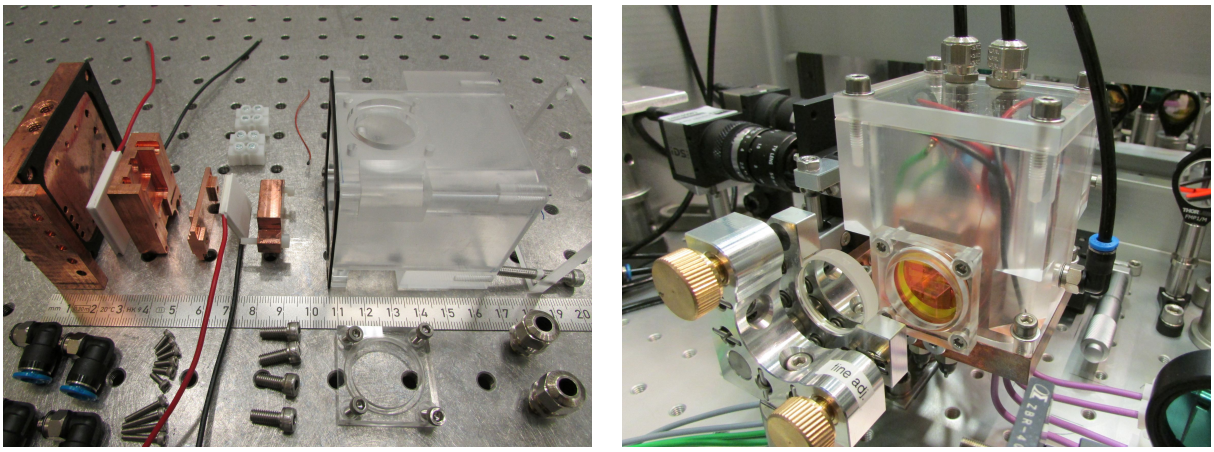

Figure 5.14: The Peltier-cooled crystal mount in parts and fully assembled in the amplifier.

Peltier elements. Instead, a close proximity of the cooling channels to the Peltier elements, a turbulent flow in those channels and the lowest permissible coolant temperature help to achieve low crystal temperatures. For the measurement of the actual temperature, two NTC thermistors were installed near the gain crystal. Their temperature-dependent resistance was used together with the Steinhart-Hart equation to infer the temperature of the copper next to the crystal. A simple check of the temperature measurement with ice and hot steam at ambient pressure resulted in 0.26 °C and 99.1 °C and built trust into this read-out setup.

The temperature of the crystal mount and gain crystal could now be changed by the amount of electric current sent through the Peltier elements. When no pump light was applied, the temperature could reach −37 °C. During regular operation, the lowest accessible temperature was −28 °C due to the heat load of the amplification process.

A seed power of about 775 mW was available for the amplification experiments. This power was measured just before the seed beam entered the mounting module. The losses caused by the AR-coated windows of the module are not taken into account because they are not relevant for the investigation of the temperature dependence. The crystal in use was specified to have a transmission of 5.2 % at 1560 nm through its length of 9 mm.

The amplifier was operated at its output power limit with a pump power of 28.3 W, which led to an output power of about 3.8 W for cooled operation. The observed dependence of the emitted power on the temperature of the crystal mount is shown in fig. 5.15. The reduction in crystal temperature by about 50 °C led to an increase in power by about 19 %. This amount of improvement was confirmed in multiple temperature cycles. It was necessary to rule out a location change within the crystal by thermal expansion in order to attribute this improvement to the temperature reduction. A camera was used for this purpose. This camera monitored the position of the generated harmonic light relative to the gain crystal during the temperature cycles. The recorded images showed only a tiny motion within the glowing structure. The magnitude of this motion was negligible compared to the change in height required to cancel out the advantage of low-temperature

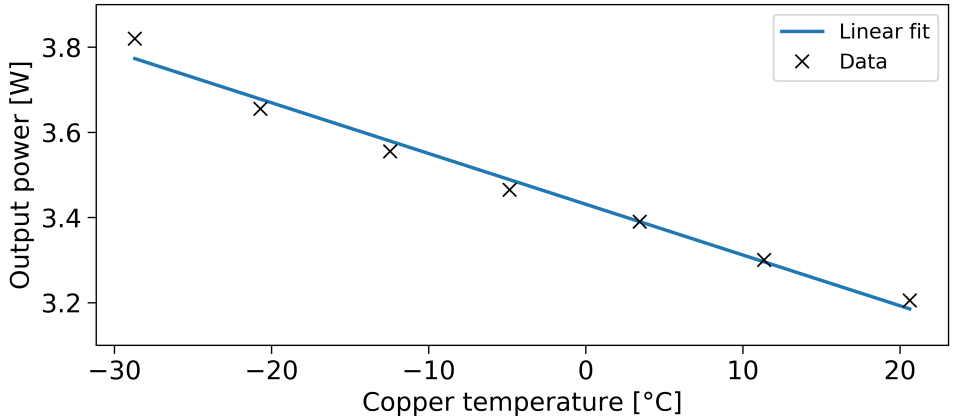

Figure 5.15: The graph shows the obtained amplifier output-power plotted against the temperature of the crystal mount. The measured data agree well with a linear fit function. The reduction in cooling temperature by about 50 °C leads to an increase in output power by about 19 %.

operation. Therefore, it is concluded that lower crystal temperatures have a positive effect on the amplification.

Influence of Temperature on the Beam Quality

As motivated at the beginning, the reduction in crystal temperature could also have a positive effect on the beam quality. This hypothesis was tested by measuring the transverse intensity profile and the beam quality factor for the minimal crystal temperature and for an ambient crystal temperature in an otherwise unchanged amplifier. These temperature states will be called "cooled" and "warm" in the following. Figure 5.16 shows the beam profiles of the warm and cooled amplifier. In this measurement, the amplifier was seeded with about 710 mW, such that the output power of the warm amplifier was about 2.9 W and the output power of the cooled amplifier was about 3.5 W. The corresponding amplification factors agree well with the previously described performances. Accordingly, the same is also true for the power improvement factor delivered by cooling. For the measurement, the amplifier output was attenuated by two output couplers and a neutral density filter. A pyroelectric array camera was then used to record the intensity beam profiles. The obtained beam profiles in fig. 5.16 differ mainly in size, which probably means that the beam caustic in the amplifier depends on the amplification strength due to processes like gain guiding, self-focusing and thermal lensing. The more important observation is that no severe beam degradation is visible in the far field for either of them.

A series of M^2-measurements was made to further quantify the beam quality caused by the crystal's operating temperature. The seed power in this experiment was about 745 mW. The output power of the warm amplifier was 3.13 W and the output power of the cooled amplifier was 3.70 W. The spectra emitted by the warm and cooled amplifier

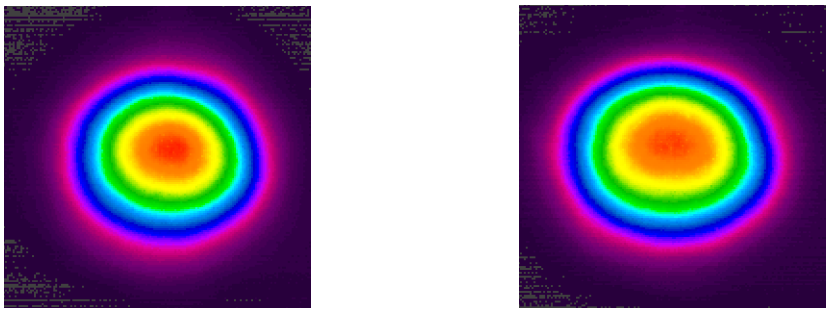

a) b)

Figure 5.16: a) Intensity beam profile emitted by the amplifier with the gain crystal at ambient temperatures. b) Intensity beam profile emitted by the amplifier with the cooled gain crystal.

were essentially the same. Details on this follow later in fig. 5.17. The respective spectral center of mass was used for the M^2-evaluations. These centers were all within 2 nm of 2283 nm. The averaged M^2-values of the measurements are listed in the second column of table 5.3. Contrary to expectation, it was found that the beam quality is slightly worse in cooled operation. The largest deterioration is from 1.16 to 1.20. This deterioration in beam quality is another plausible explanation for the change in beam diameter observed before in fig. 5.16.

A part of the slightly elevated M^2-value could be due to the amplifier arrangement itself. The M^2-value without amplification was measured to be 1.11 and 1.13 in the horizontal and vertical plane. Therefore, already the passive amplifier arrangement has a slightly elevated M^2-value. The deterioration in operation might again be attributed to gain guiding, self-focusing or thermal lensing, and the stronger amplification due to cooling could cause the additional slight deterioration for cooled operation.

Table 5.3: Properties of the Peltier-cooled amplifier.

Configuration	M_X^2 / M_Y^2	Extinction ratio pumped	Extinction ratio unpumped
Warm	1.16 / 1.16	270	200
Cooled	1.18 / 1.20	46	36
Cooled + $\lambda/4$ plate	–	285	–

For the same output power level, the polarization of the amplifier and its temperature dependence was investigated. A pure, linear polarization is the desired output polarization for later Infrasampler applications. Accordingly, the polarization was quantified in terms of the achievable extinction ratio. The extinction ratio is the ratio of the maximum and minimum measurable power that can be measured behind a rotating polarizer. Therefore, a large extinction ratio corresponds to a large fraction of the light being in one plane of polarization, which is the desired polarization state.

The polarizer used for this measurement was a wire grid polarizer (WP25M-UB, Thorlabs GmbH). This polarizer is specified to have an extinction ratio of about 10 000 or higher. It is, therefore, suitable for analyzing the extinction ratio of the amplifier output. The power meter in use was the S302C unit from Thorlabs. With those measuring instruments, an extinction ratio of up to 800 was found for the output of the oscillator. Measurements of such high extinction rations have relatively low precision, because it is hard to measure sub-1 mW powers reliably, while small deviations substantially influence the obtained extinction ratios. For the amplifier measurements, the beam was attenuated with an output coupler made of Infrasil. The findings for the amplifier are summarized in table 5.3. For the cooled amplifier, an extinction ratio in the range from 36 to 60 was found. This is substantially worse than for the same arrangement operated at ambient temperatures. For ambient temperatures, extinction rates in the range from 210 to 325 were found. Interesting is that the same tendency is even observed without amplification. This was tested by examining the seed beam after its propagation through the unpumped amplifier. For this case, an extinction ratio of 36 was obtained for the cooled gain crystal and an extinction ratio of 200 for the warm amplifier. Therefore, the reduction of the extinction ratio is not related to the amplification process. Another positive observation is that the reduction is reversible. It was, for example, possible to improve the polarization of the cooled, pumped amplifier with a quarter-wave plate. In this way, the extinction ratio could be restored to a value of about 260 to 310. The need to use a quarter-wave plate is a semi-ideal solution due to the additional material dispersion. Future investigations could clarify if the polarization modification is related to the mechanical mounting or to the temperature of the crystal. Perhaps the polarization modification is just stress-induced birefringence due to a shrinking of the clamping screws or a stiffening of the rubber O-rings and can potentially be omitted. If the cleanness of linear polarization really needs to be optimized, then one should also be aware of the fact that ordinary mirrors and their usage are of importance. For example, metallic mirrors preserve linear polarization only if the polarization is truly s or p with respect to the incident plane on that mirror [162, p. 228].

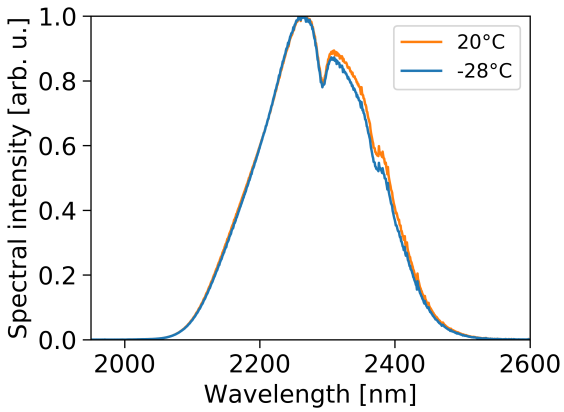

Figure 5.17: Spectra emitted by the amplifier in two temperature states.

Other quantities that should be affected by the crystal temperature are the emission and absorption cross-sections. Their shapes and magnitudes change with temperature. This is at least the case for Cr:ZnSe [163] and Ti:sapphire [164] when cooled from room temperature to the boiling point of liquid nitrogen ($\approx -196\,°C$). The amount of cooling in the present amplifier did not lead to a significant change in the spectrum, as fig. 5.17 shows. Based on the temperature-dependent fluorescence spectrum of Cr:ZnSe [163], which should be a good approximation for Cr:ZnS, it seems unlikely that Peltier-cooling, in the narrower range from a maximum of $-60\,°C$ to about $20\,°C$, can cause much larger spectral narrowing. Nevertheless caused spectral narrowing can probably be compensated with spectral broadening in the amplifier. Such spectral broadening will be demonstrated later in fig. 5.25a.

Detailed Investigation of the Output-Power Rollover

The following paragraphs describe the attempts to avoid the rollover of the output power for high pump powers. This phenomenon has already been briefly introduced on page 91. This rollover prevents the use of the amply available pump power for the realization of higher output powers. Potential causes for this effect could be an increase in core temperature, a bleaching of the crystal, a variation of the pump source, an increase in self-focusing or an increase in thermal lensing. A few experiments were carried out with the aim to clarify

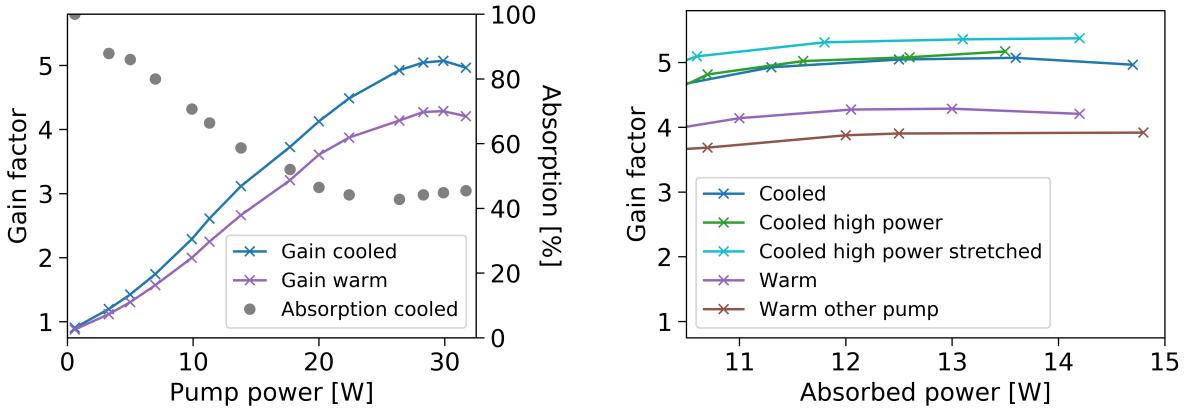

Figure 5.18: a) The gain factor of the amplifier and how it grows with the applied pump power for the two temperature states "warm" ($\approx$ 20 °C) and "cooled" ($\approx$ -28 °C), and the absorption of the "cooled" amplifier as a function of the pump power. b) The gain factor of various amplifiers plotted over the amount of absorbed pump power. The amount of absorbed power depicted here corresponds to a pump power of 26 W to 32 W in figure a). The different amplifier configurations are described in the main text.

the origin of the rollover and to prevent its occurrence. These experiments are discussed in this subsection because they involved the Peltier-cooled crystal mount. It still applies

the naming convention that "warm" corresponds to a copper temperature of about 20 °C and that "cooled" corresponds to an operation at about −28 °C.

One of the hopes of an operation at lower temperatures was that it might help to fight the mentioned rollover if this effect was caused by the heating of the crystal. Accordingly, one of the first experiments presented is the temperature influence on this matter. This influence was tested by recording the output power as a function of the pump power for the "warm" and "cooled" amplifier. The data in fig. 5.18a shows those measurements, and one can see that the stagnation for the highest pump powers is present in both configurations. Cooling the crystal to a lower core temperature could, therefore, not prevent the rollover. The gain factor is displayed in fig. 5.18a for better comparability with other measurements. Whether it is the gain factor or the output power on the y-axis does not affect the rollover.

A potential explanation of the stagnation of the curve could be the bleaching of the crystal. If the crystal stops absorbing additional pump power, then the output power is logically limited. This saturation of the pump absorption can occur due to the depletion of the ground level and due to the population of the upper energy level of the pump transition and of the laser transition. The absorbed pump power can be approximated as the difference between the applied and the transmitted pump power. This approximation neglects transmission losses like the 7 % of the ZnSe windows of the Peltier-cooled mount. However, this inaccuracy cannot explain the observed absorption of about 40 % in fig. 5.18a. Thus, the crystal is still absorbing pump power in the region of the rollover and is not yet completely bleached. This can also be seen in fig. 5.18b, where the data points of "warm" and "cooled" (and of others) are plotted over the corresponding absorbed pump power for the range of the rollover. So there is still a growing total absorption and a potential for increasing amplification.

Another suspect to cause the rollover is the pump source with its variation of waist position with chosen power, as described in fig. 5.4b on page 81. This variation can influence amplifier output - pump power measurements, like the one in fig. 5.18a, if the pump power is regulated directly at the pump laser. Two sets of data in fig. 5.18b show that this variation is not responsible for the rollover. The first data set "Cooled high power" was obtained by optimizing the amplifier explicitly for the highest pump power. This optimization was otherwise always performed at a pump power at the beginning of the rollover. The rollover occurred, however, despite the new optimization strategy. The second data set "Warm other pump" used the polarization-based pump arrangement from fig. 5.3c on page 80 to rule out pump-light variations. Also for this arrangement, a flattening of the output power was observed. Therefore, the variation of the pump source can be excluded as the cause of the rollover.

A different aspect that distinguishes the beginning of the curves in fig. 5.18a from their ends is the peak power present within the gain crystal. The rollover could, therefore, be caused by the influence of self-focusing. This hypothesis was tested by launching chirped seed pulses into the amplifier. Elongating the pulses by a factor of 4 compensates most of the increase in energy and keeps the peak power largely below the original level. This should reduce self-focusing and its influence significantly. The required dispersion was introduced with two TOD1902 mirrors and two 5 mm thick ZnSe windows. However, the

limitation in output power appeared even for those stretched pulses, as the data set "Cooled high power stretched" in fig. 5.18b shows.

In conclusion, it was not possible to overcome the rollover of output power over pump power by simple experimental means. A possible loophole regarding the absorption at high pump powers could be that the absorption could mainly take place in irrelevant parts of the beam caustic. Numerical simulations could allow one to gain a deeper understanding of the absorption reduction and of other amplifier dynamics. These simulations could potentially attribute the occurrence of the rollover to one of the amplifier dynamics, similar to the simulations for erbium-doped fiber amplifiers in reference [165, p. 12]. Another effect that could cause the rollover is the thermal lens in the amplifier [166]. This lens can cause the rollover by significantly changing the beam caustics or by degrading the beam profiles.

Gain Saturation and CW Performance

Gain saturation is an expected effect for laser amplifiers, as described on page 14. Unclear was the extent to which it would occur in the here discussed Cr:ZnS amplifiers. Knowledge of this extent is important information for the operation of the amplifier with more powerful oscillators and for the estimation of future systems. A series of measurements with different seed powers was performed to determine the gain saturation of the cold Peltier-cooled amplifier. For these measurements, the seed power was adjusted with a wire grid polarizer before the seed beam was launched into the well-performing amplifier configuration specified by the first two columns of table 5.4. Only the seed beam alignment was optimized for each seed power. Figure 5.19 shows the obtained data under the label "ML". The gain saturation is visible in fig. 5.19 as a reduction of the gain factor for growing seed power with a slope of about $-1.6\,\mathrm{W}^{-1}$. The fact that a higher gain factor can be achieved for lower seed power makes the specification of the gain factor alone an ambiguous metric for the performance of an amplifier. A more meaningful performance assessment is possible if two of the three quantities, output power, gain factor and seed power are specified.

Another general observation was that continuous-wave operation always delivered more output power than mode-locked operation. A seed-variation-study with CW seed light was made under the same conditions as before for ML light to quantify this observation. The obtained data are displayed in fig. 5.19.

The emitted beam caustic differs between CW and ML operation for Kerr-lens mode-locked oscillators. This could be a potential explanation for the difference in amplifier performance if the waist diameters in the amplifier differ much for CW and ML. Therefore, the diameters of CW and ML seed were measured to gain information on the difference in beam waist. The measured values are displayed in table 5.4. They are fairly similar, which makes it less likely that a change in beam caustic causes the difference in performance.

Also, the influence of the different temporal structures of CW and ML can be ruled out. Its influence on the obtained performance was investigated by numerical simulations on Ti:sapphire in reference [158]. In that publication, it was found that the inversion dynamic only causes a difference between CW and ML amplification for pulse repetition rates below three times the inverse of the upper-state lifetime [158]. This is certainly not the case for

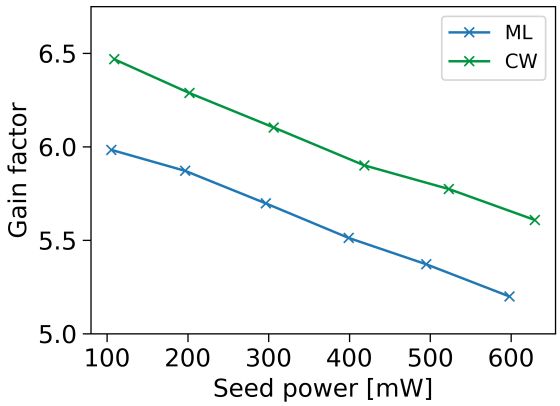

Figure 5.19: Measured gain factors for varying seed powers of mode-locked and continuous-wave radiation.

Table 5.4: Overview of the beam caustics used in the investigation. Δz specifies the longitudinal separation of the horizontal and vertical beam waist.

	Pump	ML	CW
Diameter [µm]	74 ±4	63 ±1	58 ±1
M_X^2 / M_Y^2	1.26 ±0.07	1.08 ±0.01	1.07 ±0.02
Δz [mm]	0.7	0.7	0.6

the oscillator's repetition rate of 49.9 MHz and the lifetime of about 5 µs.

A partial explanation for the difference between CW and ML operation was found in self-focusing. Preliminary data and experience from other experiments, see later subsection 5.4.6, suggest that it is possible to narrow the gap between ML and CW performance by elongating the seed pulses.

Pulse Duration Measurement

Another important aspect of the amplifier output is its compressibility to ultrashort pulses. This compressibility was already proven with FROG measurements for Cr:ZnS amplifiers at room temperature [143]. Nonetheless, it is valuable to know whether this is also true for cooled gain crystals and this particular amplifier. To prove this amplifier's ability to deliver ultrashort pulses, the output of the cooled amplifier was recompressed with chirped mirrors (CM2004) and material (sapphire) and then analyzed with a second-harmonic-generation FROG setup. The recorded experimental trace is shown in fig. 5.20a. Visually, the trace makes a time-symmetrical impression, which is a first quality indicator.

The trace was then retrieved using the program "FROG 3.2.4" from Femtosoft Technologies. The retrieved trace is displayed in fig. 5.20b. It shows a good agreement with the recorded trace and exhibits a FROG-error of 0.00185 on a grid of 256 points. Another feature that makes the measurement trustworthy is the agreement between measured and retrieved spectrum in fig. 5.20c. The flatness of the spectral phase over the spectral range indicates a good recompression of the pulse. The border areas reveal the presence of residual third-order dispersion, which is the next higher order of spectral phase after GDD. According to the retrieval, the pulse has a FWHM duration of 47 fs. The Fourier-transform-limited pulse duration, as shown in fig. 5.20d, is 43 fs.

This experiment is a proof of principle and did not strive for the shortest possible pulses. Especially since the oscillator spectrum at this point (fig. 5.20c) was narrower than usual, compare, for example, with fig. 5.17 on page 97. If one is really after the shortest possible pulses, then one would try to drive spectral broadening in the amplifier and might utilize specially designed dispersive mirrors to straighten the spectral phase even more. The cooled amplifier operated as expected and delivered a gain factor of about 5 in this experiment.

Thus, it was demonstrated that the amplification process in the cooled crystal does not cause unexpected spectral phase distortions and that the ZnSe windows and the other optical components in the beam path can be compensated.

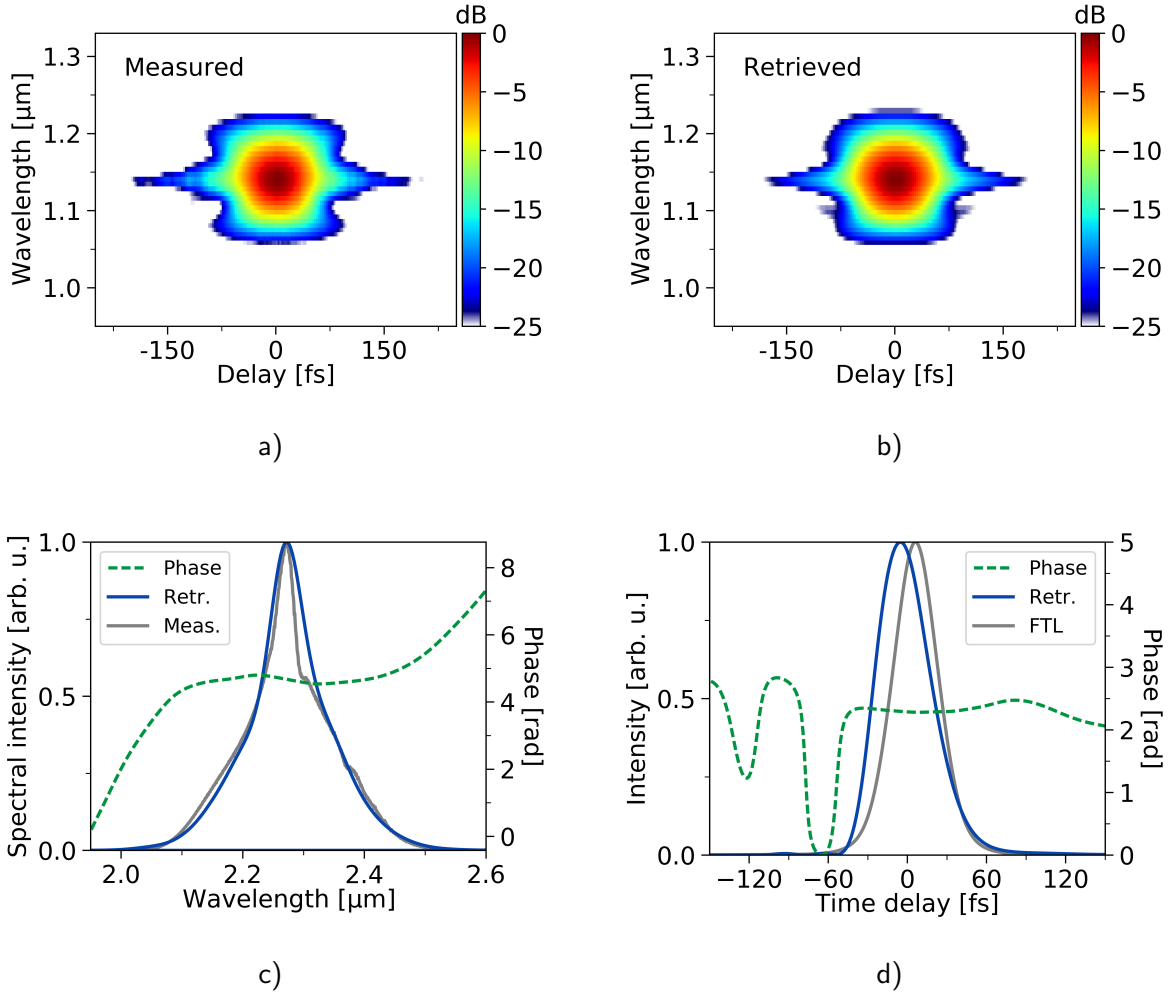

Figure 5.20: a) Measured FROG trace. b) Retrieved FROG trace. c) Comparison of the spectrum measured with a spectrometer and the spectrum found by the FROG trace retrieval. The retrieved spectral phase is also displayed. d) Comparison of the retrieved temporal pulse shape and phase with its Fourier-transform-limited version.

Pump-Noise Transfer

In the previous subsection on page 91, the potential for saturating the pump-noise transfer for a warm amplifier was investigated. An alternative possibility that could dampen the transfer is the lengthening of the upper-state lifetime, which can be achieved in the cooled amplifier. The idea behind this possibility is as follows. The upper-state lifetime defines the shortest time after which a substantial reduction in population inversion due to spontaneous emission occurred. Therefore, the inversion cannot fully follow intensity modulations of the pump light, if the significant modulation occurs on a shorter time scale than the lifetime and if spontaneous emission is a major excitation sink. This mechanism should be equivalent to a dampened pump-noise transfer into the population inversion. A longer lifetime should shift the onset of this mechanism to lower frequencies and the hope was to see this effect in the output of the amplifier. The intensity noise of the Peltier-cooled amplifier was measured for the warm and cooled state to check the presence of this effect. In this experiment, the amplifier was seeded with about 730 mW and delivered an output power of 3.13 W in the warm state and an output power of 3.68 W in the cold state. A set of the obtained data is shown in fig. 5.21. It can be seen in fig. 5.21 that the change in crystal temperature did not substantially alter the distribution and amplitude of the intensity noise.

The computation of the integrated $\mathrm{RIN_{rms}}$ for the spectral band from 100 Hz to 1 MHz resulted in a value of 0.054 % for the oscillator, a value of 0.102 % for the warm amplifier and a value of 0.116 % for the cooled amplifier. Cooling down the gain crystal did not improve the intensity noise. Therefore, both single-pass amplifiers roughly double the relative intensity noise of the pulse train, while they increase the optical power by a factor of about 4 or 5.

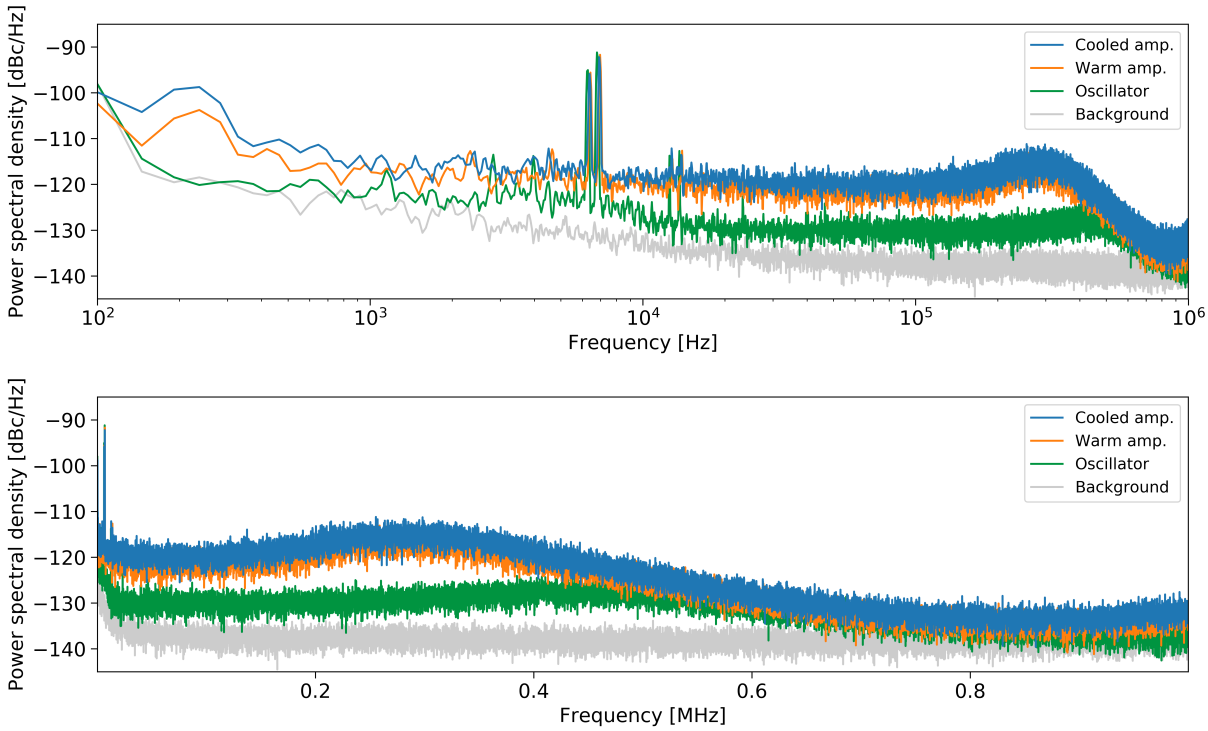

Figure 5.21: Investigation of the influence of the cooling temperature on the intensity noise. Both graphs depict the measured and accordingly normalized spectral power over frequency. The upper graph presents the data on a logarithmic frequency scale, the lower graph on a linear frequency scale. The electrical power delivered by the photodiode was used as the respective reference level. The background measurement describes the noise floor of the entire measurement chain.

5.4.5 Alternative Scaling Concepts for Single Stage Amplifiers

In the previous subsection, it was possible to obtain gain factors in the range of 4 to 5 and output powers of over 3 W from a single 9 mm Cr:ZnS amplifier stage. This is a first step towards the targeted power levels. The question then arose whether it is possible to amplify even more in a single amplifier stage. This question was addressed with attempts to realize more sophisticated amplifier arrangements with more than one pass through the amplifier crystal. This subsection reports on such double-pass amplifiers and their performance.

The first design under investigation mimicked the classical "bow tie" multipass amplifier scheme. In this design, the amplified seed beam was redirected with a retroreflecting hollow roof prism mirror and was focused into the crystal again. A schematic of this amplifier can be seen in fig. 5.22a. The schematic illustrates that the seed beams cross each other

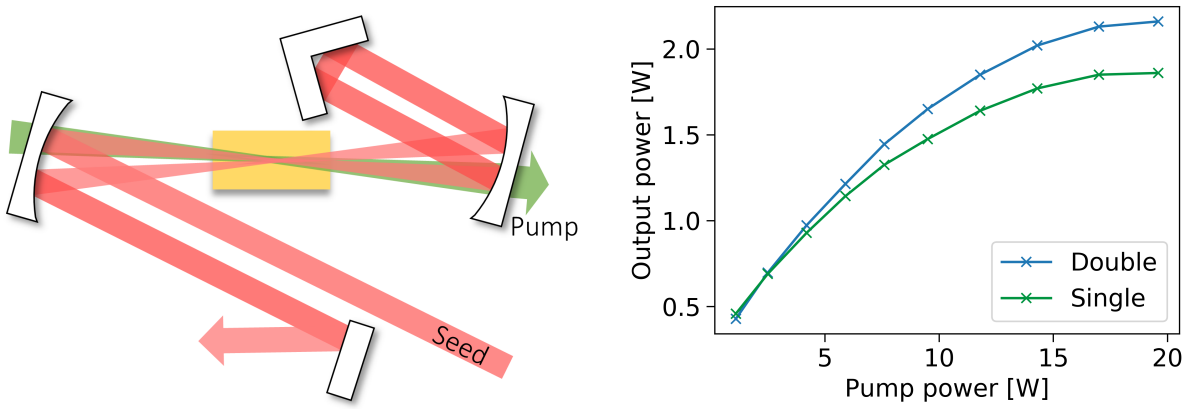

Figure 5.22: a) Schematic of the double-pass amplifier with geometric beam separation. After the first pass through the amplifier, the beam gets reflected back into the amplifier. There, it crosses the pumped region for additional gain and is then separated from the incoming beam with a pick-off mirror. b) The graph displays the obtained output power over the applied pump power. Data is shown for the double-pass amplifier with geometric beam separation and for the single-pass amplifier obtained by removing the retroreflecting hollow roof prism mirror.

in the gain volume. Accordingly, the overlap between the seed beam-caustics and pump beam-caustic cannot be as ideal as in the single-pass case. The optimization of this overlap would certainly be interesting and could be investigated in future studies. However, in this series of experiments, the pump beam and the first seed pass were aligned for optimal overlap and the second seed beam simply crossed the gain volume. This type of a second pass through the crystal will be called "geometric double pass" since the separation of the incoming and emitted beam is achieved purely with geometric means. The amplifier had a seed diameter of 67 µm and a pump diameter of 61 µm. The seed oscillator for these experiments was "Miranda 1". Accordingly, only a seed power of about 330 mW was available for the experiments. A direct comparison between the geometric double pass and

its simple single-pass version can be seen in fig. 5.22b, which displays the obtained output power over the applied pump power. Each of the "double pass"-data points was adjusted for minimal still tolerable beam separation. With too little separation, feedback into the oscillator stopped mode-locked operation. On the other hand, too much separation led to a reduction in performance. It can be seen that an output power of 2.16 W was obtained for the double pass and an output power of 1.86 W for the single-pass amplifier in the same configuration. This is an improvement of about 16 %. However, the emitted beam had an elliptical shape due to the angles of incidence on the curved mirrors.

A second, refined investigation of the geometric double pass was performed with "Miranda 2" as the front-end. The biggest conceptual change in this second version was the presence of a Brewster plate to compensate the astigmatism introduced by the angles of incidence on the curved mirrors. This required to rotate the polarization of the seed light with a half-wave plate to *p*-polarization to reduce reflection losses. A 5 mm thick CaF_2 window was chosen as the Brewster plate, because it has a rather low negative dispersion of $-40\,\mathrm{fs}^2\,\mathrm{mm}^{-1}$ at a wavelength of 2.3 µm and a relatively small Brewster's angle of 55° [167, 168]. The amplifier was seeded with about 640 mW. The seed diameter was 63 µm and the pump diameter was 72 µm. The amplification was performed with an additional distance of 50 µm to the crystal bottom in order to have more alignment tolerance for the second pass. The second pass was able to increase the output power from 2.35 W to 2.55 W. The same experiment was repeated for an enlarged gain volume to test if this benefits the second pass. The larger gain volume was created by a pump waist-diameter of 112 µm. For this configuration, an increase in output power from 2.25 W to 2.55 W was observed. Neither the Brewster plate nor the enlarged gain volume led to a major performance improvement. Both modifications fell short of expectations. The implemented geometric double passes boosted the output power by a maximum of 16%.

A different approach for the realization of the second pass was tested too. This approach made use of the polarization of the seed beam to separate the backward propagating seed beam from the forward propagating seed beam. This separation can be realized by inserting a polarizer and a quarter-wave plate before the amplifier crystal and by reflecting the seed beam back through the amplifier. The polarizer then separates the back-reflected beam from the incoming beam if the wave plate is oriented correctly. The schematic of this arrangement can be seen in fig. 5.23a. Only the seed beam passes through the crystal twice. The pump beam is removed after the first pass to protect the pump source from potentially harmful feedback. The diameters of seed and pump were 67 µm and 61 µm in this arrangement. As the schematic indicates, a slight offset between the forward and backward propagating seed beam was required in the experimental realization. This was necessary because the wire grid polarizer (WP25M-UB, Thorlabs GmbH) in combination with the quarter-wave plate (superachromatic, B.Halle Nachfl. GmbH) was not able to suppress feedback into the oscillator sufficiently. More separation was required with growing output power. The achieved performance is documented in fig. 5.23b. The data points called "Double" represent the highest performance achieved for the lowest tolerable separation in the double-pass amplifier. The graph shows an initially steep slope for the double-pass configuration until the point where the output power requires such large separations that

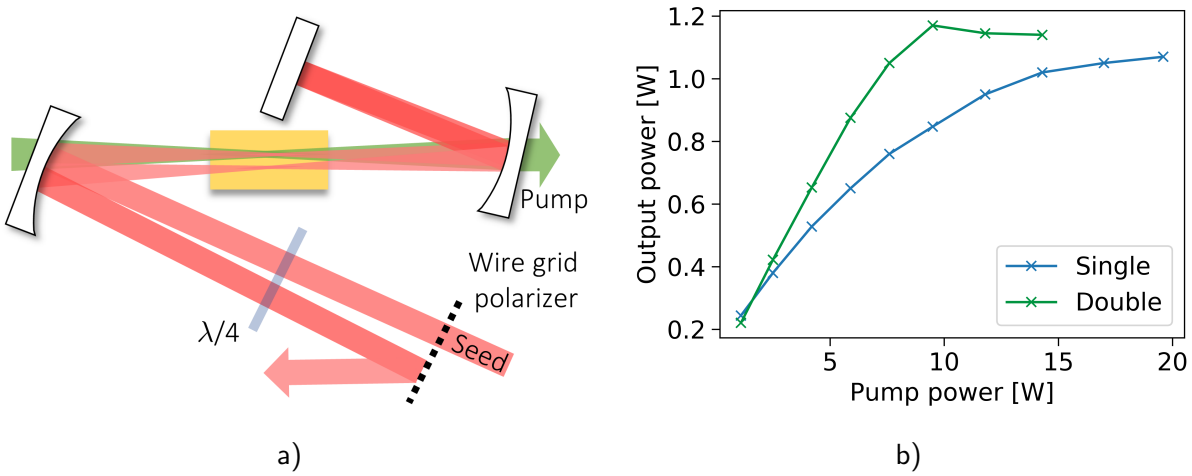

a) b)

Figure 5.23: a) Schematic of the polarization-based double-pass amplifier. The back-reflected beam of the second pass needs a little additional spatial separation to suppress feedback into the oscillator. The beam separation in the crystal is exaggerated in this illustration. b) The achievable output power at different applied pump powers. Data for a single pass through the arrangement and for the complete double-pass amplifier are displayed.

the advantage of the second pass fades away. At its peak, the double pass performed about one-third better than the single-pass configuration for the same pump power. This demonstrates the great potential which polarization-based double-pass or multipass amplifiers have if they can operate with almost perfect seed-pump overlap. The seed power for the experiments in fig. 5.23b was only about 205 mW, which explains their low output power level. The seed power was so low in this experiment because "Miranda 1" was used and because of the losses at the polarization optics.

Also, for the polarization-based approach, a follow-up experiment was executed. This time, an arrangement consisting only of a polarizer, a quarter-wave plate and an end mirror was set up as the most basic arrangement to minimize the number of parameters. As the wire grid polarizer failed to suppress feedback into the oscillator, another type of polarizer with an even higher extinction ratio (>100 000:1) was used. This polarizer was a 20° Wollaston prism (WPA10, Thorlabs GmbH), which required the input beam to have an angle of incidence of 10° on the polarizer. The arrangement was optimized for maximum transmission into the orthogonal polarization state with a slightly detuned end mirror. Next, the end mirror was aligned for back reflection along the incident beam path. This proper alignment then caused a loss of mode-locked operation for all tested configurations. Therefore, no second polarization-based double-pass amplifier was realized. The oscillator used was "Miranda 2". The reason for the inability to suppress feedback is not known. However, the result of this second experiment with an even better polarizer suggests that the action of the wave plate is not uniform enough over the involved spectral bandwidth. Good news for future implementations of polarization-based multipass amplifiers is that recently broadband optical isolators for a wavelength of 2.3 µm (MESOS broadband iso-

lators, Electro-Optics Technology Inc.) have become commercially available. To what extent their material dispersion can be handled remains to be seen, but their availability will probably enable more advanced polarization-based multipass amplifiers. A few such amplifier schemes can be found in these references [169–171, p. 13].

5.4.6 Power Scaling with Multiple Amplifier Stages

Output powers in the range of 2.9 W to 3.8 W were demonstrated in the previous subsections for a single-pass amplifier stage pumped at a wavelength of 1908 nm. Apart from the intended performance variations due to the crystal temperature and the diameters, the performance was modified by varying seed-power levels and the spatially varying doping concentration of the gain crystal. The input coupler used in the design had a radius of curvature of 200 mm and the focusing lens of the pump beam had a focal length of 150 mm. In a typical case, such a single water-cooled amplifier stage delivered an output power of about 3.3 W for a seed power of about 730 mW. This performance can be obtained by pumping with a pump power of about 26 W, of which about 13 W are transmitted through the crystal as residual pump light.

This large amount of residual pump light, which propagates collinearly with the seed, can be used for further amplification. This further use can be made possible by forming an image of the pump and seed waist, either with a 4f-telescope or with a single lens and the appropriate imaging distances. In this way, one can build a second amplifier without much effort, simply by placing another gain crystal in the newly generated second focus. This implementation of additional amplifier stages is a less elaborated scaling approach than those attempted in the previous subsection 5.4.5, but it turned out to be an effective one, as will be shown on the following pages.

For this second amplifier stage, only a few parameters are adjustable. Those parameters are the position parameters of the second gain crystal and the diameters of the second foci. The latter scale collectively and were not investigated in this series of experiments. Therefore, the z and height position of the gain crystal were the main tuning parameters. The gain crystal used was specified with a transmission of 5.3 % for a wavelength of 1560 nm through its length of 9 mm, and thus had very similar properties to the crystal in the first amplifier stage. This transmission corresponds to about 17 % for a wavelength of 1908 nm. The pump and seed waist were imaged into this crystal with a 4f-telescope based on two focusing lenses with a focal length of 75 mm each. The first of those lenses was an achromatic doublet and the second was a plano-convex spherical lens, as these were the best lenses at hand.

The amplifier chain in its first implementation generated much visible light in the second amplifier crystal. An impression of this can be gained in fig. 5.24. This happened because the polycrystalline Cr:ZnS has high $\chi^{(2)}$ and $\chi^{(3)}$ nonlinearities and features random quasi-phase-matching. Therefore, a number of nonlinear effects take place in the crystal and generate harmonics of the fundamental spectrum, if high intensities are reached in the crystal [155]. In this first implementation, the usage of the second amplifier increased the output power by about 1.6 W for mode-locked operation. However, for continuous-wave

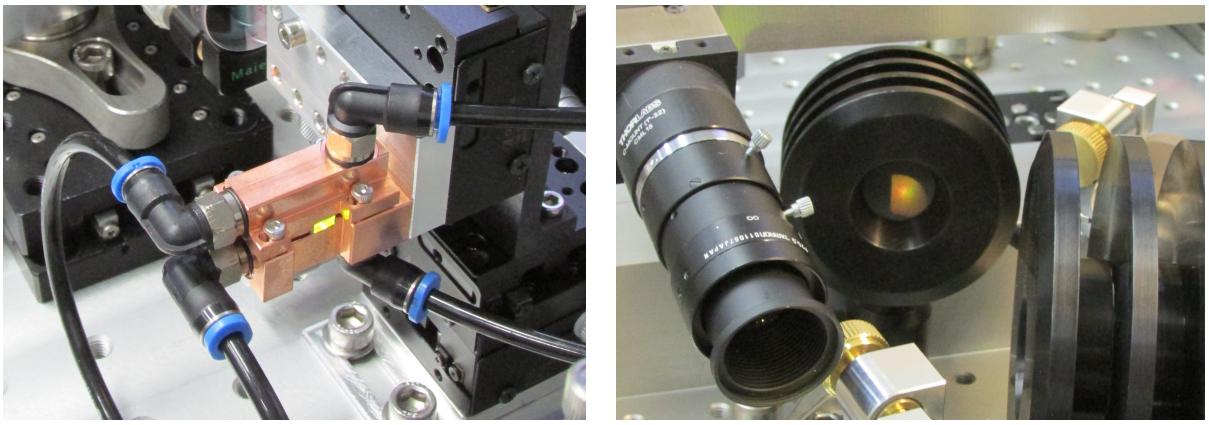

a) b)

Figure 5.24: a) The luminous gain crystal of the second amplifier stage in its copper mount. In the first iterations of the second amplifier, the seed beam generated much more visible light than in the first amplifier stage. b) A picture of the power sensor of the second stage. The visible light generated in the gain crystal illuminates a part of the sensor area in yellow, orange and green.

operation, the additional output power was twice as high. Moreover, the ideal crystal position in z-direction was quite different for ML and CW operation. Together, these observations suggest that nonlinear processes are rather strong in the second stage. This is not surprising, given the higher power level in the second stage. Moreover, a calculation of the involved dispersion indicated that the pulses were temporally compressed as they propagated through the second gain crystal. This recompression was not intended, but the material of the relay-imaging arrangement balanced by chance the dispersion introduced by both gain crystals and led to even higher peak powers in the second crystal. Therefore, the idea for improvement was to make the seed pulses more CW-like. This could be achieved by stretching the seed pulses in time with material dispersion. For this purpose, AR-coated ZnSe windows that are 5 mm thick were inserted into the relay-imaging arrangement. Adding the first window allowed to achieve 0.5 W more output power while simultaneously obtaining 0.6 W more transmitted pump power. This simultaneous improvement was possible because the optimal z-position was different from before. The optimum was now 2.6 mm further in the direction that previously yielded more visible light but less power. When adding the second plate, a similar behavior was observed, with a gain in output power of another 0.7 W and an additionally transmitted pump power of 0.8 W. So it seems that the optimal crystal position was shifted behind the pump focus by the self-focusing of the recompressed pulses and that the pulse stretching brought the optimal crystal position closer to the pump-beam waist. In this way, the pump intensities become higher and the percentage absorption becomes lower, resulting in an increase in transmitted power. The simultaneously improving overlap of the seed caustic with the pump caustic explains the improved performance of the operation with reduced self-focusing. The optimization was

then continued by removing detrimental back-reflections into the oscillator stemming from the imaging lenses, by adjusting the crystal position in z and height, and by pumping harder. In the end, this pushed the obtained output power to about 7.4 W.

Another indication for the presence of nonlinearity was found in the modifications that the emitted spectrum exhibited at different pump power levels even after the addition of the two dispersive windows. For increasing pump and output power, an increase in spectral width was observed, which then also developed a pronounced intensity suppression in the middle part of the spectrum. This is a typical feature of spectral broadening by self-phase modulation. This evolution is exemplified in fig. 5.25a with three lines for low, medium and high average power. The transition between these lines is continuous. This observation of spectral broadening confirms previous reports that gain narrowing can be overcome in this material [46, 143]. The spectra in fig. 5.25 were smoothened during evaluation with a moving average to remove artifacts, which were introduced by the spectrometer's multimode fiber.

The same measurement was repeated with three dispersive plates in the imaging arrangement. This amplifier followed the same spectral evolution as the amplifier with two plates. It only showed a less pronounced spectral broadening, as can be seen by comparing fig. 5.25b with fig. 5.25a. This is due to the desired additional pulse stretching, the corresponding reduction in peak power and the dependence of the spectral broadening on peak power (eq. (2.52)). The third plate improved the output power of this amplifier by only about 0.2 W for high pump powers.

The spectra in fig. 5.25b show a slight dip around the dashed line at 1908 nm. This dip is an artifact caused by the background subtraction and a tiny amount of still copropagating pump light. This pump light is not noticed in power measurements, but spectrometers can sense its presence. The dashed line illustrates the spectral proximity between pump and seed light. This proximity can become a limiting factor for the amount of useful spectral broadening in the amplifier, because the dichroic mirror for the separation of pump and seed will truncate and temporally distort the blue wing of the generated seed spectrum.

Another aspect is that the SPM-driven spectral broadening comes along with self-focusing, which in turn affects the spatial beam quality. It is, therefore, necessary to make a tradeoff between spectral broadening, beam quality and, to some extent, output power. A similar tradeoff between amplification and nonlinear processes is reflected in literature, as can be seen from the reduction in power between reference [36] and [155] of table 5.2. Some stretching of the pulses will almost certainly be used in future amplifiers because it resulted in much better power performance.

Stretching the seed pulses before the first amplifier should result in the best performance, because gain and losses can be regarded as multiplicative factors. Therefore, their sequence does not matter in first approximation. In fact, however, the gain factors will be slightly higher if the stretching is performed before the first amplifier. That is the case due to a reduced gain saturation and a reduced nonlinearity in the first stage, and a reduced pump loss for the second amplifier. The gain saturation will be lower because the initial seed power will be lower by introducing the dispersion before the first amplifier. Nevertheless, this dispersion should be introduced with the lowest possible seed-power losses.

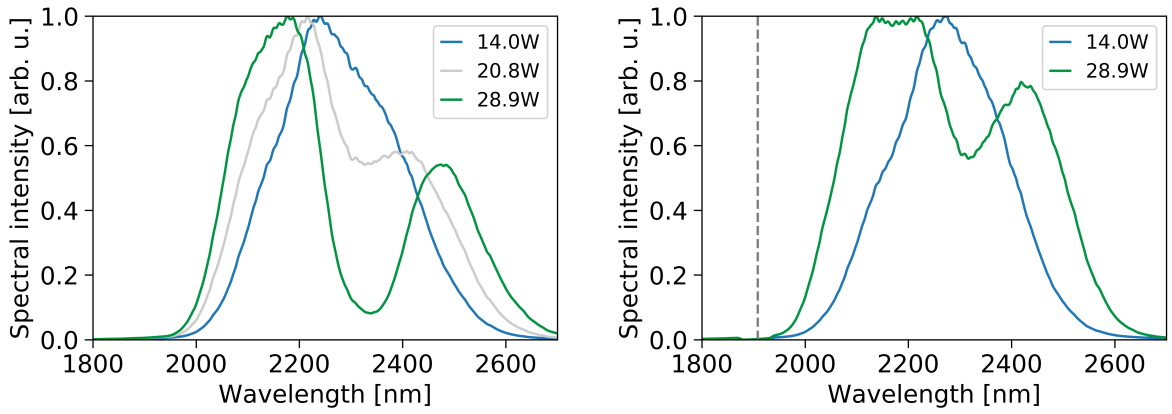

Figure 5.25: Spectra emitted by the dual stage amplifier at different pump power levels. a) Series of spectra with two stretcher windows between the amplifiers. The blue line corresponds to an output power of about 4.3 W, the gray line to about 6.3 W and the green line to about 7.9 W. b) Two spectra recorded for three stretcher windows between the amplifiers. The blue line corresponds to an output power of about 4.3 W and the green line to about 8.1 W. The gray dashed line indicates the pump wavelength.

The amplifier with three material plates was characterized further in terms of beam quality. The shape of the obtained transverse intensity profile depends on the overlap between seed and pump and can be tuned for maximal symmetry or maximal output power. The existence of these two distinct states could be an indication of imperfect amplifier alignment. The beam profile displayed in fig. 5.26a was optimized for maximal symmetry and was thus recorded for an output power of 6.9 W. The cross section shown at the bottom of the image was, for example, affected by the horizontal seed beam alignment. The M^2-value was determined for an output power of 7.1 W with a slightly (50 µm) relaxed height setting in the first amplifier stage. The M^2-value was found to be 1.16 in the horizontal direction and 1.10 in the vertical direction for a central wavelength of 2274 nm. The measured data and their evaluations can be seen in fig. 5.26b. The observed astigmatism should come from the angles of incidence on the concave input couplers. For the later application, one can reduce this astigmatism with Brewster plates or cylindrical mirrors.

In conclusion, the amplifier tandem can deliver an output power of about 7.7 W. There is still a residual pump power of about 4 W after the second stage, but this is probably too little pump power for a third stage, given that stage one and two had a pump power of 26 W and 13 W available. An option would have been to increase the initial pump power further, but it was unclear how much power the first crystal can withstand without damage. Thus, a second pump branch was built so that the output of the second stage could be combined with a new beam of pump light for amplification in a third crystal.

As said, the third amplifier stage was seeded by the output of stage one and two, which typically emitted a power of about 7.7 W at that time. The seed pulses were delivered to

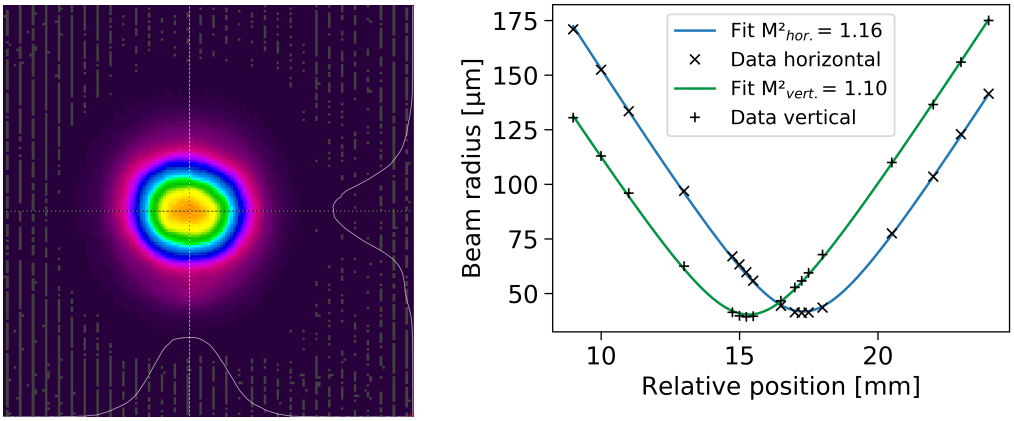

a) b)

Figure 5.26: a) Transverse intensity beam profile emitted by the dual stage amplifier. Cross sections of the profile along the dotted lines are displayed at the right and lower margin. The profile was recorded with a pyroelectric array camera. b) M^2-measurement of the dual stage amplifier emission. The graph displays the measured beam radii and the fitted beam-width evolution for the horizontal and vertical plane. The obtained M^2-values are 1.16 and 1.10, respectively.

the third stage as a roughly collimated beam. On their way, the seed pulses were stretched further in order to prevent potential damages due to the otherwise growing peak power. For this purpose, two TOD1902 mirrors with about 1000 fs^2 and one 5 mm thick ZnSe window with about 1250 fs^2 were inserted into the beam path. The seed beam was then combined with the new pump beam using an input coupler with a ROC of 200 mm. The resulting seed waist diameter was estimated to be about 55 µm in low power operation. This third amplifier stage was typically able to increase the output power to 13.6 W by applying a pump power of 29.6 W. The crystal used had a length of 9.0 mm. It was specified with a transmission of 15.7 % for a wavelength of 1908 nm. The amount of transmitted pump light was about 14 W during amplification. The amplifier was characterized for an output power of 13.3 W. The corresponding beam profile is displayed in fig. 5.27a. It shows no severe signs of distortion. The M^2-values were measured to be 1.50 and 1.47 for a central wavelength of 2270 nm. Their evaluations can be seen in fig. 5.27b.

The residual pump power of about 14 W after the third stage suggested the realization of a fourth stage. This time, the foci were imaged with only one single lens with a focal length of 100 mm, since it better suited the spatial constraints. Two more 5 mm thick ZnSe windows were added into this imaging arrangement in order to keep stretching the pulses as their energy grows. The crystal of the fourth amplifier stage was only 5.1 mm long because a longer crystal was not available at that time. The crystal was specified with a transmission of 10 % at a wavelength of 1560 nm through its length and showed no height dependence. The absence of the usual height dependence in this crystal is an argument against improved cooling as the cause of the height dependence. This fourth

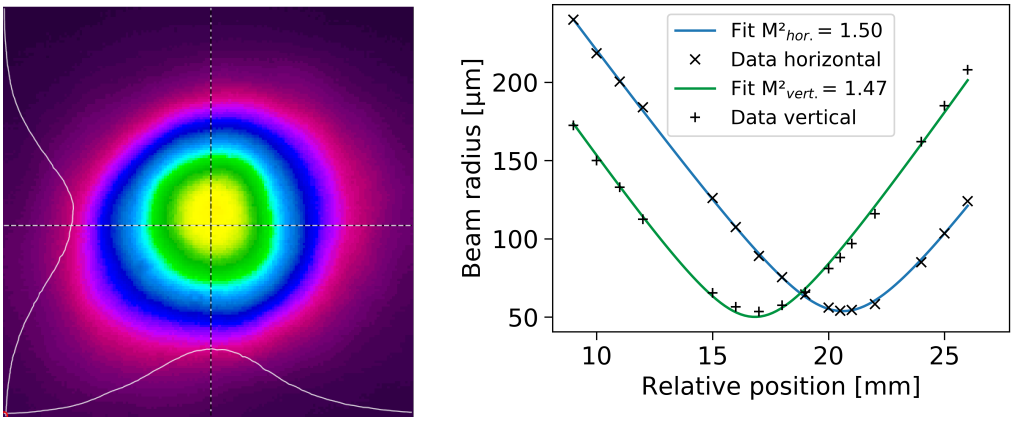

a) b)

Figure 5.27: a) Transverse intensity beam profile recorded for the triple stage amplifier. Cuts through the profile along the dashed lines are displayed at the left and lower margin. The profile was recorded with a pyroelectric array camera. b) M^2-measurement of the emitted beam of the triple stage amplifier. Displayed are the measured radii and the fitted beam-width evolutions. The data was taken with a scanning slit beam profiler. The computed M^2-value in the horizontal plane is 1.50 and 1.47 in the vertical plane.

amplifier increased the output power of the amplifier chain to 16.6 W while being seeded with 13.6 W. The residual pump power after this amplifier was about 6W. The amplifier chain was characterized for this output power of 16.6 W. The recorded beam profile can be seen in fig. 5.28a. The M^2-measurements are shown in fig. 5.28b. For a central wavelength of 2257 nm, the M^2-values were determined to be 1.37 each.

The M^2-values presented in this subsection are intended as evidence that there is no severe beam quality degradation due to the high average power level. They can be further optimized and their exact value will probably depend on the exact implementation of the amplifier. The M^2-values will, for example, depend on the quality of the relay-imaging and the chosen amount of nonlinearity.

Each of the amplifier stages contributed a few watts to the power of the seed beam, as summarized in table 5.5. This approach can be pursued as long as one manages the nonlinearity within the gain crystals. The limit will then be set by the balance between percentage losses like reflection losses and the gained power per stage. The sub-20 W range became accessible with a reasonable effort via the presented multi-stage approach. The demonstrated average power of more than 16 W corresponds to a gain factor of about 22, which is a high value for an amplifier system at full repetition rate. The expected compressibility of the pulses to a duration of about 40 fs makes this system a competitive 2 µm source.

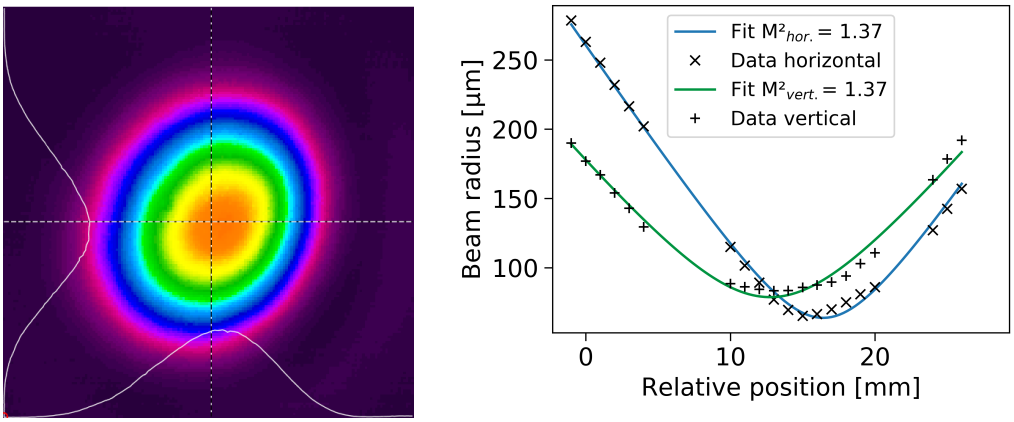

a) b)

Figure 5.28: a) Transverse intensity beam profile emitted by the amplifier with four amplification stages. Cuts through the profile along the dashed lines are displayed at the left and lower margin. The recording was taken with a pyroelectric array camera. b) M^2-characterization of the four-stage amplifier. The graph displays the measured beam radii and the fitted beam-width evolution for the horizontal and vertical plane. Both axes resulted in an M^2-value of 1.37.

Table 5.5: Multi-stage amplifier overview. The seed diameter of the 1st stage was 62 µm. The seed diameter is only specified for the 1st stage because the values of the subsequent stages in operation will certainly deviate from the measurements at low power due to effects like thermal lensing. The same argument applies to the pump diameters that are not specified.

	1st Stage	2nd Stage	3rd Stage	4th Stage
Crystal length [mm]	9.0	9.0	9.0	5.1
Diameter pump [µm]	70	–	68	–
Pump power [W]	26	13	29.6	14
Transmitted power [W]	13	4	14	6
Absorbed power [W]	13	9	15.6	8
Seed power [W]	0.73	3.3	7.7	13.6
Output power [W]	3.3	7.7	13.6	16.6
Added power [W]	2.6	4.4	5.9	3.0
Gain factor	4.52	2.33	1.77	1.22
M_X^2 / M_Y^2	1.16 / 1.16	1.16 / 1.10	1.50 / 1.47	1.37 / 1.37

5.4.7 Higher Doped Gain Crystals

This subsection is motivated by the repeatedly made observation that the amplifier performance seems to correlate positively with the doping concentration. Accordingly, higher doped gain crystals were obtained to investigate this further. This subsection reports on the comparison of such a crystal with a normal doped crystal in an identical amplifier configuration. In this amplifier configuration, the seed and pump diameters were about 65 µm and the seed power was about 728 mW. The higher doped crystal under investigation was specified to have a transmission of 5.3 % through its length of 8.9 mm for a wavelength of 1908 nm. The normal doped crystal was already used in previous experiments and was specified to have a transmission of 5.3 % through its length of 9.0 mm for a wavelength of 1560 nm. This corresponds to a transmission of about 17 % for a wavelength of 1908 nm, according to the crystal's spectrally resolved transmission report by IPG Photonics. In the following, these crystals are identified by their doping degree as highly and normally doped.

The observed height dependence of the pump light transmission of these crystals is shown in fig. 5.29a. If one compares these transmission curves, then one finds a much lower and much more uniform transmission for the highly doped crystal. In the crystal with normal doping, a pronounced gradient in transmission is present and the measured transmission values are, as expected, higher. The transmission values were recorded as described before on page 88. The measurement was performed with a pump power of 60.8 mW for the highly doped crystal and with a pump power of 28.5 mW for the normally doped crystal. The dip in the transmission measurement of the normal crystal at about 0.5 mm was caused by a damage at the front surface. This damage occurred during powerful amplifier operation, as will be described later. Such damages originate most likely from local material weaknesses, like a weak crystal grain or a defect in the AR-coating. High pump powers can turn such weak points into damages. The values of the normal crystal are also presented in fig. 5.11.

In a second measurement, the spatial dependence of the amplifier performance was determined according to the procedure described on page 89. The obtained height dependence is displayed in fig. 5.29b. The observed gain evolutions are essentially the inversions of the transmission measurements because less transmitted pump light means more absorbed energy with more potential for amplification. Accordingly, the two crystals showed again quite different behaviors. The performance of the normally doped crystal exhibits a large variation over the height of the crystal and is rather modest for most of the crystal. This is in good agreement with the inversion of its transmission behavior. Its performance measurement was interrupted in the second half due to the occurrence of the crystal damage.

The performance of the highly doped crystal reflects the low, uniform value of its pump light transmission by delivering a high, nearly position-independent gain. The amplification is, in general, higher in the highly doped crystal. The highly doped crystal was able to deliver a bit more output power than 3.9 W for a seed power of 0.73 W and a pump power of 31 W. This is about 34 % more output power than the normal crystal can deliver.

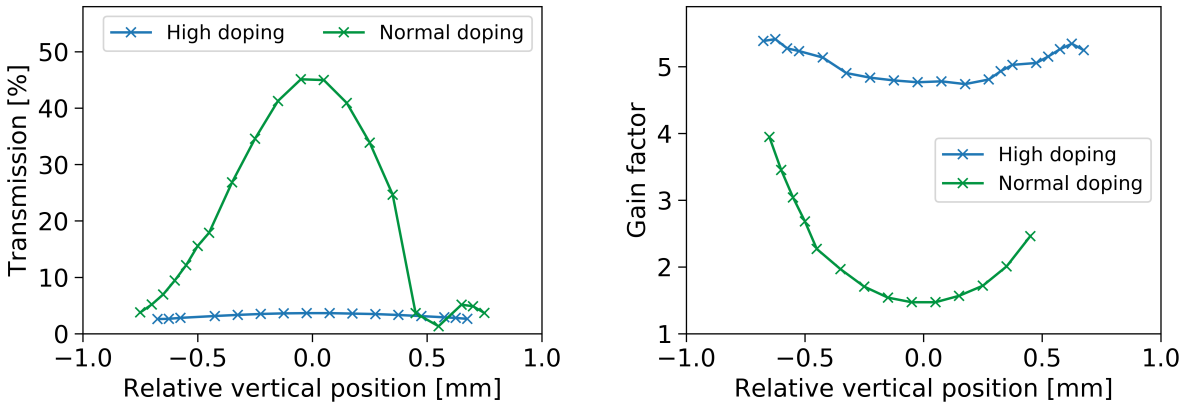

Figure 5.29: a) Spatial dependence of the pump light transmission of a highly doped crystal and a normally doped crystal. The displayed values are a good approximation of the small-signal transmission. The rapid change of the green line around 0.5 mm was caused by a damage at the front surface. The investigated crystals had a height of about 2 mm. b) Spatially resolved gain-factor measurements associated with the measurements in fig. a). The measurement of the normal crystal was aborted after the occurrence of the damage at about 0.5 mm.

Moreover, the nearly position-independent gain of the highly doped crystal makes future systems more reliable by not depending on one particular position. Further, it removes the need to locate the beams only a few 10s of µm from the crystal's edge. This reduces the risk of hitting the surrounding indium by alignment drifts or accidental alignment changes. The transmission, at a pump power of 31 W and with the presence of seed light, was about 42 %. The corresponding transmitted pump power of 13 W is comparable to the powers used in subsection 5.4.6 and should, therefore, allow the operation of a subsequent amplifier stage.

The doping and transmission inhomogeneity of the highly doped crystal also showed a horizontal dependence. This is exemplified in fig. 5.30a. This inhomogeneity gives access to transmission values below and above the actual crystal specification. The measurement from fig. 5.29a corresponds to the vertical measurement in fig. 5.30a. The measurement from fig. 5.29a did not surpass the specified transmission of 5.3 % due to its horizontal position at the edge of the crystal. The reported performance of 3.9 W was obtained in a corner of the crystal with a small-signal transmission of about 2.6 %. This suggests that crystals with an average transmission of 5 % are not the end of the doping optimization. Even higher doping concentrations should be beneficial for amplification with pump light at 1908 nm.

The transverse intensity profile, depicted in fig. 5.30b, shows no serious beam degradation despite the further increased thermal load in the higher doped crystal.

The output power of the highly doped amplifier was recorded for 100 minutes to get an impression of the long-term stability. The recording in fig. 5.31 shows a good stability

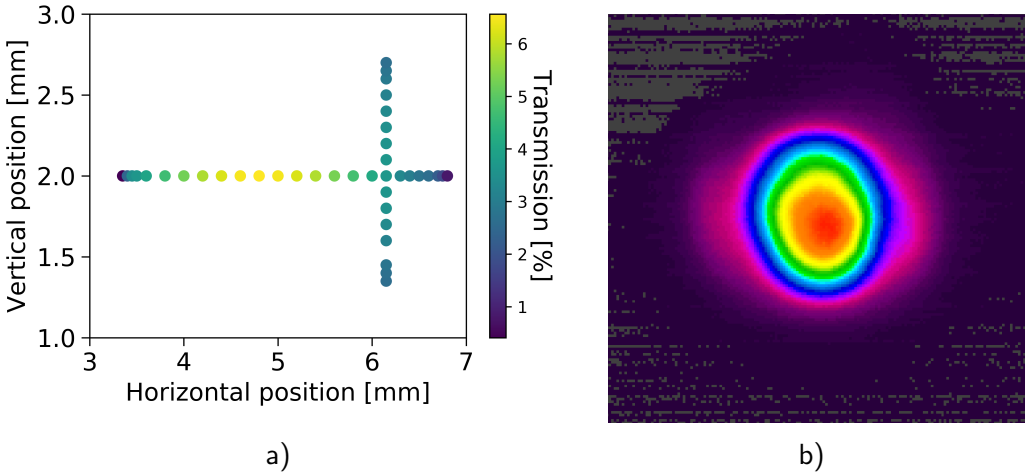

Figure 5.30: a) Pump-light transmission through the highly doped crystal. The measurement is spatially resolved in the transverse plane. In this plane, the crystal was 4.0 mm wide and 2.0 mm high. b) Transverse intensity profile of the single-stage amplifier equipped with the highly doped gain crystal. The amplifier was operating at an output power of 3.9 W during this recording. The beam profile was recorded with a pyroelectric array camera, which was placed behind two output couplers and some neutral density filters for beam attenuation.

of the thermalized system without any further drifting. The minor fluctuations of this amplifier give hope for the performance of the amplifier chain.

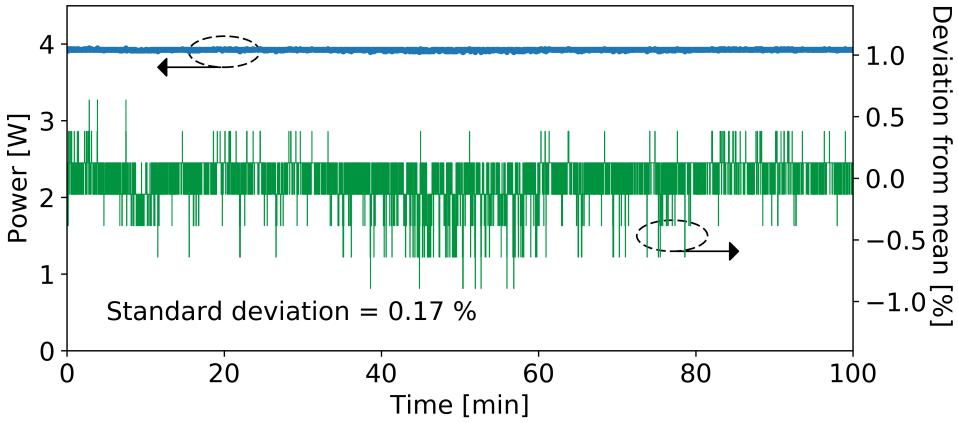

Figure 5.31: Long-term power recording of the highly doped amplifier. The blue line shows the measured power over time. The green line shows the percentage deviation from the mean power.

The highly doped crystal used in this subsection was available for experiments only at the very end of the experimental phase. Accordingly, there are many new, exciting questions to be answered in the future.

5.5 Chapter Summary and Outlook

In this chapter, various approaches to improve the performance of Cr:ZnS amplifiers were investigated. Thulium-based pump lasers were used throughout the experiments, and it was found that a pump wavelength of 1908 nm, as compared to the more common 1946 nm, is beneficial due to the more favorable ratio between the absorption and emission cross-section of Cr:ZnS at this wavelength.

Optimizing the design of the single-pass amplifiers has improved the performance of these amplifiers. Their gain factor was further increased by realizing the first Cr:ZnS amplifier at sub-0 °C temperatures. Cooling the gain crystal to about −30 °C led to about 19 % more output power. The extent of gain saturation, which is important information for assessing the potential of the amplifier stage, was also measured and amounts to a reduction in gain of 1.6 per watt of seed power.

The pronounced influence of the doping concentration on the amplifier performance suggested the use of a more highly doped crystal, which led to a very promising power improvement of about 34 %. The presence of high doping concentrations already in the center of the crystal is very beneficial in general because this allows more fault-proof amplifier systems by relaxing the need to operate at the edges of the crystal.

In all amplifiers, a rollover of output power with respect to the pump power was observed and could not be eliminated. Further investigations on its possible origin, such as thermal lensing, may help to reduce the rollover and enable the full use of the available pump power.

The largest leap forward in the pursuit of higher output powers was achieved with the operation of multiple amplifiers in series. This approach turned out to be a very effective way of reaching higher output powers. This is especially true if the foci and alignments are recycled for the subsequent amplifiers. With this approach, it was possible to amplify the initial seed power of 0.73 W to an output power of 16.6 W. This output should be compressible to pulse durations of about 30 fs to 50 fs.

At such high powers and intensities, it was found that gain narrowing is not an issue in the amplifiers discussed. Its appearance can be overcome with SPM-driven spectral broadening. In fact, the strong nonlinearity due to the high nonlinear refractive index must be managed already in the second amplifier stage to reduce self-focusing and the corresponding gain degradation. For this, one should apply a version of chirped pulse amplification and keep track of the dispersion as the pulses propagate through the amplifier arrangement.

Future implementations of the Cr:ZnS amplifiers can be improved in a variety of ways. If the amplifier system uses several pump beams but does not require independent power control of these, then the splitting of the pump laser should be realized with polarization-independent, partially reflective optics. This would preserve the intensity noise of the present pump laser at its lowest level. One would build thulium-laser-pumped amplifiers with higher doped gain crystals. If thermal beam quality degradation should appear with those crystals, then one would return to lower doped crystals and spread out the amplification over multiple crystals. Also promising are the recently available optical isolators, which

should enable polarization-based double-pass amplifiers by acting as Faraday mirrors.

The demonstrated output power of more than 16 W promises powerful mid-IR generation. Under the assumption that one can apply the conversion efficiencies demonstrated by others for Cr:ZnS-systems [140], one would obtain the following. The IDFG process optimized for spectral width (6.7 µm to 17 µm) would deliver 76 mW of power, which is about 1.5 times more power in an about 2.2 times broader mid-IR spectrum than used in the current Infrasampler [20, 27]. The IDFG process optimized for power generation (6.7 µm to 12 µm) would even deliver more than 1.3 W of mid-IR power. Therefore, such an amplifier chain with an output power of 16 W is a powerful new source for field-resolved spectroscopic measurements.

Chapter 6

Summary and Conclusion

Broadband, CEP-stable, femtosecond pulses in the mid-IR promise to revolutionize the analysis of biological samples through the technology of field-resolved infrared spectroscopy. This thesis was concerned with the search for the best driving laser that can provide, in conjunction with the process of intra-pulse difference-frequency generation, the desired mid-IR pulses at multiple megahertz repetition rates.

The mature Yb:YAG thin-disk technology operating at a wavelength of 1.03 µm provided a good starting point for the development of driving lasers with high average and peak powers — the latter parameter being particularly useful for enhancing nonlinear frequency conversion, such as from the near-infrared to the mid-infrared region. The further development of such a Kerr-lens mode-locked thin-disk oscillator in terms of peak power was reported in chapter 3. For the first time, the integration of an active multipass cell into such a KLM oscillator was experimentally tested.

The active multipass cell provided additional gain, and allowed substantially higher output coupling rates and access to a larger share of the intracavity peak power. The successful implementation doubled the oscillator's output coupling rate to 50 % — the highest demonstrated output coupling rate for KLM thin-disk oscillators to date. The resulting oscillator emits pulses with a pulse duration of 290 fs, at a repetition rate of 10.6 MHz and an average power of 140 W. This performance corresponds to a peak power of 40 MW and makes this oscillator the most powerful oscillator in terms of peak power in ambient air.

To further improve the peak power in the future, an active multipass cell could be implemented in evacuated Yb:YAG oscillators. In this way, peak powers of 200 MW or more could be produced directly. Other KLM thin-disk oscillators with less potent gain media would also benefit from the 2 to 4 times higher output coupling rates enabled by active multipass cells.

Apart from higher peak powers, the generation of mid-IR light can also be improved via other approaches. For instance, a change in the driving wavelength can significantly increase the conversion efficiency to the mid-IR due to the much wider selection of suitable conversion crystals with higher nonlinearities. Consequently, chapter 4 described the development of thin-disk oscillators at a wavelength of 2.1 µm and reported on the realization

of a femtosecond Ho:YAG KLM thin-disk oscillator.

Since Ho:YAG thin-disk oscillator is a nascent technology, much effort was focused on investigating and optimizing the disk parameters and on improving the technical implementation of the oscillator. The experiments on the disk thickness and doping concentration led to a much better understanding of their optimal ranges. The installation of the oscillator in a vacuum-compatible housing also revealed an unexpectedly large influence of humidity on laser performance. By dehumidifying the environment of the oscillator, the power was increased by 20 %.

While the Ho:YAG thin-disk technology is still maturing and will require more development before its deployment in field-resolved spectroscopy, bulk lasers based on Cr:ZnS were also identified as a promising technology for the realization of a driving laser at longer wavelengths. As described in chapter 5, these lasers can directly emit ultrashort pulses. Nevertheless, because of their lower output powers, they required the development of powerful amplifiers. Therefore, the research focus shifted to the questions of how and to what extent the performance of Cr:ZnS amplifiers can be improved.

Investigations of the doping concentration, beam-waist sizes and pump wavelength provided experimental evidence of the appropriate parameter ranges. The operation of four water-cooled amplifiers in series boosted an initial average seed power of 0.73 W to an output power of over 16 W. The realization of the first Peltier-cooled Cr:ZnS amplifier at about −30 °C demonstrated an improvement of about 19 % in power over conventional water-cooling.

Compared to the existing and only Infrasampler commissioned for biological sampling so far [20], ultrashort, 2.3 µm pulses with an average power of 16 W have the potential to generate 27 times more mid-IR power if the IDFG is optimized to the bandwidth currently in use. The mid-IR spectral bandwidth could in principle also be doubled from 6-11 µm to 6-17 µm, while providing, at 76 mW, 1.5 times more power. Therefore, the relatively simple technology of the amplifier chain should already provide enough power for mid-IR generation and the subsequent electro-optic sampling.

The search for the best driving laser for the generation of the coveted broadband, CEP-stabilized mid-IR light led to the investigation of various laser technologies, from Yb:YAG and Ho:YAG thin-disk oscillators to Cr:ZnS bulk-laser systems. The results obtained for these approaches are of significance for the respective technologies themselves and represent important steps for their advancement. Moreover, the improved Yb:YAG oscillator is already deployed for new field-resolved spectroscopy experiments. Yet the performance demonstrated for Cr:ZnS amplifiers makes Cr:ZnS bulk lasers the most compact, efficient, and promising front-end for future implementations. The future refinements of the Cr:ZnS bulk-laser technology and of field-resolved infrared spectroscopy shall lead to the envisioned breakthrough in the study of biological systems. This grand goal has motivated the advances in laser technology reported in this thesis, and it is expected that this goal will continue to stimulate important advances in the future.

Appendix A

Relative Intensity Noise

The optical power of a laser source $P_{optical}(t)$ can be written as a sum of a mean power P_{Mean} and a fluctuating term $\delta P(t)$.

$$P_{optical}(t) = P_{Mean} + \delta P(t) \tag{A.1}$$

The frequency-dependent relative intensity noise $RIN(\nu)$ is defined as the spectral density $S_{\delta P}(\nu)$ of the optical power fluctuations divided by the square of the optical mean power [172].

$$RIN(\nu) = \frac{S_{\delta P}(\nu)}{P_{Mean}^2} \tag{A.2}$$

For the measurement of the relative intensity noise, a fraction of the laser emission is focused onto a photodiode in reverse bias (for example, Det10D2, Thorlabs GmbH). This photodiode creates a current $I_{electrical}(t)$ and a voltage $U_{DC}(t)$ on a load, which are proportional to the incident optical power $P_{optical}(t)$. This proportionality is valid within the limits of the photodiode's response time and within the linear range of the photodiode. The voltage $U_{DC}(t)$ gets measured and can be separated again into a mean voltage U_{MeanDC} and a fluctuating voltage $\delta U(t)$.

$$U_{DC}(t) \propto I_{electrical}(t) \propto P_{optical}(t) \tag{A.3}$$

$$U_{DC}(t) = U_{MeanDC} + \delta U(t) \tag{A.4}$$

The proportionality of optical power to voltage is used to express the relative intensity noise as:

$$RIN(\nu) = \frac{S_{\delta U}(\nu)}{U_{MeanDC}^2} \quad , \tag{A.5}$$

where $S_{\delta U}(\nu)$ is the spectral density of the fluctuating voltage.

This quantity $S_{\delta U}(\nu)$ was determined by splitting-off the mean voltage U_{MeanDC} from the initial signal $U_{DC}(t)$, an eventual amplification of the residual and an analysis of the

so obtained signal on an RF spectrum analyzer (E4447A, Agilent). The spectrum analyzer determines the electrical power at the frequency ν within the frequency range RBW and returns this power as frequency-dependent quantity $dBm(\nu)$ in the unit dBm. This quantity was converted into $S_{\delta U}(\nu)$ by correcting for a potential power amplification G in units of dB, by converting from mW to W, by normalizing the resolution bandwidth and by multiplying with the input impedance R of the spectrum analyzer.

$$S_{\delta U}(\nu) = \frac{R}{\mathrm{RBW}} 10^{\frac{dBm(\nu)-G-30}{10}} \tag{A.6}$$

A measurement of the mean voltage then allowed the calculation of the optical relative intensity noise:

$$RIN(\nu) = \frac{R}{U_{MeanDC}^2 \mathrm{RBW}} 10^{\frac{dBm(\nu)-G-30}{10}} \ . \tag{A.7}$$

A common way to specify the amount of noise in a frequency interval $[\nu_1, \nu_2]$ is to integrate $RIN(\nu)$ and to take the square root of it. This procedure results in the variable "integrated $\mathrm{RIN_{rms}}$". This quantity is in its mathematical formulation similar to a root mean square of the optical power fluctuations normalized to the square of the optical mean power, which motivates the annex "rms".

$$\text{int. } \mathrm{RIN_{rms}} = \sqrt{\int_{\nu_1}^{\nu_2} RIN(\nu)\, \mathrm{d}\nu} \tag{A.8}$$

The integration is replaced by a summation since the data is discrete. Other numerical integration methods are eligible too. Differences between integration methods are noticeable, but not severe.

$$\text{int. } \mathrm{RIN_{rms}} = \sqrt{\Delta\nu \sum_m RIN_m} \tag{A.9}$$

The quantity int. $\mathrm{RIN_{rms}}$ is often expressed as a percentage.

Appendix B

Data Archiving

The experimental raw data, the corresponding evaluation files and the resulting figures are saved on the data archive server of the Laboratory for Attosecond Physics at the Max Planck Institute of Quantum Optics and can be found in the following directory:

/afs/ipp-garching.mpg.de/mpq/lap/publication_archive/Theses/2021/

The files there are organized in accordance with the structure of the thesis. For each figure, there is a separate folder that contains the associated data. If necessary, a *ReadMe.txt* file provides further explanations and instructions about the folder's contents.

Bibliography

[1] A. H. Zewail. *Femtochemistry: Atomic-Scale Dynamics of the Chemical Bond.* J. Phys. Chem. A **104**, 5660 (2000).

[2] F. Krausz and M. Ivanov. *Attosecond physics.* Rev. Mod. Phys. **81**, 163 (2009).

[3] K. Sugioka and Y. Cheng. *Ultrafast lasers–reliable tools for advanced materials processing.* Light: Science & Applications **3**, e149 (2014).

[4] T. W. Hänsch. *Nobel Lecture: Passion for precision.* Rev. Mod. Phys. **78**, 1297 (2006).

[5] T. Wilken, G. L. Curto, R. A. Probst, T. Steinmetz, A. Manescau, L. Pasquini, J. I. González Hernández, R. Rebolo, T. W. Hänsch, T. Udem, and R. Holzwarth. *A spectrograph for exoplanet observations calibrated at the centimetre-per-second level.* Nature **485**, 611 (2012).

[6] A. Beyer, L. Maisenbacher, A. Matveev, R. Pohl, K. Khabarova, A. Grinin, T. Lamour, D. C. Yost, T. W. Hänsch, N. Kolachevsky, and T. Udem. *The Rydberg constant and proton size from atomic hydrogen.* Science **358**, 79 (2017).

[7] I. Coddington, N. Newbury, and W. Swann. *Dual-comb spectroscopy.* Optica **3**, 414 (2016).

[8] H. Timmers, A. Kowligy, A. Lind, F. C. Cruz, N. Nader, M. Silfies, G. Ycas, T. K. Allison, P. G. Schunemann, S. B. Papp, and S. A. Diddams. *Molecular fingerprinting with bright, broadband infrared frequency combs.* Optica **5**, 727 (2018).

[9] P. Lasch. *Biomedical Vibrational Spectroscopy.* John Wiley & Sons, Incorporated, Hoboken : (2008.).

[10] N. L. Anderson and N. G. Anderson. *The Human Plasma Proteome.* Molecular & Cellular Proteomics **1**, 845 (2002).

[11] K. Hollywood, D. R. Brison, and R. Goodacre. *Metabolomics: Current technologies and future trends.* PROTEOMICS **6**, 4716 (2006).

[12] P. E. Geyer, L. M. Holdt, D. Teupser, and M. Mann. *Revisiting biomarker discovery by plasma proteomics.* Molecular Systems Biology **13**, 942 (2017).

[13] M. J. Baker, S. R. Hussain, L. Lovergne, V. Untereiner, C. Hughes, R. A. Lukaszewski, G. Thiefin, and G. D. Sockalingum. *Developing and understanding biofluid vibrational spectroscopy: a critical review.* Chem. Soc. Rev. **45**, 1803 (2016).

[14] H. Günzler. *IR-Spektroskopie.* Wiley-VCH, Weinheim (2003).

[15] N. R. Newbury, I. Coddington, and W. Swann. *Sensitivity of coherent dual-comb spectroscopy.* Opt. Express **18**, 7929 (2010).

[16] A. Schwaighofer, M. Montemurro, S. Freitag, C. Kristament, M. J. Culzoni, and B. Lendl. *Beyond Fourier Transform Infrared Spectroscopy: External Cavity Quantum Cascade Laser-Based Mid-infrared Transmission Spectroscopy of Proteins in the Amide I and Amide II Region.* Anal. Chem. **90**, 7072 (2018).

[17] I. Coddington, W. C. Swann, and N. R. Newbury. *Time-domain spectroscopy of molecular free-induction decay in the infrared.* Opt. Lett. **35**, 1395 (2010).

[18] A. Sell, R. Scheu, A. Leitenstorfer, and R. Huber. *Field-resolved detection of phase-locked infrared transients from a compact Er:fiber system tunable between 55 and 107 THz.* Applied Physics Letters **93**, 251107 (2008).

[19] A. S. Kowligy, H. Timmers, A. J. Lind, U. Elu, F. C. Cruz, P. G. Schunemann, J. Biegert, and S. A. Diddams. *Infrared electric field sampled frequency comb spectroscopy.* Science Advances **5** (2019).

[20] I. Pupeza, M. Huber, M. Trubetskov, W. Schweinberger, S. A. Hussain, C. Hofer, K. Fritsch, M. Poetzlberger, L. Vamos, E. Fill, T. Amotchkina, K. V. Kepesidis, A. Apolonski, N. Karpowicz, V. Pervak, O. Pronin, F. Fleischmann, A. Azzeer, M. Žigman, and F. Krausz. *Field-resolved infrared spectroscopy of biological systems.* Nature **577**, 52 (2020).

[21] Q. Wu and X.-C. Zhang. *Free-space electro-optic sampling of terahertz beams.* Applied Physics Letters **67**, 3523 (1995).

[22] G. Gallot and D. Grischkowsky. *Electro-optic detection of terahertz radiation.* J. Opt. Soc. Am. B **16**, 1204 (1999).

[23] M. Porer, J.-M. Ménard, and R. Huber. *Shot noise reduced terahertz detection via spectrally postfiltered electro-optic sampling.* Opt. Lett. **39**, 2435 (2014).

[24] S. Keiber, S. Sederberg, A. Schwarz, M. Trubetskov, V. Pervak, F. Krausz, and N. Karpowicz. *Electro-optic sampling of near-infrared waveforms.* Nature Photonics **10**, 159 (2016).

[25] P. R. Griffiths and J. A. de Haseth. *Fourier Transform Infrared Spectrometry*, chapter 6 - Other Components of FT-IR Spectrometers, pp. 143–160. John Wiley & Sons, Ltd, second edition (2007).

[26] P. Tidemand-Lichtenberg, J. S. Dam, H. V. Andersen, L. Høgstedt, and C. Pedersen. *Mid-infrared upconversion spectroscopy.* J. Opt. Soc. Am. B **33**, D28 (2016).

[27] M. Huber, M. Trubetskov, S. A. Hussain, W. Schweinberger, C. Hofer, and I. Pupeza. *Optimum Sample Thickness for Trace Analyte Detection with Field-Resolved Infrared Spectroscopy.* Anal. Chem. **92**, 7508 (2020).

[28] S. Vasilyev, I. S. Moskalev, V. O. Smolski, J. M. Peppers, M. Mirov, A. V. Muraviev, K. Zawilski, P. G. Schunemann, S. B. Mirov, K. L. Vodopyanov, and V. P. Gapontsev. *Super-octave longwave mid-infrared coherent transients produced by optical rectification of few-cycle 2.5-μm pulses.* Optica **6**, 111 (2019).

[29] E. Hecht. *Optics.* Pearson Education Limited, Harlow, fifth edition edition (2017). ISBN 13: 978-1-292-09693-3.

[30] L. Puskar and U. Schade. *The IRIS THz/Infrared beamline at BESSY II.* Journal of large-scale research facilities **2**, A95 (2016).

[31] J. Faist, F. Capasso, D. L. Sivco, C. Sirtori, A. L. Hutchinson, and A. Y. Cho. *Quantum Cascade Laser.* Science **264**, 553 (1994).

[32] Q. Lu, D. Wu, S. Slivken, and M. Razeghi. *High efficiency quantum cascade laser frequency comb.* Scientific Reports **7**, 43806 (2017).

[33] M. S. Vitiello, G. Scalari, B. Williams, and P. D. Natale. *Quantum cascade lasers: 20 years of challenges.* Opt. Express **23**, 5167 (2015).

[34] V. Petrov. *Parametric down-conversion devices: The coverage of the mid-infrared spectral range by solid-state laser sources.* Optical Materials **34**, 536 (2012).

[35] I. T. Sorokina. *Solid-State Mid-Infrared Laser Sources*, volume 89 of *Topics in Applied Physics*, chapter Crystalline Mid-Infrared Lasers, pp. 262–358. Springer Berlin Heidelberg (2003).

[36] S. Mirov, I. Moskalev, S. Vasilyev, V. Smolski, V. Fedorov, D. Martyshkin, J. Peppers, M. Mirov, A. Dergachev, and V. Gapontsev. *Frontiers of mid-IR lasers based on transition metal doped chalcogenides.* IEEE Journal of Selected Topics in Quantum Electronics **24**, 1 (2018).

[37] M. Ebrahimzadeh. *Solid-State Mid-Infrared Laser Sources*, chapter Mid-Infrared Ultrafast and Continuous- Wave Optical Parametric Oscillators, pp. 184–224. Springer Berlin Heidelberg, Berlin, Heidelberg (2003).

[38] V. Smolski, S. Vasilyev, I. Moskalev, M. Mirov, Q. Ru, A. Muraviev, P. Schunemann, S. Mirov, V. Gapontsev, and K. Vodopyanov. *Half-Watt average power femtosecond source spanning 3-8 μm based on subharmonic generation in GaAs.* Applied Physics B **124**, 101 (2018).

[39] C. Manzoni and G. Cerullo. *Design criteria for ultrafast optical parametric amplifiers.* Journal of Optics **18**, 103501 (2016).

[40] M. Seidel, X. Xiao, S. A. Hussain, G. Arisholm, A. Hartung, K. T. Zawilski, P. G. Schunemann, F. Habel, M. Trubetskov, V. Pervak, O. Pronin, and F. Krausz. *Multi-watt, multi-octave, mid-infrared femtosecond source.* Science Advances **4** (2018).

[41] W. Koechner. *Solid-state laser engineering.* Springer series in optical sciences. Springer, New York, NY, 6. rev. and updated edition (2006).

[42] B. E. A. Saleh and M. C. Teich. *Fundamentals of photonics.* Wiley series in pure and applied optics. Wiley-Interscience, Hoboken, NJ [u.a.] (2007).

[43] P. A. Berry and K. L. Schepler. *High-power, widely-tunable Cr2+:ZnSe master oscillator power amplifier systems.* Opt. Express **18**, 15062 (2010).

[44] O. Svelto. *Principles of Lasers.* Springer US, Boston, MA, 5th edition (2010).

[45] M. Eichhorn. *Quasi-three-level solid-state lasers in the near and mid infrared based on trivalent rare earth ions.* Applied Physics B **93**, 269 (2008).

[46] S. Vasilyev, I. Moskalev, M. Mirov, V. Smolski, S. Mirov, and V. Gapontsev. *Ultrafast middle-IR lasers and amplifiers based on polycrystalline Cr:ZnS and Cr:ZnSe.* Optics Materials Express **7**, 2636 (2017).

[47] J.-C. Diels and W. Rudolph. *Ultrashort laser pulse phenomena.* Elsevier, Acad. Press, Amsterdam [u.a.], 2nd edition (2006).

[48] N. Chunosov. *reZonator.* `http://www.rezonator.orion-project.org/`. Accessed on 2020-11-28.

[49] R. C. Eckardt. *Free-space laser resonators*, volume 1 - Principles, chapter A2.1, pp. 81–114. Inst. of Physics Publ. (2004).

[50] A. Penzkofer, M. Wittmann, M. Lorenz, E. Siegert, and S. Macnamara. *Kerr lens effects in a folded-cavity four-mirror linear resonator.* Optical and Quantum Electronics **28**, 423 (1996).

[51] International Organization for Standardization. *ISO 11146-1:2005: Lasers and laser-related equipment - Test methods for laser beam widths, divergence angles and beam propagation ratios* (2005).

[52] N. Hodgson. *Laser resonators and beam propagation.* Springer series in optical sciences. Springer, New York, NY (2005).

[53] A. M. Weiner. *Ultrafast optics.* Wiley series in pure and applied optics. Wiley, Hoboken, NJ ; Hoboken, NJ (2009).

[54] U. Keller, K. J. Weingarten, F. X. Kartner, D. Kopf, B. Braun, I. D. Jung, R. Fluck, C. Honninger, N. Matuschek, and J. Aus der Au. *Semiconductor saturable absorber mirrors (SESAM's) for femtosecond to nanosecond pulse generation in solid-state lasers.* IEEE Journal of Selected Topics in Quantum Electronics **2**, 435 (1996).

[55] F. X. Kärtner. *Few-cycle laser pulse generation and its applications.* Topics in applied physics. Springer, Berlin [u.a.] (2004).

[56] N. Modsching, J. Drs, J. Fischer, C. Paradis, F. Labaye, M. Gaponenko, C. Kränkel, V. J. Wittwer, and T. Südmeyer. *Sub-100-fs Kerr lens mode-locked Yb:Lu2O3 thin-disk laser oscillator operating at 21 W average power.* Opt. Express **27**, 16111 (2019).

[57] J. Brons. *High-power femtosecond laser-oscillators for applications in high-field physics.* Ph.D. thesis, Ludwig-Maximilians-Universität München (2017).

[58] S. T. Cundiff, J. Ye, and J. L. Hall. *Optical frequency synthesis based on mode-locked lasers.* Review of Scientific Instruments **72**, 3749 (2001).

[59] R. P. Trebino. *Frequency-resolved optical gating.* Kluwer Academic Publishers, Boston ; Boston (2000).

[60] V. Pervak, I. Ahmad, S. A. Trushin, Z. Major, A. Apolonski, S. Karsch, and F. Krausz. *Chirped-pulse amplification of laser pulses with dispersive mirrors.* Opt. Express **17**, 19204 (2009).

[61] O. Pronin, M. Seidel, F. Lücking, J. Brons, E. Fedulova, M. Trubetskov, V. Pervak, A. Apolonski, T. Udem, and F. Krausz. *High-power multi-megahertz source of waveform-stabilized few-cycle light.* Nature Communications **6**, 6988 (2015).

[62] K. DeLong. *FROG (Frequency-Resolved Optical Gating) Software.* `https://github.com/kenwdelong/frog`. Accessed on 2020-12-02.

[63] R. W. Boyd. *Nonlinear Optics.* Elsevier, Acad. Press ; Elsevier, Acad. Press, Amsterdam [u.a.], 3. edition (2008).

[64] J. Weitenberg. *Transversale Moden in optischen Resonatoren für Anwendungen hoher Laserintensität.* Ph.D. thesis, Rheinisch-Westfälischen Technischen Hochschule Aachen (2017). ISBN 978-3-86359-596-8.

[65] R. M. Kaumanns. *Generation of energetic femtosecond pulses at high average power.* Ph.D. thesis, Ludwig-Maximilians-Universität München (2020).

[66] C. J. Saraceno, F. Emaury, C. Schriber, A. Diebold, M. Hoffmann, M. Golling, T. Südmeyer, and U. Keller. *Toward Millijoule-Level High-Power Ultrafast Thin-Disk Oscillators*. IEEE Journal of Selected Topics in Quantum Electronics **21**, 106 (2015).

[67] D. Strickland and G. Mourou. *Compression of amplified chirped optical pulses*. Optics Communications **56**, 219 (1985).

[68] R. L. Sutherland. *Handbook of nonlinear optics*. Optical engineering. Dekker, New York [u.a.] (2003).

[69] C. Gaida, M. Gebhardt, T. Heuermann, F. Stutzki, C. Jauregui, J. Antonio-Lopez, A. Schülzgen, R. Amezcua-Correa, A. Tünnermann, I. Pupeza, and J. Limpert. *Watt-scale super-octave mid-infrared intrapulse difference frequency generation*. Light: Science & Applications **7**, 94 (2018).

[70] O. Novák, P. R. Krogen, T. Kroh, T. Mocek, F. X. Kärtner, and K.-H. Hong. *Femtosecond 8.5 μm source based on intrapulse difference-frequency generation of 2.1 μm pulses*. Opt. Lett. **43**, 1335 (2018).

[71] J. Zhang, K. Mak, N. Nagl, M. Seidel, D. Bauer, D. Sutter, V. Pervak, F. Krausz, and O. Pronin. *Multi-mW, few-cycle mid-infrared continuum spanning from 500 to 2250 cm^{-1}*. Light: Science and Applications **7**, 17180 (2018).

[72] G. Cerullo, A. Baltuška, O. Mücke, and C. Vozzi. *Few-optical-cycle light pulses with passive carrier-envelope phase stabilization*. Laser & Photonics Reviews **5**, 323 (2011).

[73] A. Giesen, H. Hügel, A. Voss, K. Wittig, U. Brauch, and H. Opower. *Scalable concept for diode-pumped high-power solid-state lasers*. Applied Physics B **58**, 365 (1994).

[74] C. J. Saraceno, D. Sutter, T. Metzger, and M. Abdou Ahmed. *The amazing progress of high-power ultrafast thin-disk lasers*. Journal of the European Optical Society-Rapid Publications **15**, 15 (2019).

[75] W. Demtröder. *Experimentalphysik - Mechanik und Wärme*. Springer, Berlin [u.a.], 5th edition (2008).

[76] I. Pupeza, D. Sánchez, J. Zhang, N. Lilienfein, M. Seidel, N. Karpowicz, T. Paasch-Colberg, I. Znakovskaya, M. Pescher, W. Schweinberger, V. Pervak, E. Fill, O. Pronin, Z. Wei, F. Krausz, A. Apolonski, and J. Biegert. *High-power sub-two-cycle mid-infrared pulses at 100 MHz repetition rate*. Nature Photonics **9**, 721 (2015).

[77] F. Saltarelli, I. J. Graumann, L. Lang, D. Bauer, C. R. Phillips, and U. Keller. *Power scaling of ultrafast oscillators: 350-W average-power sub-picosecond thin-disk laser*. Opt. Express **27**, 31465 (2019).

[78] C. J. Saraceno, F. Emaury, C. Schriber, M. Hoffmann, M. Golling, T. Südmeyer, and U. Keller. *Ultrafast thin-disk laser with 80 μJ pulse energy and 242 W of average power.* Optics Letters **39**, 9 (2014).

[79] M. Müller, C. Aleshire, A. Klenke, E. Haddad, F. Légaré, A. Tünnermann, and J. Limpert. *10.4 kW coherently combined ultrafast fiber laser.* Opt. Lett. **45**, 3083 (2020).

[80] T. Nubbemeyer, M. Kaumanns, M. Ueffing, M. Gorjan, A. Alismail, H. Fattahi, J. Brons, O. Pronin, H. G. Barros, Z. Major, T. Metzger, D. Sutter, and F. Krausz. *1 kW, 200 mJ picosecond thin-disk laser system.* Opt. Lett. **42**, 1381 (2017).

[81] F. Meyer, T. Vogel, S. Ahmed, and C. J. Saraceno. *Single-cycle, MHz repetition rate THz source with 66 mW of average power.* Opt. Lett. **45**, 2494 (2020).

[82] F. Emaury, A. Diebold, C. J. Saraceno, and U. Keller. *Compact extreme ultraviolet source at megahertz pulse repetition rate with a low-noise ultrafast thin-disk laser oscillator.* Optica **2**, 980 (2015).

[83] T. Südmeyer, S. V. Marchese, S. Hashimoto, C. R. E. Baer, G. Gingras, B. Witzel, and U. Keller. *Femtosecond laser oscillators for high-field science.* Nature Photonics **2**, 599 (2008).

[84] T. Südmeyer, C. Kränkel, C. R. E. Baer, O. H. Heckl, C. J. Saraceno, M. Golling, R. Peters, K. Petermann, G. Huber, and U. Keller. *High-power ultrafast thin disk laser oscillators and their potential for sub-100-femtosecond pulse generation.* Applied Physics B **97**, 281 (2009).

[85] J.-H. Wolter, M. A. Ahmed, and T. Graf. *Thin-disk laser operation of Ti:sapphire.* Opt. Lett. **42**, 1624 (2017).

[86] J.-H. Wolter, A. Voss, R. Balmer, S. Ricaud, M. Antier, C. Simon-Boisson, T. Graf, and M. A. Ahmed. *Ti:sapphire Thin-Disk Laser with Plano-Convex-Shaped Single-Crystal Diamond Heat Spreaders.* In *2019 Conference on Lasers and Electro-Optics Europe and European Quantum Electronics Conference*, pp. ca–p–50. Optical Society of America (2019).

[87] J. Schulte, T. Sartorius, J. Weitenberg, A. Vernaleken, and P. Russbueldt. *Nonlinear pulse compression in a multi-pass cell.* Optics Letters **41**, 4511 (2016).

[88] K. Fritsch, M. Poetzlberger, V. Pervak, J. Brons, and O. Pronin. *All-solid-state multipass spectral broadening to sub-20 fs.* Optics Letters **43**, 4643 (2018).

[89] S. Gröbmeyer, K. Fritsch, B. Schneider, M. Poetzlberger, V. Pervak, J. Brons, and O. Pronin. *Self-compression at 1 μm wavelength in all-bulk multi-pass geometry.* Applied Physics B **126**, 159 (2020).

[90] M. Pötzlberger. *Kerrlinsen-modengekoppelte Dünnscheibenlaser mit mehrfachen Scheibendurchgängen*. Master's thesis, Ludwig-Maximilians-Universität München (2016).

[91] J. Koerner, C. Vorholt, H. Liebetrau, M. Kahle, D. Kloepfel, R. Seifert, J. Hein, and M. C. Kaluza. *Measurement of temperature-dependent absorption and emission spectra of Yb:YAG, Yb:LuAG, and Yb:CaF2 between 20°C and 200°C and predictions on their influence on laser performance*. J. Opt. Soc. Am. B **29**, 2493 (2012).

[92] J. Zhang, J. Brons, M. Seidel, V. Pervak, V. Kalashnikov, Z. Wei, A. Apolonski, F. Krausz, and O. Pronin. *49-fs Yb:YAG thin-disk oscillator with distributed Kerr-lens mode-locking*. In *2015 European Conference on Lasers and Electro-Optics - European Quantum Electronics Conference*, pp. PD–A–1. Optical Society of America (2015).

[93] O. Pronin, J. Brons, C. Grasse, V. Pervak, G. Boehm, M. C. Amann, A. Apolonski, V. L. Kalashnikov, and F. Krausz. *High-power Kerr-lens mode-locked Yb:YAG thin-disk oscillator in the positive dispersion regime*. Optics Letters **37**, 3543 (2012).

[94] K. Beil, S. T. Fredrich-Thornton, F. Tellkamp, R. Peters, C. Kränkel, K. Petermann, and G. Huber. *Thermal and laser properties of Yb:LuAG for kW thin disk lasers*. Opt. Express **18**, 20712 (2010).

[95] X. Xu, Z. Zhao, P. Song, B. Jiang, G. Zhou, J. Xu, P. Deng, G. Bourdet, J. Christophe Chanteloup, J.-P. Zou, and A. Fulop. *Upconversion luminescence in Yb3+-doped yttrium aluminum garnets*. Physica B: Condensed Matter **357**, 365 (2005).

[96] F. Saltarelli, I. J. Graumann, L. Lang, D. Bauer, C. R. Phillips, and U. Keller. *Power Scaling of Ultrafast Laser Oscillators: 350-W Output Power Sub-ps SESAM-Modelocked Thin-Disk Laser*. In *Conference on Lasers and Electro-Optics*, p. SF3E.3. Optical Society of America (2019).

[97] E. Vicentini, Y. Wang, D. Gatti, A. Gambetta, P. Laporta, G. Galzerano, K. Curtis, K. McEwan, C. R. Howle, and N. Coluccelli. *Nonlinear pulse compression to 22 fs at 15.6 µJ by an all-solid-state multipass approach*. Opt. Express **28**, 4541 (2020).

[98] J. Brons, V. Pervak, D. Bauer, D. Sutter, O. Pronin, and F. Krausz. *Powerful 100-fs-scale Kerr-lens mode-locked thin-disk oscillator*. Optics Letters **41**, 3567 (2016).

[99] D. Bauer, I. Zawischa, D. H. Sutter, A. Killi, and T. Dekorsy. *Mode-locked Yb:YAG thin-disk oscillator with 41 µJ pulse energy at 145 W average infrared power and high power frequency conversion*. Optics Express **20**, 9698 (2012).

[100] F. Saltarelli, A. Diebold, I. J. Graumann, C. R. Phillips, and U. Keller. *Self-phase modulation cancellation in a high-power ultrafast thin-disk laser oscillator*. Optica **5**, 1603 (2018).

[101] J. Brons, V. Pervak, E. Fedulova, D. Bauer, D. Sutter, V. Kalashnikov, A. Apolonskiy, O. Pronin, and F. Krausz. *Energy scaling of Kerr-lens mode-locked thin-disk oscillators.* Optics Letters **39**, 6442 (2014).

[102] M. Poetzlberger, J. Zhang, S. Gröbmeyer, D. Bauer, D. Sutter, J. Brons, and O. Pronin. *Kerr-lens mode-locked thin-disk oscillator with 50% output coupling rate.* Opt. Lett. **44**, 4227 (2019).

[103] C. J. Saraceno, F. Emaury, O. H. Heckl, C. R. E. Baer, M. Hoffmann, C. Schriber, M. Golling, T. Südmeyer, and U. Keller. *275 W average output power from a femtosecond thin disk oscillator operated in a vacuum environment.* Opt. Express **20**, 23535 (2012).

[104] R. Paschotta and U. Keller. *Passive mode locking with slow saturable absorbers.* Applied Physics B **73**, 653 (2001).

[105] H. A. Haus. *Mode-locking of lasers.* IEEE Journal of Selected Topics in Quantum Electronics **6**, 1173 (2000).

[106] S. V. Marchese, T. Südmeyer, M. Golling, R. Grange, and U. Keller. *Pulse energy scaling to 5 μJ from a femtosecond thin disk laser.* Optics Letters **31**, 2728 (2006).

[107] M. Baumgartl, C. Lecaplain, A. Hideur, J. Limpert, and A. Tünnermann. *66 W average power from a microjoule-class sub-100 fs fiber oscillator.* Opt. Lett. **37**, 1640 (2012).

[108] A. Chong, W. H. Renninger, and F. W. Wise. *Properties of normal-dispersion femtosecond fiber lasers.* Journal of the Optical Society of America B **25**, 140 (2008).

[109] S. Naumov, A. Fernandez, R. Graf, P. Dombi, F. Krausz, and A. Apolonski. *Approaching the microjoule frontier with femtosecond laser oscillators.* New Journal of Physics **7**, 216 (2005).

[110] G. Palmer, M. Schultze, M. Siegel, M. Emons, U. Bünting, and U. Morgner. *Passively mode-locked Yb:KLu(WO_4)$_2$ thin-disk oscillator operated in the positive and negative dispersion regime.* Optics Letters **33**, 1608 (2008).

[111] F. Ö. Ilday, D. K. Kesim, M. Hoffmann, and C. J. Saraceno. *Discrete Similariton and Dissipative Soliton Modelocking for Energy Scaling Ultrafast Thin-Disk Laser Oscillators.* IEEE Journal of Selected Topics in Quantum Electronics **24**, 1 (2018).

[112] W. Liu, R. Liao, J. Zhao, J. Cui, Y. Song, C. Wang, and M. Hu. *Femtosecond Mamyshev oscillator with 10-MW-level peak power.* Optica **6**, 194 (2019).

[113] K. Beckwitt, F. W. Wise, L. Qian, L. A. Walker, and E. Canto-Said. *Compensation for self-focusing by use of cascade quadratic nonlinearity.* Optics Letters **26**, 1696 (2001).

[114] J. Neuhaus, J. Kleinbauer, A. Killi, S. Weiler, D. Sutter, and T. Dekorsy. *Passively mode-locked Yb:YAG thin-disk laser with pulse energies exceeding 13 μJ by use of an active multipass geometry.* Optics Letters **33**, 726 (2008).

[115] J. Neuhaus, D. Bauer, J. Zhang, A. Killi, J. Kleinbauer, M. Kumkar, S. Weiler, M. Guina, D. H. Sutter, and T. Dekorsy. *Subpicosecond thin-disk laser oscillator with pulse energies of up to 25.9 μJ by use of an active multipass geometry.* Opt. Express **16**, 20530 (2008).

[116] J. Neuhaus. *Passively mode-locked Yb:YAG thin-disk laser with active multipass geometry.* Ph.D. thesis, Universität Konstanz, Konstanz (2009).

[117] D. Bauer. *Modengekoppelte Scheibenoszillatoren für Materialbearbeitung.* Ph.D. thesis, Universität Konstanz, Konstanz (2012).

[118] J. Neuhaus, D. Bauer, J. Kleinbauer, A. Killi, D. H. Sutter, and T. Dekorsy. *Numerical analysis of a sub-picosecond thin-disk laser oscillator with active multipass geometry showing a variation of pulse duration within one round trip.* Journal of the Optical Society of America B **27**, 65 (2010).

[119] A. Jackson, M. Ohmer, and S. LeClair. *Relationship of the second order nonlinear optical coefficient to energy gap in inorganic non-centrosymmetric crystals.* Infrared Physics & Technology **38**, 233 (1997).

[120] K. Vodopyanov, S. Mirov, V. Voevodin, and P. Schunemann. *Two-photon absorption in GaSe and CdGeAs2.* Optics Communications **155**, 47 (1998).

[121] V. Petrov, A. Yelisseyev, L. Isaenko, S. Lobanov, A. Titov, and J.-J. Zondy. *Second harmonic generation and optical parametric amplification in the mid-IR with orthorhombic biaxial crystals LiGaS2 and LiGaSe2.* Applied Physics B **78**, 543 (2004).

[122] K. L. Vodopyanov. *Parametric generation of tunable infrared radiation in ZnGeP2 and GaSe pumped at 3 μm.* J. Opt. Soc. Am. B **10**, 1723 (1993).

[123] C. Hofer, S. A. Hussain, W. Schweinberger, M. Huber, T. P. Butler, D. Gerz, N. Karpowicz, F. Krausz, and I. Pupeza. *Quantum-Efficiency and Bandwidth Optimized Electro-Optic Sampling.* In *OSA Technical Digest*, pp. cf–p–15. Optical Society of America, Munich (2019).

[124] S. Lamrini, P. Koopmann, M. Schäfer, K. Scholle, and P. Fuhrberg. *Efficient high-power Ho:YAG laser directly in-band pumped by a GaSb-based laser diode stack at 1.9 μm.* Applied Physics B **106**, 315 (2012).

[125] N. P. Barnes, B. M. Walsh, and E. D. Filer. *Ho:Ho upconversion: applications to Ho lasers.* J. Opt. Soc. Am. B **20**, 1212 (2003).

[126] O. L. Antipov, I. D. Eranov, and R. I. Kositsyn. *36 W Q-switched Ho:YAG laser at 2097 nm pumped by a Tm fiber laser: evaluation of different Ho3+ doping concentrations.* Laser Physics Letters **14**, 015002 (2016).

[127] E. Lippert, S. Nicolas, G. Arisholm, K. Stenersen, and G. Rustad. *Midinfrared laser source with high power and beam quality.* Appl. Opt. **45**, 3839 (2006).

[128] M. Schellhorn. *Performance of a Ho:YAG thin-disc laser pumped by a diode-pumped 1.9 µm thulium laser.* Applied Physics B **85**, 549 (2006).

[129] G. Renz. *Moderate high power 1 to 20 µs and kHz Ho:YAG thin disk laser pulses for laser lithotripsy.* In W. A. Clarkson and R. K. Shori (eds.), *Solid State Lasers XXIV: Technology and Devices*, volume 9342, pp. 373 – 380. International Society for Optics and Photonics, SPIE (2015).

[130] G. Renz, J. Speiser, and A. Giesen. *InP-diode laser stack pumped Ho:YAG or Cr:ZnSe thin disk lasers.* In *2013 Conference on Lasers and Electro-Optics Europe International Quantum Electronics Conference CLEO EUROPE/IQEC*, pp. 1–1 (2013).

[131] J. Zhang, F. Schulze, K. F. Mak, V. Pervak, D. Bauer, D. Sutter, and O. Pronin. *High-Power, High-Efficiency Tm:YAG and Ho:YAG Thin-Disk Lasers.* Laser & Photonics Reviews **12**, 1700273 (2018).

[132] S. Tomilov, T. Vogel, M. Hoffmann, Y. Wang, and C. J. Saraceno. *100 W-class 2 µm Ho:YAG Thin-Disk Laser.* In *Conference on Lasers and Electro-Optics*, p. SM3E.1. Optical Society of America (2020).

[133] J. Zhang, K. F. Mak, and O. Pronin. *Kerr-Lens Mode-Locked 2µm Thin-Disk Lasers.* IEEE Journal of Selected Topics in Quantum Electronics **24**, 1 (2018).

[134] B. M. Walsh. *Review of Tm and Ho materials; spectroscopy and lasers.* Laser Physics **19**, 855 (2009).

[135] G. Renz and J. Speiser. *Recent Work on Ho:YAG Thin Disk Lasers in the multiple 10 W Range.* In *Stuttgart Laser Technology Forum* (2018).

[136] M. Liu, S. Wang, D. Tang, L. Chen, and J. Ma. *Preparation and upconversion luminescence of YAG(Y3Al5O12): Yb3+, Ho3+ nanocrystals.* Journal of Rare Earths **27**, 66 (2009).

[137] J. B. Gruber, M. D. Seltzer, V. J. Pugh, and F. S. Richardson. *Electronic energy-level structure of trivalent holmium in yttrium aluminum garnet.* Journal of Applied Physics **77**, 5882 (1995).

[138] A. Diebold, F. Saltarelli, I. J. Graumann, C. J. Saraceno, C. R. Phillips, and U. Keller. *Gas-lens effect in kW-class thin-disk lasers.* Opt. Express **26**, 12648 (2018).

[139] S. Tomilov, T. Vogel, M. Hoffmann, Y. Wang, and C. J. Saraceno. *High-power CW Ho:YAG thin-disk laser and first SESAM-modelocking.* In *Europhoton*, pp. We–A3.6 (2020).

[140] S. Vasilyev, V. Smolski, I. Moskalev, J. Peppers, M. Mirov, Y. Barnakov, V. Fedorov, D. Martyshkin, A. Muraviev, K. Zawilski, P. Schunemann, S. Mirov, K. Vodopyanov, and V. Gapontsev. *Multi-octave infrared femtosecond continuum generation in Cr:ZnS-GaSe and Cr:ZnS-ZGP tandems.* In P. G. Schunemann and K. L. Schepler (eds.), *Nonlinear Frequency Generation and Conversion: Materials and Devices XIX*, volume 11264, pp. 13–24. International Society for Optics and Photonics, SPIE (2020).

[141] S. Vasilyev, I. Moskalev, V. Smolski, J. Peppers, M. Mirov, A. Muraviev, K. Vodopyanov, S. Mirov, and V. Gapontsev. *Multi-octave visible to long-wave IR femtosecond continuum generated in Cr:ZnS-GaSe tandem.* Optics Express **27**, 16405 (2019).

[142] Q. Wang, J. Zhang, N. Nagl, V. Pervak, F. Krausz, O. Pronin, and K. F. Mak. *Highly Efficient Broadband Mid-Infrared Generation (2.8-12.5 μm) Based on a Compact Cr:ZnS Laser.* In *2019 Conference on Lasers and Electro-Optics Europe European Quantum Electronics Conference (CLEO/Europe-EQEC)*, pp. 1–1 (2019).

[143] Q. Wang, J. Zhang, A. Kessel, N. Nagl, V. Pervak, O. Pronin, and K. F. Mak. *Broadband mid-infrared coverage (2–17 μm) with few-cycle pulses via cascaded parametric processes.* Opt. Lett. **44**, 2566 (2019).

[144] N. Nagl, S. Gröbmeyer, V. Pervak, F. Krausz, O. Pronin, and K. F. Mak. *Directly diode-pumped, Kerr-lens mode-locked, few-cycle Cr:ZnSe oscillator.* Opt. Express **27**, 24445 (2019).

[145] N. Nagl, S. Gröbmeyer, M. Potzlberger, V. Pervak, F. Krausz, and K. F. Mak. *Directly Diode-Pumped Few-Optical-Cycle Cr:ZnS Laser at 800 mW of Average Power.* In *Conference on Lasers and Electro-Optics*, p. SF3H.5. Optical Society of America (2020).

[146] L. D. DeLoach, R. H. Page, G. D. Wilke, S. A. Payne, and W. F. Krupke. *Transition metal-doped zinc chalcogenides: spectroscopy and laser demonstration of a new class of gain media.* IEEE Journal of Quantum Electronics **32**, 885 (1996).

[147] Y. K. Ha. *Directly diode-pumped femtosecond Cr:ZnS amplifier.* Master's thesis, Ludwig-Maximilians-Universität München (2019).

[148] C. Gaida, M. Gebhardt, T. Heuermann, F. Stutzki, C. Jauregui, and J. Limpert. *Ultrafast thulium fiber laser system emitting more than 1 kW of average power.* Opt. Lett. **43**, 5853 (2018).

[149] T. Matniyaz, F. Kong, M. T. Kalichevsky-Dong, and L. Dong. *302 W single-mode power from an Er/Yb fiber MOPA.* Opt. Lett. **45**, 2910 (2020).

[150] H. Lin, Y. Feng, Y. Feng, P. Barua, J. K. Sahu, and J. Nilsson. *656 W Er-doped, Yb-free large-core fiber laser.* Opt. Lett. **43**, 3080 (2018).

[151] I. T. Sorokina and E. Sorokin. *Femtosecond Cr2+-Based Lasers.* IEEE Journal of Selected Topics in Quantum Electronics **21**, 273 (2015).

[152] V. E. Leshchenko, B. K. Talbert, Y. H. Lai, S. Li, Y. Tang, S. J. Hageman, G. Smith, P. Agostini, L. F. DiMauro, and C. I. Blaga. *High-power few-cycle Cr:ZnSe mid-infrared source for attosecond soft x-ray physics.* Optica **7**, 981 (2020).

[153] M. Yumoto, N. Saito, and S. Wada. *50 mJ/pulse, electronically tuned Cr:ZnSe master oscillator power amplifier.* Opt. Express **25**, 32948 (2017).

[154] P. Komm, U. Sheintop, S. Noach, and G. Marcus. *Carrier-to-envelope phase-stable, mid-infrared, ultrashort pulses from a hybrid parametric generator: Cr:ZnSe laser amplifier system.* Opt. Express **27**, 18522 (2019).

[155] S. Vasilyev, I. Moskalev, V. Smolski, J. Peppers, M. Mirov, V. Fedorov, D. Martyshkin, S. Mirov, and V. Gapontsev. *Octave-spanning Cr:ZnS femtosecond laser with intrinsic nonlinear interferometry.* Optica **6**, 126 (2019).

[156] S. Vasilyev, I. Moskalev, V. Smolski, J. Peppers, M. Mirov, S. Mirov, and V. Gapontsev. *27 Watt middle-IR femtosecond laser system at 2.4 μm.* In *Laser Congress 2018 (ASSL)*, p. AW3A.1. Optical Society of America (2018).

[157] S. Vasilyev, M. Mirov, and V. Gapontsev. *Kerr-lens mode-locked femtosecond polycrystalline Cr^{2+}:ZnS and Cr^{2+}:ZnSe lasers.* Optics Express **22**, 5118 (2014).

[158] A. Ozawa, T. Udem, U. D. Zeitner, T. W. Hänsch, and P. Hommelhoff. *Modeling and optimization of single-pass laser amplifiers for high-repetition-rate laser pulses.* Phys. Rev. A **82**, 033815 (2010).

[159] S. Vasilyev, I. Moskalev, M. Mirov, S. Mirov, and V. Gapontsev. *Multi-Watt mid-IR femtosecond polycrystalline Cr^{2+}:ZnS and Cr^{2+}:ZnSe laser amplifiers with the spectrum spanning 2.0 - 2.6 μm.* Opt. Express **24**, 1616 (2016).

[160] P. A. Popov, S. V. Kuznetsov, A. A. Krugovykh, N. V. Mitroshenkov, S. S. Balabanov, and P. P. Fedorov. *Study of the thermal conductivity of PbS, CuFeS2, ZnS.* Kondensirovannye Sredy I Mezhfaznye Granitsy = Condensed Matter and Interphases **22**, 97 (2020).

[161] S. Backus, R. Bartels, S. Thompson, R. Dollinger, H. C. Kapteyn, and M. M. Murnane. *High-efficiency, single-stage 7-kHz high-average-power ultrafast laser system.* Opt. Lett. **26**, 465 (2001).

[162] W. Demtröder. *Experimentalphysik 2*. Springer-Lehrbuch. Springer, Berlin (2017).

[163] A. Říha, H. Jelínková, M. Němec, M. Čech, D. Vyhlídal, M. E. Doroshenko, and V. V. Badikov. *Temperature dependence of Cr:ZnSe active medium spectral and laser properties*. In *Proc.SPIE*, volume 11033, pp. – (2019).

[164] H. Burton, C. Debardelaben, W. Amir, and T. A. Planchon. *Temperature dependence of Ti:Sapphire fluorescence spectra for the design of cryogenic cooled Ti:Sapphire CPA laser*. Opt. Express **25**, 6954 (2017).

[165] J. A. Bebawi, I. Kandas, M. A. El-Osairy, and M. H. Aly. *A Comprehensive Study on EDFA Characteristics: Temperature Impact*. Applied Sciences **8** (2018).

[166] A. Ozawa, W. Schneider, F. Najafi, T. W. Hänsch, T. Udem, and P. Hommelhoff. *A Peltier Cooled Single Pass Amplifier for Titanium:Sapphire Laser Pulses*. Laser Physics **20**, 967 (2010).

[167] M. N. Polyanskiy. *Refractive index database*. `https://refractiveindex.info`. Accessed on 2020-11-17.

[168] I. H. Malitson. *A Redetermination of Some Optical Properties of Calcium Fluoride*. Appl. Opt. **2**, 1103 (1963).

[169] G. Ernst, W. Witteman, J. Verschuur, R. Mols, B. van Oerle, A. Bouman, J. Botman, H. Hagedoorn, J. Delhez, and W. Kleeven. *The "TEU-FEL" project*. Infrared Physics & Technology **36**, 81 (1995). Proceedings of the Sixth International Conference on Infrared Physics.

[170] M. Porer. *Ultrafast low-energy dynamics of strongly correlated systems*. Ph.D. thesis, Universität Regensburg (2015).

[171] S. Jackel, I. Moshe, and R. Lavi. *Comparison of adaptive optics and phase-conjugate mirrors for correction of aberrations in double-pass amplifiers*. Appl. Opt. **42**, 983 (2003).

[172] International Organization for Standardization. *ISO 11554:2017: Optik und Photonik - Laser und Laseranlagen - Prüfverfahren für Leistung, Energie und Kenngrößen des Zeitverhaltens von Laserstrahlen* (2017).

List of Publications

Peer Reviewed Journal Articles

- *Markus Poetzlberger*, Jinwei Zhang, Sebastian Gröbmeyer, Dominik Bauer, Dirk Sutter, Jonathan Brons and Oleg Pronin, "Kerr-lens mode-locked thin-disk oscillator with 50 % output coupling rate", Opt. Lett. 44, 4227-4230 (2019)
- Ioachim Pupeza, Marinus Huber, Michael Trubetskov, Wolfgang Schweinberger, Syed A. Hussain, Christina Hofer, Kilian Fritsch, *Markus Poetzlberger*, Lenard Vamos, Ernst Fill, Tatiana Amotchkina, Kosmas V. Kepesidis, Alexander Apolonski, Nicholas Karpowicz, Vladimir Pervak, Oleg Pronin, Frank Fleischmann, Abdallah Azzeer, Mihaela Žigman and Ferenc Krausz, "Field-resolved infrared spectroscopy of biological systems", Nature 577, 52–59 (2020)
- Kilian Fritsch, *Markus Poetzlberger*, Vladimir Pervak, Jonathan Brons and Oleg Pronin, "All-solid-state multipass spectral broadening to sub-20 fs", Opt. Lett. 43, 4643-4646 (2018)
- Sebastian Gröbmeyer, Kilian Fritsch, Benedikt Schneider, *Markus Poetzlberger*, Vladimir Pervak, Jonathan Brons and Oleg Pronin, "Self-compression at 1 µm wavelength in all-bulk multi-pass geometry", Appl. Phys. B 126, 159 (2020)
- In preparation
  Markus Poetzlberger, Nathalie Nagl, Qing Wang and Ka Fai Mak, "Power scaling of Cr:ZnS amplifiers"

Selected Conference Talks

- *M. Poetzlberger*, J. Brons, D. Bauer, D. Sutter, J. Zhang, F. Krausz and O. Pronin, "Kerr-lens mode-locked thin-disk oscillator with 50 % output coupling rate", in 8th EPS-QEOD Europhoton Conference 2018, p. FrM2.3
- *M. Poetzlberger*, J. Brons, J. Zhang, D. Bauer, D. Sutter, F. Krausz and O. Pronin, "Towards Active Multipass Kerr-lens Mode-locked Yb:YAG Thin-disk Oscillators", in 2017 European Conference on Lasers and Electro-Optics and European Quantum Electronics Conference, (Optical Society of America, 2017), p. CA_7_2.

Danksagung

Ich möchte meinen Dank zuerst an Prof. Dr. Ferenc Krausz richten dafür, dass er dieses Forschungsumfeld mit all seinen Möglichkeiten geschaffen hat. Ohne dieses Umfeld wäre unsere Arbeit nicht möglich.

Ein herzliches Danke ergeht auch an Prof. Dr. Jörg Schreiber, welcher sich ohne zu zögern bereit erklärt hat, mir die Ehre zu erweisen und meine Dissertation zu begutachten.

Darüber hinaus möchte ich mich noch bei den Professoren Dr. Armin Scrinzi, Dr. Joachim Rädler, Dr. Achim Hartschuh und Dr. Ivo Sachs bedanken, die sich dankenswerterweise die Zeit nahmen, mein Prüfungskomitee zu bilden.

Der größte Dank geht an meinen Gruppenleiter Dr. Kafai Mak. Durch dein Coaching bin ich über mich hinausgewachsen! Ich hoffe inständig, dass auch du eines Tages im gleichen Ausmaß von unserer gemeinsamen Zeit profitierst und dass du den Erfolg erlebst, den du dir so sehr verdienst! Du bist ein „supervisor“, wie man ihn sich nur wünschen kann! Bleib so und lass nicht nach in deinen Bemühungen ein guter „leader“ zu sein!

Ein Danke an Prof. Dr. Oleg Pronin dafür, dass er mich vor Jahren in sein Team geholt hat und für die guten Zeiten, die ich dadurch hatte!

A heartfelt thank-you to Prof. Dr. Jinwei Zhang for accompanying my first steps in the field of laser physics and the great, view-expanding conversations late in the office. I miss those days :)

Was wäre die Arbeit ohne Arbeitskollegen, in deren Umfeld man gerne viele Stunden verbringt?! Solche Kollegen habe ich in euch, Kilian, Sebastian und Nathalie, gefunden! In besonderer Erinnerung werden mir die Unternehmungen abseits der Arbeit bleiben, ob bei Reisen auf der Autobahn, dem Erkunden von Landshut oder unter nächtlichem Himmel. Und auch fachlich bin ich froh, euch im Team gehabt zu haben! Besonders dir Kilian ein Danke für die professionelle Entwicklung von so vielen mechanischen Komponenten, die Unterstützung bei meinen ersten Schritten in Python und für die Einführung unseres Datenservers. Dir Nathalie ein Danke für deine vielseitigen FROG-Skripte und deine Oszillatoren.

Und was wäre die Arbeit ohne Vorgänger?! Daher an dieser Stelle ein Danke an Jonathan und Marcus, dafür, dass ihr eure Erfahrung gerne teilt.

But what would the last 1.5 years have been like without new colleagues?! Aleksandar, Philipp, Shizhen and Maciej, I'm glad that four such competent and interesting personalities joined our team. I'm also grateful for the valuable feedback that you guys have given me for my thesis!

I'm also grateful that I had the opportunity to meet so many more nice and interesting individuals over the last few years! Christina, Yookyung, Daniel, Martin, Dmitrii, Gaia, Qing, Marinus, Wolfgang, Leonard, Maksim, Ann-Kathrin, Theresa, Moritz, Maximilian, Benedikt, Tobias, Johannes, Meriem, Magdalena, Julia,... essentially a list without ending!

Ein Laser lässt sich nicht ohne Spiegel bauen. Genau so würde unserem Lehrstuhl etwas fehlen, ohne Vladimir und seinem Team! Danke Vladimir für deine tollen Spiegel!

Für die großartige Zusammenarbeit möchte ich mich auch bei Herrn Oehm und seinem Team von der Mechanik-Werkstatt bedanken! Ihr habt wirklich jeden meiner Aufträge zu meiner vollsten Zufriedenheit erledigt! Und war doch mal Feuer am Dach, dann fand man rasche, unkomplizierte Hilfe bei Mechanik Limmer! Ein Danke dafür!

Unser Institut zeichnet sich durch weitere, nicht direkt in der Wissenschaft tätige, Mitarbeiter aus! Stellvertretend möchte ich hier Klaus dafür danken, dass er die gute Seele unseres Stockwerks ist. Florian, Hans und Herrn Bär möchte ich dafür danken, dass sie die Bude am Laufen halten, und Katharina dafür, dass sie unsere vielen Bestellungen beglichen hat.

Abschließend ein Dank an meine Freunde, die mein Leben bereichern, und an meine Familie, welche mich bestmöglich durch das Ende meiner Doktorarbeit gebracht hat!

Danke euch allen!